**Title**

Infragravity Runup Methods: 1D or 2D?

**Author**

Henderson, Cassandra Starr

**Publication Date**

2024

UNIVERSITY OF CALIFORNIA SAN DIEGO

# Infragravity Runup Methods: 1D or 2D?

A dissertation submitted in partial satisfaction of the
requirements for the degree Doctor of Philosophy

in

Oceanography

by

Cassandra Starr Henderson

Committee in charge:

Mark A. Merrifield, Chair
Bruce D. Cornuelle
Julia W. Fiedler
Robert T. Guza
Geno Pawlak

2024

The Dissertation of Cassandra Starr Henderson is approved, and it is acceptable in quality and form for publication on microfilm and electronically.

University of California San Diego

2024

# EPIGRAPH

We will be victorious if we have not forgotten how to learn.

– *Rosa Luxemburg*

# TABLE OF CONTENTS

## LIST OF FIGURES

# LIST OF TABLES

## ACKNOWLEDGEMENTS

Thank you to the whole Coastal Processes Group, but especially Mark Merrifield, R.T. Guza, and Julia Fiedler, whose support have been foundational to this work. Mark, you supported me through difficult times, when many would not have. Thank you. Guza, your excitement and passion for science helped me rebuild my motivation after devastating setbacks. I consider myself well advised. To Julia, thank you for teaching me how to use numerical wave models. I also am deeply grateful to Bruce Cornuelle for teaching me his Bayesian methods, and to Geno Pawlak for his "outside" role in the committee. I am also grateful to Duncan Wheeler, Athina Lange, Bingchen Liu, Austin Barnes, Andrea Rodriguez-Marin Freudmann, Helen Zhang, Sierra Byrne, Niv Anidjar, Holden Leslie-Bole, Connor Mack, Lauren Kim, and the rest of the Center for Coastal Studies basement crew. Through the waves and strange smells, we endured. I also extend my gratitude to Michele Okihiro, Brian Woodward, Adam Young, Hironori Matsumoto, Robert Grenzeack, Kent Smith, Lucian Perry Shane Finnerty, Mele Johnson, Carson Black, Esther Nofodji and the rest of the intrepid field crew. Also Andrew Skemer, Michael Strauss, Jenny Greene, and Gillian Knapp from astronomy land, and other friends in physical oceanography; Bonnie Ludka, Theresa Morrison, Margaret Lindemann, and Luke Kachelein.

I would also be remiss if I did not acknowledge the tremendous contributions made by the United Auto Workers, Local 4811, without whom, I and many others would not be able to pay rent. You all have my admiration, especially Charlotte, Will, Briar, Anna, Anjali (and Tu), Niv, Jessica, Isaiah, Monica, Devon, Alejandra, Gwen, Adu, Hiya, Kate (and Jeremy), Lian, Vero, Alick, Joe, Kat, Nico, Luke, Jack, Euan, Jack D, Kelvin, Ankitha, Rafael, and many more. You supported my when I was low, taught me that class struggle is everywhere, and solidarity is forever. Especially large shout-out to my friends in Grad Workers United for Progress, and to Jessica Ng, with whom I have shared many adventures.

I also acknowledge bt werner, my friend, colleague, and comrade, and my friends in the San Diego Local of the Film Camera Club (CC) – Ananth, Ron, Marcos, Cande, Ash, Sahar, Jacob, Matt, Alonzo, Juliana, Kate, Lian, Allie, and alumni Alex, Jonathan, Paige, and Mark, and honorary members André, Charlie, Haley, Elle, and Sam. I am lucky to find myself among such excellent people. To Ananth, I have always admired your integrity as an organizer. To Cande, who is probably the only one of you who will read this – your rigor of scientific and cultural criticism shows me what it means to take scholarship seriously.

To Tom Schneck, who got me started on this road by dissuading me from engineering to go pursue physics, thanks for the push, and thank you to my other beloved grandparents Pat Schneck, Donna Henderson, and Starr Henderson, and my dear sister Erica (and Amanda). To Allie, despite all the struggles, I will treasure my last years in grad school because of you. To Mom and Dad, words are inadequate to express my love and gratitude for your support, especially at the end. All is well.

Chapter 1, in full, is a reprint of the material as it appears in Coastal Engineering 175 (2022). Cassandra S. Henderson, Julia W. Fiedler, Mark A. Merrifield, R.T. Guza and Adam P. Young, 2022. The dissertation author was the primary investigator and author of this paper.

Chapter 2, in full, is currently being prepared for submission for publication of the material. Cassandra S. Henderson and R.T. Guza, Bruce D. Cornuelle, Mark A. Merrifield and Julia W. Fiedler. The dissertation author was the primary investigator and author of this material.

# VITA

| | |
|---|---|
| 2017 | Bachelor of Science, University of California Santa Cruz |
| 2017-2018 | Research Assistant, Princeton University |
| 2024 | Doctor of Philosophy, University of California San Diego |

# PUBLICATIONS

Henderson, C., Skemer, A., Morley, C., Fortney, J. “A new statistical method for the characterization of exoplanet atmospheres.” 2017, MNRAS, Mon Not R Astron Soc 2017. doi.org/10.1093/mnras/stx1495

Henderson, C., Merrifield, M., Fiedler, J., Guza, R.T., Young, A., “Field Observations and modeling of storm wave runup and overtopping”, Coastal Engineering 2022, doi.org/10.1016/j.coastaleng.2022.104128

Henderson, C., Guza, R.T., Cornuelle, B.D., Merrifield, M., Fiedler, J.W., “Bayesian Analysis of Infragravity Edge Waves”, in prep.

# ABSTRACT OF THE DISSERTATION

## Infragravity Runup Methods: 1D or 2D?

by

Cassandra Starr Henderson

Doctor of Philosophy in Oceanography

University of California San Diego, 2024

Mark A. Merrifield, Chair

Infragravity (IG) waves are long period ocean waves (nominally 25 to 250 seconds) generated by nonlinear, long period variations in the momentum flux of incident sea swell (nominally 4 to 25 sec) wave groups in shallow water. IG waves are ubiquitous on the shoreline, can dominate the runup during storms, and contribute to wave driven flooding. Predicting IG waves with numerical wave models or empirically are a current research topic in Nearshore Physical Oceanography.

In chapter 1, we initialize the the nonhydrostatic numerical wave model SWASH with measurements in 6m depth and compare model predictions to LiDAR observations of wave runup and overtopping in Imperial Beach, CA. SWASH (1D) skillfully predicts wave by wave runup and overtopping.

In chapter 2, we challenge the 1D assumption inherent in chapter 1 by examining the impacts of infragravity edge waves propagating alongshore (in 2D) as well as cross-shore, using observations over 2 months at Torrey Pines. Edge waves can be up to 25% of the runup variance, and are most significant (sometimes¿ 80%) for alongshore velocities. SWASH 1D lacks 2D edge waves, but partially compensates by overpredicting non-edge (e.g. leaky ) IG waves. Edge waves contribute to errors in 1D methodologies.

In the appendix, SWASH 2D is used to simulate infragravity edge waves, and demonstrate a need for further development of modeling methodologies.

# Introduction

Since the first observations of infragravity waves by Munk (1949) and Tucker and Deacon (1950), IG waves have been a key topic in nearshore physical oceanography, owing to their contributions to surfzone dynamics and wave impacts alike. These long period (25 to 250 second) waves arise from nonlinear interactions between short period waves (4 to 25 seconds). Where short period waves (a.k.a. sea swell waves or SS waves) are generated offshore by wind, infragravity waves (IG waves) are generated through nonlinear interactions in the surfzone (for mathematical developments, see Biesel (1952); Longuet-Higgins and Stewart (1964); Hasselmann (1967)). In many cases, IG waves grow larger than SS waves in very shallow water, and are primary contributors to wave runup and overtopping (see chapter 1, but also Bertin et al. (2018)). They are strongly affected by changes in depth, and therefore mostly trapped in shallow water, but some travel into deep water and can be detected in the deep ocean (Webb et al., 1991) and even in ice fields (Bromirski et al., 2010).

Oceanographers also took interest in edge waves, which are solutions to the shallow water equations describing trapped waves that travel parallel to shore (Stokes, 1846; Ursell, 1952). Edge waves are a resonant mode of the surfzone, arising from multiple constructively interfering waves (Schäffer and Jonsson, 1992) which experience the beach as a wave guide. These waves were discovered to be highly energetic at lower-than-IG frequencies (5 minutes to 10 hours) (Munk et al., 1964), and they were first attributed to wind gusts or hurricanes (Munk et al., 1956). Eventually Gallagher (1971) connected the dynamics of IG waves to edge waves, leading to lab (e.g. Bowen and Guza (1978)) and field studies (Huntley (1976);

Huntley et al. (1981); Oltman-Shay and Guza (1987) and many more) of infragravity edge waves. Edge waves were thought to be a significant contributor to surfzone physics. Of edge waves, Walter Munk said “it has turned out that the linear edge waves provide a linear core to the highly nonlinear coastal and littoral dynamics” (Munk, 2000).

Recently, to account for the nonlinear interactions between individual waves, numerical models which resolve individual waves have come into prominence (e.g. SWASH (Simulating WAves till SHore); Zijlema et al. (2011)). These models have high skill at predicting wave runup using only wave action along a cross-shore transect (hence they are 1-dimensional), which by definition excludes edge waves (which are 2-dimensional).

In Chapter 1, one of these nonlinear models (SWASH) is tested for suitability for simulating wave runup from offshore wave measurements along a cross-shore transect at Imperial Beach, CA, and compared to LiDAR observations. SWASH-predicted and LiDAR-observed runup time series are in-phase and coherent in both the sea-swell and infragravity frequency bands. The ability of a 1D model to explain nonlinear dynamics of infragravity waves raises the question: what about edge waves?

In Chapter 2, an array of sensors is deployed at Torrey Pines State Beach, CA, to study infragravity edge waves, similar to Oltman-Shay and Guza (1987); Huntley et al. (1981), but with longer spacing, deeper sensors, and more data. Also, rather than using linear array methods as done previously, Bayesian statistics are used to combine all measurements (regardless of sensor location) to estimate the intensity of edge waves (as called for by Huntley (1988)).

Chapter 2 is extensive, and spans a major field experiment, the development and adaptation of a statistical method from deep water oceanography (Bayesian Maximum a Posteriori, see Kachelein et al. (2022)) to shallow water, and the exploration of the results for understanding edge wave physics. We demonstrate that edge wave strength is associated with high tide, supporting the hypothesis that edge waves are enhanced with a steeper slope and stronger shoreline reflection.

Significant attempts were also made to model edge waves in SWASH, and some success was achieved, shown in Appendix B, but significant challenges arose with the offshore boundary condition and domain shape, so these results are limited.

We find that linear edge waves explain a significant fraction of infragravity energy, depending on location, up to 25% of the infragravity wave runup and up to 50% of the alongshore velocity infragravity variance offshore. Yet 1D methods still perform well, and the margin of error from infragravity edge waves on runup is comparable to a variety of other error sources, suggesting edge waves are a higher order effect on most beaches.

# Chapter 1

# Phase resolving runup and overtopping field validation of SWASH

## Abstract

Time series of storm wave runup and overtopping observed on a sandy beach with a scanning LiDAR are compared with predictions of the phase-resolving numerical model SWASH 1D. SWASH is initialized 300m offshore (8-m depth) with phase-resolved estimates of shoreward and seaward propagating waves, observed with a co-located pressure sensor-current meter. During 5 hours of storm conditions (2.4-m significant wave height, 17-sec peak period, high tide) swash zone bed level erosion of 80cm was observed with the LiDAR and included in SWASH simulations. Model offshore bathymetry is an ensemble of historical surveys. SWASH-predicted and LiDAR-observed runup time series are in-phase and coherent in both the sea-swell and infragravity frequency bands. Overtopping was intermittent and occurred only for the largest runups that were at suboptimal viewing angles. SWASH overpredicted by a factor of two the number of overtopping events observed with LiDAR and a single point pressure sensor. Phase-coupling between infragravity and sea swell waves at the offshore boundary and shoreline erosion both significantly affect model runup and overtopping. SWASH prediction misfits of 5-6% in runup sea-swell and infragravity heights are encouragingly small given the uncertainty in underwater bathymetry, 1D dynamics assumption, and default model representations of wave breaking

and bottom friction.

## 1.1 Introduction

Climate change will raise sea level, alter waves and beach morphologies, increase flood risk, and require costly adaptations (Nicholls and Cazenave (2010); Hinkel et al. (2014), and many others). On the US west coast, coastal erosion and flooding during storms are driven by coincident high waves and tides. Wave runup and overtopping of coastal defenses sometimes are included in predictions of future flooding (O'Neill et al., 2018; Barnard et al., 2019), but sometimes only setup is used (Vousdoukas et al., 2016) owing both to fundamental deficiencies in runup modeling (Gomes da Silva et al., 2020), and a general lack of high-resolution bathymetry required for detailed flood modeling (Gallien et al., 2018). Additional challenges in modeling extreme runup include a sometimes rapidly eroding shoreline, significant along-shore variability, and uncaptured impacts associated with groundwater and sediment properties.

For practical purposes, runup on sandy beaches is often predicted using an empirical parameterization (Stockdon et al. (2006)) that uses bulk offshore wave conditions ($H_0$ and $L_0$), and a single beach slope to represent topographic effects. Sometimes more information is available and an empirical method can be calibrated using the conditions of the beach (e.g. EurOtop; Pullen et al. (2007)). Empirical models of runup (i.e. Stockdon) or overtopping (EurOtop) are good options where site information, such as offshore bathymetry and incident wave energy spectra, is unavailable for initializing a numerical model. However, empirical runup estimates tend to have high errors, especially for extreme events (Gallien, 2016; Fiedler et al., 2018, 2020). Improving empirical models presents many challenges, including accounting for aleatory (random) uncertainty (Torres-Freyermuth et al., 2019) and variations in beach profile (Gomes da Silva et al., 2020; Soldini et al., 2013).

Numerical models of nearshore processes vary from phase-averaged shallow water or Boussinesq equations models (e.g. XBeach hydrostatic; Roelvink et al. (2009), SWAN; Holthuijsen et al. (1993)), to phase resolving models (SWASH (Simulating WAves till Shore); Zijlema et al. (2011); XBeach non-hydrostatic; Smit et al. (2010); to full Reynolds-Averaged Navier Stokes (RANS) equation solvers (e.g. OpenFOAM; Jasak et al. (2007)). RANS and VOF solvers accurately predict surfzone wave transformation and some fine scale processes (e.g. turbulence) but are computationally expensive and impractical for modeling many realistic wave and beach conditions. Individual infragravity (IG) waves are resolved in some phase-averaged models (XBeach) and omitted in others (SWAN). Phase-averaged models lack 2-way nonlinear coupling between sea-swell (SS) and IG frequencies. Significant work has been done to improve phase-averaged model parameterizations of infragravity waves and overtopping (Lashley et al., 2020; Roelvink et al., 2018).

Models that resolve phases of both SS and IG waves are a compromise where important physics are retained with (relatively) modest computation requirements. Fully phase-resolv-ing numerical models for runup and overtopping have been extensively validated in the laboratory: XBeach; Lashley et al. (2018); Roelvink et al. (2018); de Ridder et al. (2021); SWASH: Ruju et al. (2014); Smit et al. (2014); Suzuki et al. (2017); Lashley et al. (2020); and in the field: XBeach; McCall et al. (2014) (XBeach-G), de Beer et al. (2021), SWASH: Torres-Freyermuth et al. (2012); Nicolae Lerma et al. (2017); Gomes da Silva et al. (2020). Field validating 2D runup models is a longstanding challenge (Battjes and Gerritsen, 2002), and is often limited to bulk statistics.

Numerical models are limited by simplified dynamics of modeling assumptions required by lack of processing power and limited dynamical understanding. For example, the commonly used 1D assumption, valid in the narrow flumes used often for model testing, is known to overestimate IG energy by ignoring directional spread (Herbers et al., 1999; de Bakker et al., 2014). Bed roughness (i.e. friction) significantly impacts higher frequency runup (Torres-Freyermuth et al., 2019), but is difficult to directly observe and is sometimes tuned to improve model fit (e.g. Fiedler et al. (2018)). Infiltration into the sand bed is also important (Villarroel-Lamb et al., 2014). Depth-averaged models do not resolve the turbulence important for sediment transport (Briganti et al., 2016). Amplitudes and phases of shoreward propagating IG and SS waves (as well as spectra) at the offshore boundary are ideal, but rarely measured. Limited boundary condition information limits model accuracy (Fiedler et al., 2019, 2020; Gomes da Silva et al., 2020). Various surfzone dynamics such as bore-bore capture (Stringari and Power, 2020) and wave groupiness (Roelvink et al., 2018), depend on phases.

Model testing also is limited by the lack of accurate runup measurements. Video imagery is commonly used, with runup obtained by sensing the visible runup toe (Holman, 1986; Foote and Horn, 1999; Salmon et al., 2007; Almar et al., 2017). Depth of the detected runup line from this method is known only approximately. Detecting rundown from a foam line can be even more challenging, increasing noise (Aagaard and Holm, 1989). LiDAR (used here) improves runup observation (e.g. Almeida et al. (2013)), but can be costly and require extensive signal processing (section 2.2).

Gallien (2016) used runup model predictions with Xbeach in both hydrostatic (phase averaged) and non-hydrostatic (phase resolved) modes, to predict street flooding at Imperial Beach. Observed and modeled spatial extent of street flooding in this study agreed well, despite variations in flood volume of an order of magnitude. On one transect the total flood estimated volumes were: EurOtop: 160,000 l/m, nonhydrostatic XBeach: 35171 or 8595 l/m depending on domain length, and hydrostatic XBeach: 4531 l/m. These large discrepancies highlight the need for additional overtopping model validation with more detailed field observations as presented here.

Fiedler et al. (2018) modeled runup with SWASH on a 1D transect initialized with co-located pressure and current meters in ∼10 m depth at two US West Coast beaches, and compared the 10 cm runup depth line between SWASH and LiDAR-observed runup, showing agreement in observed bulk runup statistics (e.g. R2%). Fiedler et al. (2020) developed an empirical runup formula specifically for Imperial Beach using 20 years of wave hindcasts, historical beach profiles, and SWASH. They showed good agreement between bulk runup statistics predicted by the empirical formula and the storm observations discussed here. Street flooding forecasts based on this analysis were developed by Merrifield et al. (2021) and available here: https://climateadapt.ucsd.edu/imperialbeach/forecast/.

Here, we utilize field observations of runup and overtopping to validate SWASH during an extreme event. The model shows considerable skill for predicting phase-resolved runup and number of overtopping events, demonstrating that SWASH run on a 1D transect can be used to predict individual overtopping events in the field during storm conditions. We focus on the number of observed individual overtopping events as our model validation for overtopping. Five hours of observed storm waves and runup (Sections 1.2.1, 1.2.2) are used to initialize SWASH (Sections 1.2.3, 1.2.4). SWASH is compared to observations in detail, including runup (Section 1.3.1), and overtopping (Section 1.3.2). Sources of error are considered (Section 1.3.3), and the offshore conditions between observation and model are compared (Section 1.3.4). Model sensitivity to removing information is discussed (Section 1.3.5). Conclusions are in Section 1.4.

## 1.2 Methods

### 1.2.1 Observations and Study Site

Imperial Beach, a low-lying beach community in southern California, experiences chronic street flooding during coincident high waves and high tides, with impacts sometimes compounded by pollution (Steele et al 2018). Significant overtopping and backbeach erosion were observed on January 18, 2019, when high spring tides (with a range of ∼2.6 m) coincided with energetic swell (Figure 1.1). At a buoy in 20 m depth, directional spread (17 deg) was relatively low, and significant wave height (2.4 m) and wave period (17 s) were moderately high for this site (Figure 1.2). Shoreward propagating waves observed with a co-located pressure and current sensor in ∼8 m depth about 300 m offshore were used to initialize SWASH (PUV located in Figure 1.3a. Observed waves in Figure 1.4).

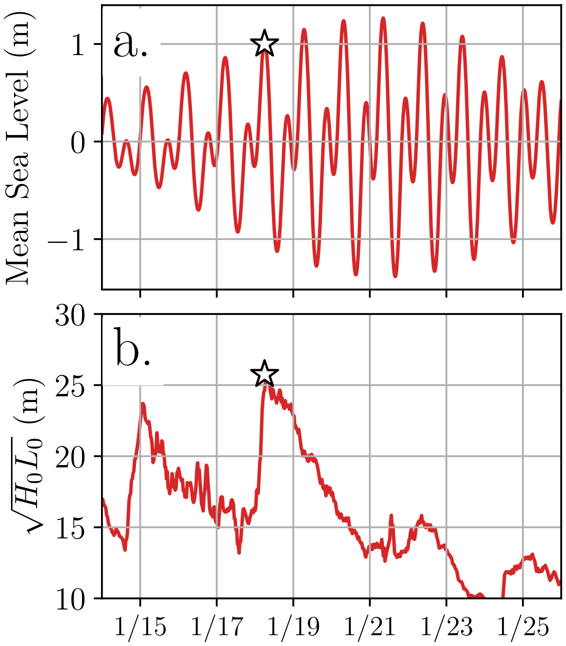

**Figure 1.1.** Time series of tide and $\sqrt{H_0 L_0}$, noting date of Imperial Beach study. (a) Water level (MSL, end of Scripps Pier ∼40 km north of the study site) (b) $\sqrt{H_0 L_0}$, a key parameter in empirical runup formulae, at offshore CDIP buoy 155 (20 m water depth). January 18, 2019, shown with white star, was a spring high tide.

The 1 km of the coastline of Imperial Beach most prone to flooding is backed with riprap, a roughly 2 m tall pile of ∼1 m diameter rocks placed between the sandy beach and community infrastructure. In some locations the landward side of the riprap is backed by structures (e.g. apartment buildings) which impede overtopping but can be damaged. In other areas overtopped water flows directly into the street (e.g. our focus site, Cortez Ave., see Figure 1.3a). The along-shore variability in flood dynamics is not addressed here.

A scanning LiDAR (RIEGL VZ-2000, 1550 nm wavelength) deployed on a 2nd story condo 20 m north of Cortez Ave. (Figure 1.3) observed a single crossshore transect at 10 Hz (lines per second) for a single high tide in nine 28-minute bursts. The scanned region extended from the seaward side of the riprap (which extends up to ∼2 meters above the sand level and ∼5 m above the water level) to ∼100 m offshore. Sand levels during

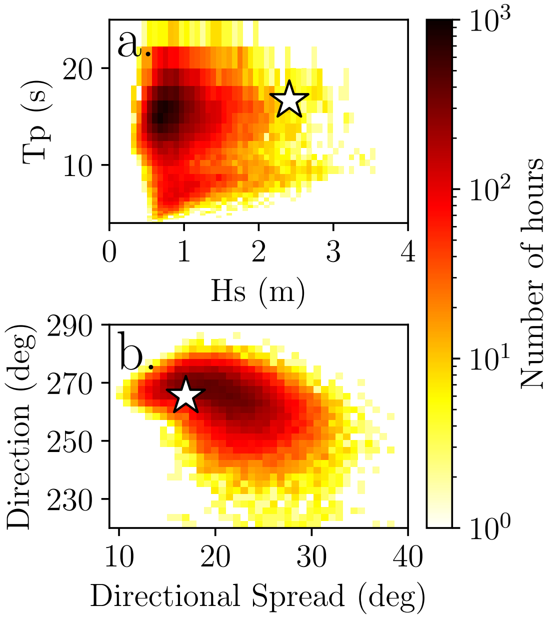

**Figure 1.2.** Historic wave conditions from 2006-2020 at CDIP buoy 155 (near Imperial Beach CA), compared to present conditions. White star is 18 Jan 2019. (a) peak period (Tp) versus significant wave height (Hs). (b) average wave direction versus directional spread. Waves were relatively energetic, long period and directionally narrow. Directional spread is defined for buoy data in van Kuik et al. (1988).

the storm, measured in the swash zone during wave downrushes with the LiDAR, eroded 80 cm over 5 hours (Figure 1.5). These same data are used by Fiedler et al. (2020).

Bed elevations from the backbeach to ∼10 m depth have been collected since 2009 with a GPS-equipped ATV and push dolly, and a jetski outfitted with acoustic sonar (Ludka et al. (2015)). A 2012 beach nourishment, intended to widen the subaerial beach and prevent street flooding, was mostly eroded but remained detectable in 2019 (Ludka et al. (2019)). Owing to beach closure from pollution, October 2018 was the most recent subaqueous survey prior to the January 2019 LiDAR observations. Winter profiles of beaches in San Diego are characteristically eroded (see: https://siocpg.ucsd.edu/data-products/beach-report/), so to avoid running the model on an unrealistic accreted October profile, an ensemble of observed eroded profiles from previous years are used for underwater SWASH bathymetry (Figure 1.3b).

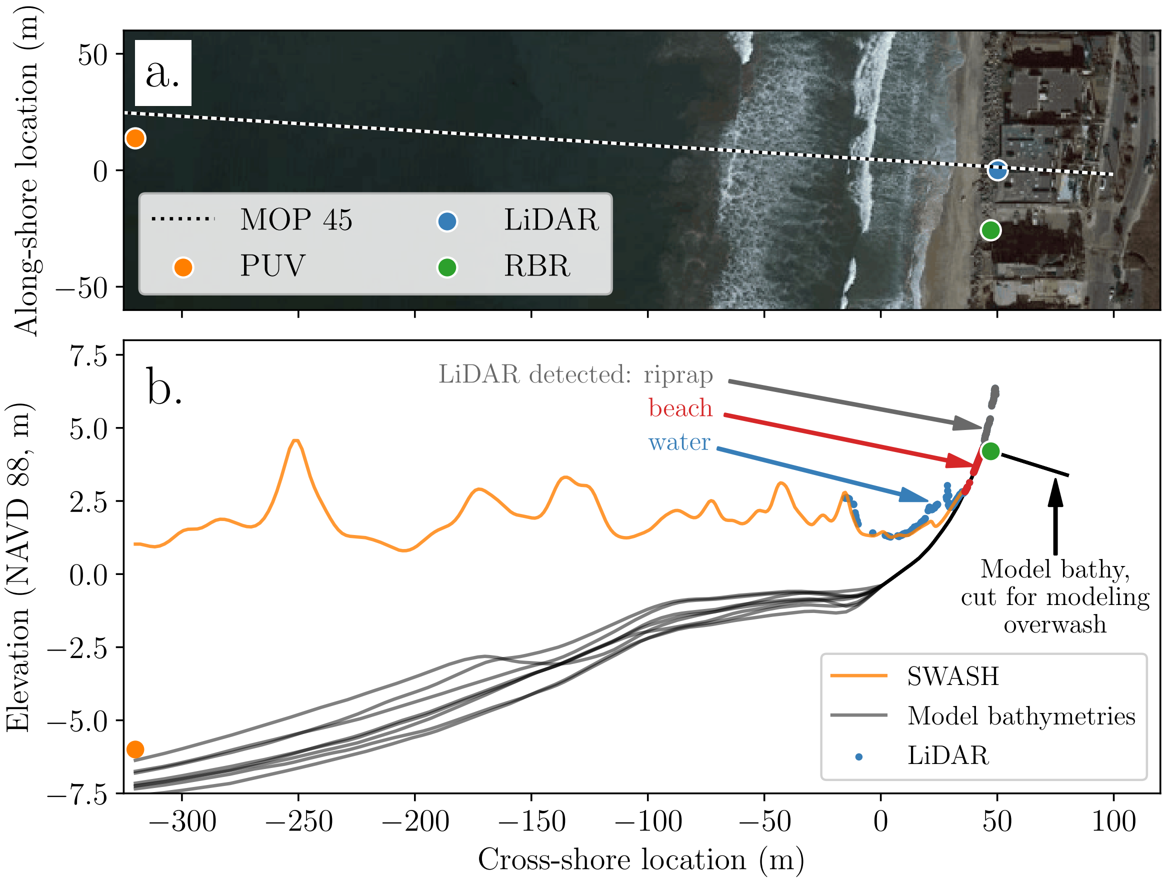

**Figure 1.3.** Observing system on 18 Jan 2019, at Imperial Beach, CA. (a) aerial (low-tide) photo showing locations of pressure and current meters (PUV, 8m depth including tide), scanning Lidar, and backbeach pressure sensor (RBR). Bathymetry has been observed since 2009 on transect 45 (dashed white line) of the Scripps Institution of Oceanography wave Monitoring and Prediction (MOP) system. The cross-shore origin is the average horizontal MSL before a 2012 beach nourishment. (b) model depth versus cross-shore location relative to MSL. Historical profiles below MSL (multiple black curves) are combined with LiDAR-observed evolving swash zone and backbeach bathymetry (see Figure 1.5). Orange curve is a snapshot of SWASH simulated water elevation.

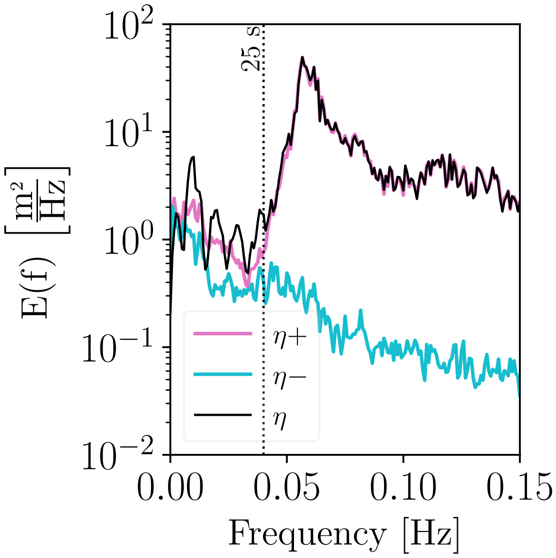

**Figure 1.4.** Sea surface elevation spectra E(f) estimated with a colocated pressure sensor and current meter in ~8 m depth, ~300 m offshore (see Figure 1.3). Total sea surface elevation spectra ($\eta$, black) is decomposed into shoreward ($\eta+$, purple) and seaward ($\eta-$, turquoise) going components. SWASH is initialized with $\eta+$ time series.

An RBRsolo3 D pressure sensor was mounted at the base of a signpole behind the riprap at the base of Cortez Avenue (Figure 1.3a), which slopes down ~40 m towards the main street, Seacoast Drive, and the Tijuana River Estuary behind it. The pressure sensor detected overtopping waves, but could not be used for volume estimates. Water from overtopping pooled at the Seacoast Drive-Cortez Ave. intersection and drained slowly into the estuary.

Over the whole observation period, waves were consistently large ($H_{\mathrm{sig}} \approx 2.4$ m). Overtopping was controlled by the tide, and peaked (1.015 m relative to MSL) at high tide around 14:00 (UTC) and stopped around 18:00, when the tide had dropped back to MSL.

### 1.2.2 LiDAR Processing

LiDAR observations were binned temporally at 10 Hz and spatially in 10 cm-wide cross-shore bins. The dynamic sand bed level was defined as the running 2-minute minimum for each cross-shore bin, and was used to estimate the depth of the runup tongue. More

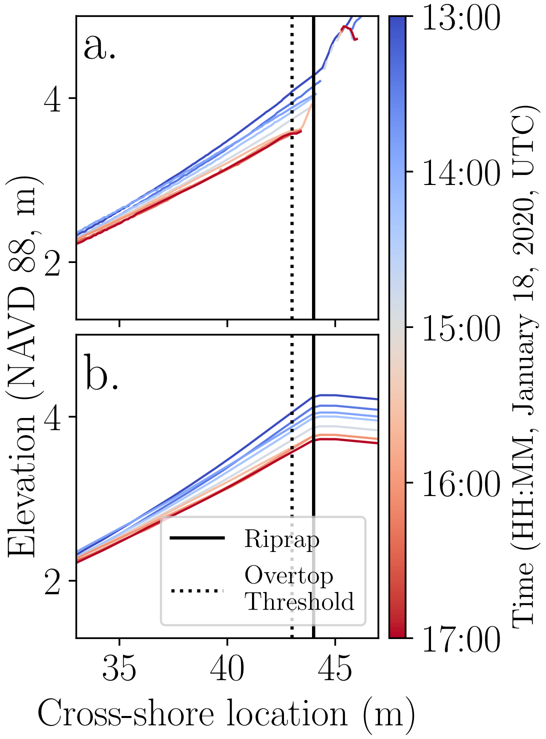

**Figure 1.5.** LiDAR observations of 80 cm of backbeach erosion over 4 hours. The slope in the swash zone erodes from 0.14 to 0.10 over the observing period. (a) smoothed median depth profiles for 28 min. segments, colored by time. MSL (0 elevation) is cross-shore location 0 in Figure 1.3. (b) median profiles with riprap flattened for each segment; yielding the depth profiles used in SWASH. Vertical lines indicate locations of riprap (x=44 m) and the empirical overtopping threshold (x = 43 m). Times given are in UTC.

sophisticated algorithms are sometimes used for bed detection, such as variance thresholds over 4 second windows (Almeida et al. (2015)), but were not practical given the data quality.

We used 30 cm for our runup threshold depth to detect the runup line (Figure 1.6), which is larger than previous thresholds (e.g. 10 cm by Fiedler et al. (2018), 5 cm by Raubenheimer et al. (1996), 2 cm by Almeida et al. (2013), or 1.5 cm by Brodie et al. (2012); Martins et al. (2015)). The same 30 cm runup threshold is used in both the model and observations, so it is a valid model test. Shallower thresholds (¡15cm) used elsewhere are not viable because of O(5 cm) error in bed level extraction and because the

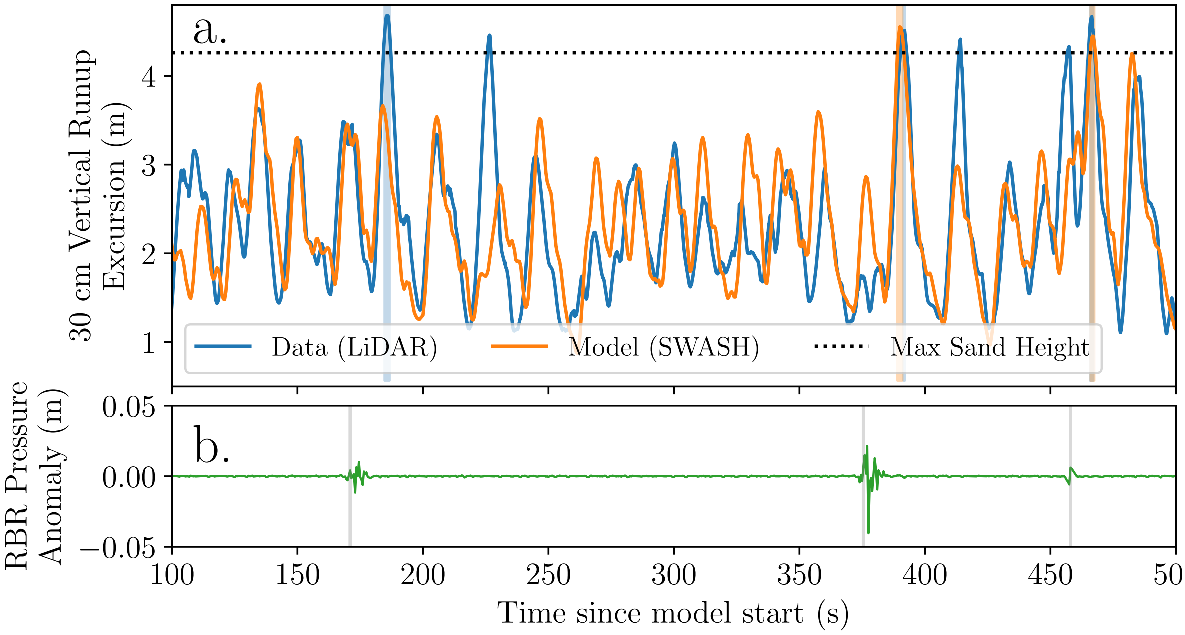

**Figure 1.6.** Example timeseries of LiDAR runup observations vs SWASH, with overtopping measurements. (a) Sample vertical runup versus time for 400 sec around 13:00 (UTC). LiDAR-observed (blue) and SWASH-modeled (orange). The runup edge is defined with 30 cm minimum depth. Shaded vertical bands indicate when an empirical horizontal runup threshold (x = 43 m, see Figure 1.5) is passed, chosen to correlate with RBR overtopping. The dashed horizontal line (elevation 4.1 m) is the elevation at the riprap base. (b) RBR pressure (behind the riprap) versus time, with grey lines showing times of overwash. Though in this sample the LiDAR runup has higher peaks, other segments show the opposite behavior.

narrow beach imposes an upper limit on the instantaneous shoreline (i.e. the instantaneous shoreline reaches the backbeach riprap during overtopping, where it is capped). Changes in observed and modeled runup with threshold depth between 0.15 - 0.35 m (not shown) are similar to previous studies. Model-data comparisons do not depend critically on the 30cm threshold.

The unquantified LiDAR errors are an analysis shortcoming. The LiDAR grazing angle, shadowing by the riprap, and noise from sea spray or vibrations of the balcony degraded data quality. Additionally, the 1550 nm wavelength used is not ideal for the water and wet sand; a shorter 905 nm wavelength (as used by Blenkinsopp et al. (2010)) may have performed better.

### 1.2.3 Runup Model

SWASH, a non-hydrostatic unsteady wave-flow numerical model designed for surf zone processes, was run with two vertical layers, a compromise between accurate linear frequency dispersion and the computational load of many layers (Zijlema et al. (2011)). SWASH was run on a 1D transect, though we used the 2D engine to take advantage of variable cross-shore grid spacing, which varies from 2 m at the seaward boundary to 20 cm at the shoreward boundary. The simulation has 3 along-shore grid points spaced at 1 m, making the model effectively 1D (Fiedler et al., 2018).

SWASH was initialized with the time series of shoreward propagating surface waves observed by the offshore co-located pressure and current sensors (PUV in Figure 1.3a, $\eta+$ in Figure 1.4), surface corrected and separated into shoreward and seaward components (Guza et al., 1984; Fiedler et al., 2019).

Model bathymetry was an ensemble of 8 representative underwater eroded winter profiles on this transect (Figure 1.3b) combined with subaerial profile evolution observed with LiDAR (Figure 1.5). The model back beach bathymetry was the smoothed median bottom profile observed by the LiDAR for each 28-minute burst. Errorbars are the RMS error from different model realizations using different subaqueous bathy-metries. This variation in bathymetry was the largest easily quantifiable source of uncertainty in this analysis.

We use the recommended settings for nonhydrostatic phys-ics and numerics based on the SWASH user manual (as presented in Zijlema et al. (2011)), with wave breaking parameters optimized for 2 vertical layers developed by Smit et al. (2013). Fine tuning model parameters for this study would have risked overfitting because the processes parameterized were not directly observed and many additional factors were not included in the model (see discussion and conclusions).

### 1.2.4 Overtopping

To simulate overtopping, the beach profile was flattened landward of the riprap base (i.e. riprap removed) (Figure 1.5), and the flux onto the riprap estimated. This does not account for how riprap (and whatever is behind it) impedes overtopping, so we consider these estimates to be an upper limit on overtopping volume.

The LiDAR did not directly observe overtopping because the riprap seaward side was shadowed and out of view. As the upper beach eroded over the 5-hr observation period, this shadowed area grew to 70 cm seaward of the riprap (Figure 1.5a). The RBR pressure sensor detected the larger overtopping events at a single point (Figure 1.6b), but it did not accurately measure water depth.

To use the modeled runup line for predicting overtopping at Cortez Ave. specifically (and taking account of the protection offered by riprap which we do not model), it was necessary to relate direct observations of overtopping (the RBR) to related observed phenomena which could be modeled (i.e. runup). RBR overtopping event counts (RBR observed pressure anomalies) were compared with the observed LiDAR runup line. A 2-second boxcar filter was applied to the runup line time series, to reduce jitter. A distance threshold was determined to match numbers of observed lidar runup maxima to overtopping events observed with the RBR. This threshold is when the 30 cm LiDAR runup line reaches within 1 m of the base of the riprap, which is a plausible proximity threshold. This threshold was then used to compare modeled runup to observed overtopping (Figure 1.8).

## 1.3 Results

### 1.3.1 Runup

A representative 400 s time series shows good agreement of SWASH-predicted and LiDAR-observed runup time series (Figure 1.6). There is an unresolved ∼20 sec time

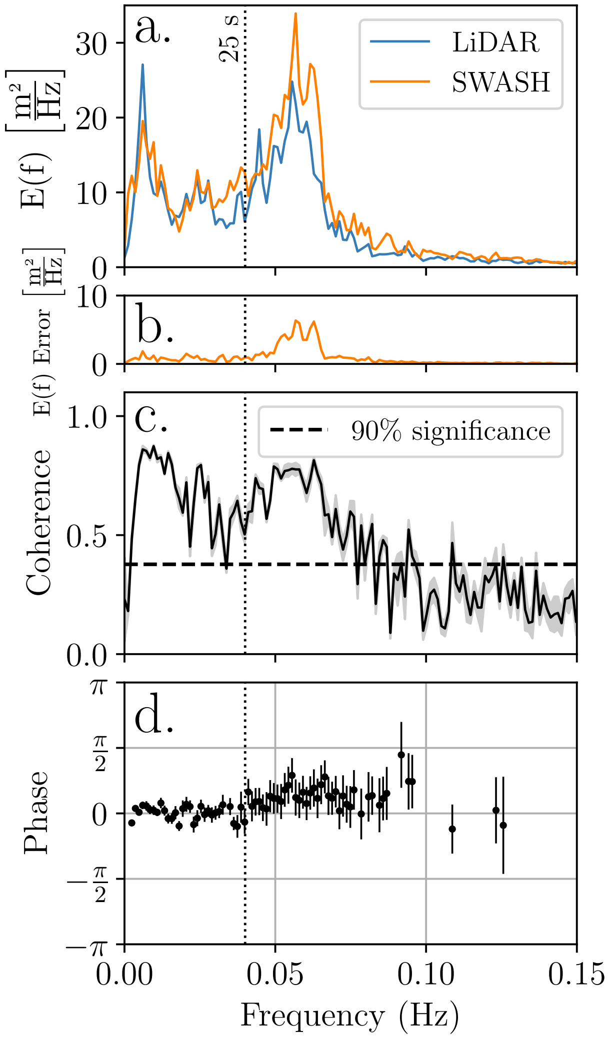

**Figure 1.7.** Spectra, coherence and phase, compared between 4 hours of LiDAR-observed and SWASH-modeled runup at Imperial Beach, CA. SWASH uses a model ensemble (using 8 historic bathymetries), and computations use a 30 cm runup line. (a): Vertical runup spectra $E_{\text{runup}}(f)$. (b): $E_{\text{runup}}(f)$ error (in physical units) using RMS scatter from different model bathymetries, which is by comparison around 10% with a maximum at 20% of the total energy at peak sea swell energies. (c): Coherence and (d): Phase difference (observed-model) when coherence is above the 90% significance. Errors in panels b, c and d are all from RMS scatter of different model bathymetries.

delay between RBR and LiDAR observed overtoppings which we do not know the source of, which may be an instrument clock error or associated with the ~25 m offset of RBR and LiDAR (Figure 1.3a). Negative pressures and smaller than expected (based on visual observation) depths are possibly associated with (compressible) air bubbles in the frothy overwash trapped in the intermittently exposed pressure orifice.

For the entire 252-min record, model and observed runup are in-phase and coherent in both the sea-swell and infragravity frequency bands (Figure 1.7). SWASH overpredicts sea swell energy but agrees better with the observed infragravity energy. In terms of runup parameters, predicted IG and SS wave heights are within 5-6% of observed, but setup at the shoreline is overpredicted by ∼40% (∼20 cm). The overprediction of shoreline setup and sea-swell energy may be related.

The approximately linear phase drift with frequency (to ∼40 deg at 0.1 Hz) is consistent with a ∼1 s time shift of unknown origin, small compared to the ∼60 s travel time from the offshore PUV to the shoreline.

Spectra (Figure 1.7) have ∼36 degrees of freedom, use 14 minute segments with 50% overlap and a cosine taper, and are not sensitive to details in spectral analysis. Errorbars in SWASH sea swell and infragravity wave heights from the RMS of the bathymetry ensemble are plotted in Figure 1.10 (orange), with more modeling scenarios included (see Section 1.3.5). LiDAR errors are unknown.

### 1.3.2 Overtopping

The empirical method discussed in Section 1.2.4 is used to estimate an overtopping rate from the LiDAR-observed runup line, which is tuned to agree with the RBR. The same method is then applied to the SWASH-modeled runup line. Although the overtopping rate inferred from the LiDAR runup line closely agrees with the RBR, SWASH over-predicts overtopping by a factor of 2 (Figure 1.8a). Along with the overprediction of setup, this suggests that dynamics not included in the model are important for accurate overtopping predictions (See Section 1.4).

Only a few overtopping events, which include the largest bores, were matched by all three of SWASH, LiDAR, and RBR. The modeled discharge rate (taken as water flux onto the riprap, which is the upper limit of overtopped volume) peaks at high tide at

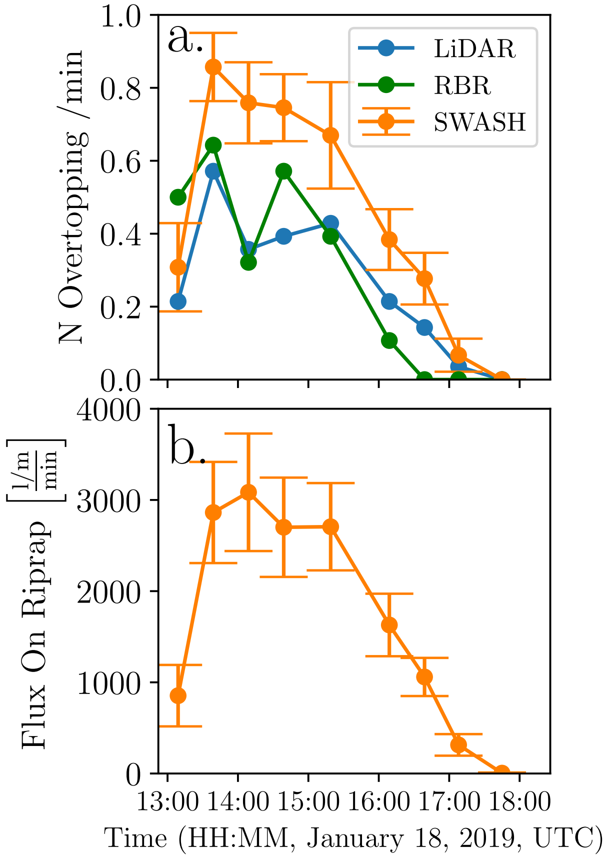

**Figure 1.8.** Overtopping rates measured and predicted by SWASH. (a): Number of overtopping events per minute versus time (UTC), estimated from LiDAR, SWASH model, and RBR (see legend). (b) SWASH model flux onto riprap. For errorbars, we use the RMS of the ensemble of SWASH results using different model bathymetries. Using this method, SWASH overpredicts the overtopping rate by about a factor of 2. The errorbars from the bathymetry ensemble only account for about half the misfit.

3080 l/m/min or 51.3 l/m/s, with an average of 1690 l/m/min or 28.2 l/m/s over the 252 minute record (Figure 1.8b).

### 1.3.3 Error from Bathymetry

The infragravity runup component is sensitive, to unknown and varying degrees, to the subaqueous and subaerial bathymetry. We test for sensitivity using a limited range of variable bathy-metry, plausible for the study beach. For this site, runup is relatively insensitive to offshore bathymetry

Errorbars for SWASH in Figures 1.7, 1.8, 1.9, 1.10 (except for phase error) and 1.11 are adopted from the RMS error of the 8 member underwater bathymetry ensemble, which is the most significant source of easily quantifiable uncertainty, given that the underwater bathymetry was not recently measured. Spectral uncertainty from bathymetry for the 5-hour period in runup is 5-20% of spectral energy density (Figure 1.7b). Runup component uncertainty is 2% for $\mathrm{H}_{\mathrm{IG}}$, 6% for $\mathrm{H}_{\mathrm{SS}}$, and 5% for setup. The errorbars are too small to explain the misfit from SWASH overpredicting overtopping and setup. The misfit in overtopping rate is $\sim$2 times larger than the errorbars on overtopping rate, and for setup the misfit is $\sim$7 times larger than errorbars. This remaining misfit to LiDAR is significant and attributable to the many factors we do not account for, such as LiDAR observation error, 2D surfzone effects, porosity of the beach and reflection on riprap.

### 1.3.4 Offshore Conditions

PUV observations were decomposed into shoreward and seaward wave components, used to estimate observed reflection coefficient (Figure 1.9). The shoreward component was used to initialize SWASH. SWASH output at the boundary was also decomposed into shoreward and seaward wave components. The shoreward component equals the PUV by definition. The seaward component is the SWASH modeled reflected/radiated wave energy.

Here SWASH overpredicts IG wave reflection coefficient by $\sim$40% (Figure 1.9d), despite the fact that the IG component of the 30 cm runup line energy was predicted accurately. Variance from unknown bathymetry was only $\sim$10%, not enough to explain the misfit. We suspect error specifically from unaccounted 2D dynamics, a known cause of infragravity wave overprediction.

The spectra were made with 20 minute segments with 50% overlap and a cosine taper (for a total of 29 segments) but were not sensitive to details of spectral analysis.

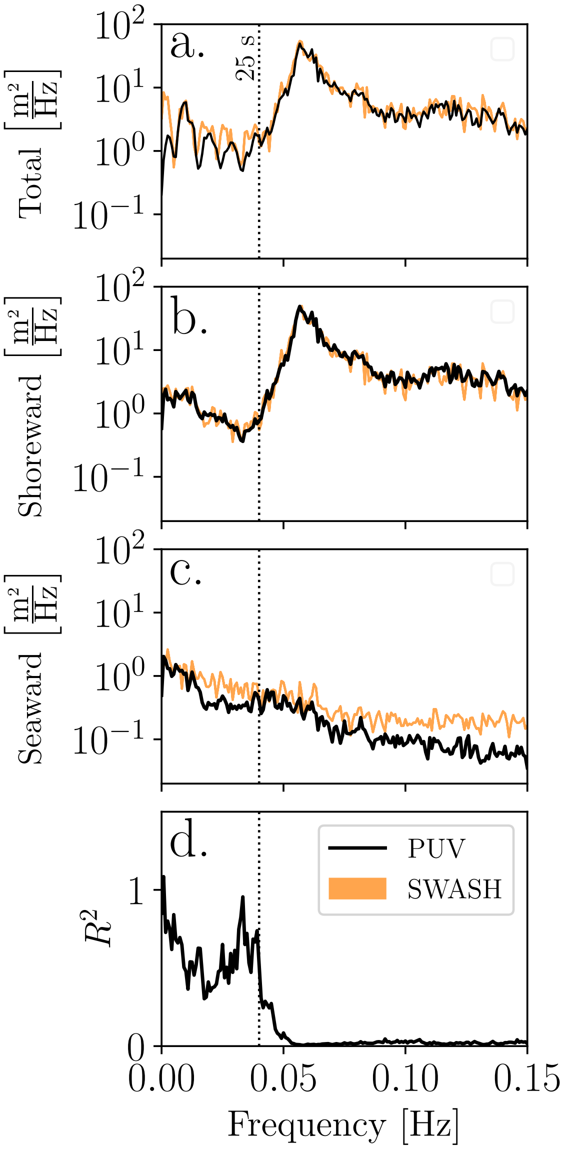

**Figure 1.9.** Sea surface elevation spectra at the offshore boundary (8 m depth, 300 m offshore) observed by co-located pressure and current meter (PUV, black) and modeled by SWASH (orange ) over 5 hours. (a): Total waves. (b): Shoreward propagating waves. Agreement is expected because PUV spectra are used for model boundary conditions. (c): Seaward propagating waves. (d): Reflection coefficient, the ratio of Seaward / Shoreward spectra. In all panels SWASH is plotted as the region between the mean plus and minus the RMS error from different model bathymetries.

### 1.3.5 Cases With Reduced Information

Because detailed observations of backbeach erosion or phase-resolved ingoing waves are often not available in field conditions, we also considered modeling cases where the 80 cm of backbeach erosion (Figure 1.5) is ignored (Figure 1.10, red), or ingoing wave phases are randomized (Figure 1.10, purple).

In the case of non-eroding bathymetry, the same ensemble of underwater bathymetries was used to estimate uncertainty, but a non-eroding backbeach was used. Overtopping in this case is suppressed (Figure 1.11), perhaps because the erosion decreases the beach slope (from $\beta$ ∼0.14 to ∼0.10). With a lower slope, less momentum is required to reach the top of the beach and overtop. The difference between the estimates grows as the erosion progresses, and reduces the rate of overtopping by up to half by the third hour. This demonstrates at least that short term erosion can be a significant factor in flood volumes, though model validation is still limited.

The observed erosion decreased the beach slope by stripping away the back beach. Though a parametric model like Stockdon 2014 would indicate a lower R2% from decreased beach slope, the berm height to be climbed by overtopping is decreased, and (in the SWASH model) more overtopping occurs. The apparent improvement in model fit results from error cancellation.

In the case of randomized phase, a grid of 64 models (8 bathymetries by 8 randomized phase sets) was used. This test examines the (common) case when only wave spectra (lacking phase information) are available at the outer boundary. When initial phases are assumed random, the accuracy of runup simulations decreases.

To randomize phase, waves are assumed to be linear and uncoupled at the 8 m deep boundary (rather than assuming any nonlinear wave shape), and the same offshore spectrum ($\eta+$ in Figure 1.4) is used to generate a time series of ingoing waves. To determine error from one source, the ensemble is averaged on the other source.

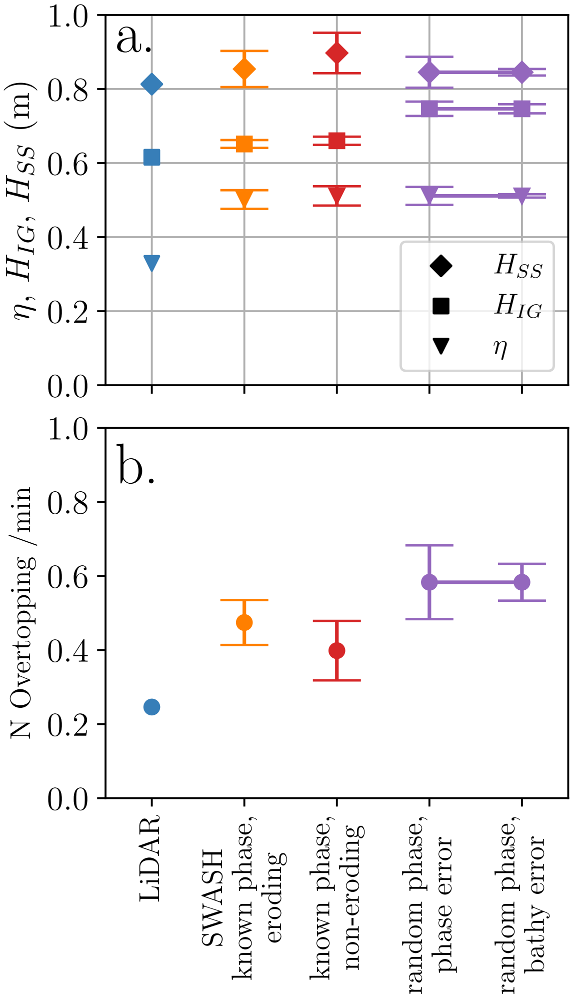

**Figure 1.10.** Overview of observed and SWASH-modeled bulk parameters, with uncertainties, for different modeling configurations. (a): setup at the shore line, and sea swell and infragravity wave heights (divided at 0.04 Hz or 25 seconds) derived from the vertical runup line, and (b): overtopping rate per minute. Left to right are LiDAR observations (blue), SWASH using all available information (orange), removing backbeach erosion information (red), and removing phase information (purple). Except for the last case (purple), all errorbars represent RMS error from the underwater model bathymetry ensemble. In the case of removed phase information (purple), the left errorbar corresponds to the RMS error from the randomized boundary condition phase ensemble (averaged on bathymetry), and the right errorbar corresponds to the RMS error from the bathymetry ensemble (averaged on phase). Notably the error for overtopping rate from randomizing phase is about 2x larger than the error from unknown bathymetry. For all SWASH models, setup was predicted to be about 1.5x larger than LiDAR observed.

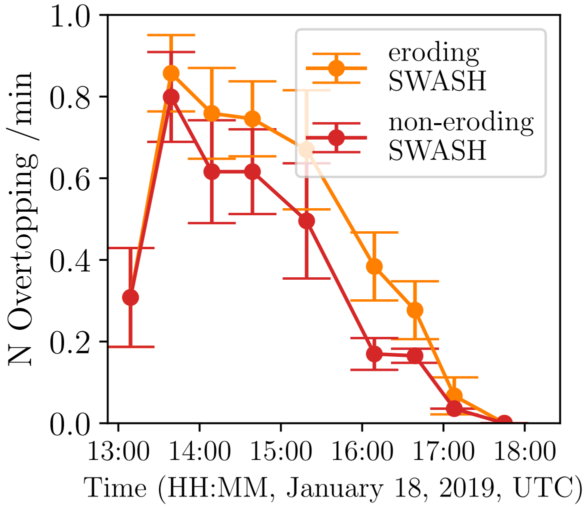

**Figure 1.11.** Overtopping rates predicted by SWASH with an eroding (orange) or static (red) backbeach bathymetry versus time (UTC). Over 4 hours, 80 cm of erosion were observed by LiDAR (see Figure 1.5). By the end of the simulation (where the difference between the eroded and non-eroded backbeach is greatest) static backbeach SWASH predicts ∼50% less overtopping than eroding backbeach SWASH.

For example, consider the case of calculating bathymetry RMS error. For each bathymetry, there are model outputs from 8 different randomized-phase boundary conditions. These 8 model outputs are averaged, leading to one model output for each bathymetry, averaged on phase. The RMS of this 8-member ensemble is the uncertainty from varied bathymetry.

Notably, the uncertainty from the randomized phase (∼20%, Figure 1.10, purple, left) is not large, but is larger by a factor of 2 than uncertainty from the bathymetry (∼10%, Figure 1.10, purple, right). Randomizing phase also leads to greater overprediction in infragravity runup, increasing the misfit from ∼6% to ∼20% (shown as the increase in infragravity height of the random phase case in Figure 1.10a). This shows how phase-related errors would become the most significant source of uncertainty in the model if phase was randomized.

The effect of errors in infragravity offshore boundary conditions (phase and amplitude) on runup is not well understood (Gomes da Silva et al., 2020). Nonlinear effects couple infragravity and sea swell phase (i.e. groupiness), and the relatively short model domain ($\sim$300 m) is insufficient for waves to evolve from unrealistic randomized phasing (used in this randomized phase test) to realistic coupled phasing (observed by the offshore instrument). We believe this explains the additional misfit in infragravity runup from randomized phases in the boundary conditions. Note that moving the offshore boundary condition to deeper water would decrease the importance of including phase-coupling at the boundary, but increase the importance of neglected 2D effects.

Overall, reduced information did not alter bulk runup statistics much, suggesting other unaccounted factors were more significant. The relative importance of errors in wave boundary and/or bathymetry that degrade 1D model performance vary on the conditions and their relative uncertainties. For example, Gomes da Silva et al. (2020) showed that runup is substantially altered by changes in subaqueous bathymetry much larger than considered here.

## 1.4 Discussion & Conclusion

Five hours of runup and overtopping observed with a scanning LiDAR and backbeach pressure sensor agree with predictions of the numerical model SWASH in 1D, initialized with a time series of shoreward propagating waves observed $\sim$300 m offshore. Previous field studies showed SWASH yields good estimates of runup bulk characteristics (e.g. Smit et al. (2014), Rijnsdorp et al. (2014), Buckley et al. (2014), Fiedler et al. (2018, 2020)). We show the model-data agreement also includes runup phases and overtopping within a factor of 2. Enabled by improved (LiDAR) observations, the model-observation misfit is smaller than in previous field estimates (Gallien, 2016), and comparable to lab studies (Suzuki et al., 2017) , though still significant. Overtopping predictions vary widely from empirical parametrizations (Shaeri and Etemad-Shahidi, 2021), to numerical models (Matias et al., 2019), to qualitative predictors (Stokes et al., 2021). Quantitative field validation of overtopping models are rare, and understanding of the relative influence of IG wave phase is limited. The runup model performance is surprisingly insensitive to changes in subaqueous bathymetry as well as the wave-by-wave match with observed runup, given the not particularly narrow wave directional spread

We also show that poorly modeled dynamics can cancel, especially for bulk statistics with limited validation. For example, omitting short-term erosion improved the apparent accuracy of the model overtopping estimate, but this is not model improvement. We might have increased model friction to improve fit, and friction is certainly an unknown factor, but the misfit could equally well be from lack of 2D dynamics. In a model with many simplifications, chasing optimal model fit by parameter tuning or adding empirical corrections can be problematic, because the quality of validation prevents adequate separation of error sources.

We also tested the impact of randomizing phase, and showed that in our case a lack of phase coupling in boundary conditions can be more important than unresolved variations in bathymetry. However, this test was limited by a relatively short 300m cross-shore model domain. Sensitivity to phase-coupling at the offshore boundary was much reduced when the offshore boundary was located 1200m offshore of a low-soope, high energy beach (Fiedler et al., 2019).

Work remains to improve both the model and validation. Model physics would be improved by accounting for wave reflection and blockage by riprap, seepage into permeable sand, and 2D dynamics, either by modeling these dynamics directly or quantifying their contribution towards model uncertainty when omitted. Model validation would be improved by studying LiDAR error and expanding to more sites and wave conditions. Realistic error estimates for the dynamics underlying bulk statistics are a necessary prerequisite for identifying model deficiencies.

This qualitative model-data overtopping comparison represents a significant step forward towards quantitative validation of phase resolving wave models in field conditions.

These improvements are enabled (and limited) by the model and observations used.

Significant unresolved challenges in 2D modeling precluded straightforward extension of our 1D simulations. Preliminary 2D model tests raised issues of model domain size, frequency resolution, periodic alongshore boundary conditions, numerical instabilities, and large computational costs, which are particularly vexing for IG waves. Further progress also will require improved observations of the offshore boundary conditions and 2D bathymetry. Nevertheless, the encouraging comparisons between the 1D model and observations at Imperial Beach suggest that quantitative phase resolving model simulations are achievable in realistic field settings.

## Acknowledgements

This study was funded by the U.S. Army Corps of Engineers (W912HZ1920020) and the California Department of Parks and Recreation, Natural Resources Division Oceanography Program (C19E0026). Data was collected and processed by Center for Coastal Studies field team members Lucian Parry, Rob Grenzeback, Kent Smith, Brian Woodward, Greg Boyd, and Mele Johnson. Laura Engeman and Michele Okihiro organized logistics. This manuscript was greatly improved by the helpful comments of two reviewers.

Scripps Institution of Oceanography and the city of Imperial Beach are built on unceded territory of the Kumeyaay Nation. Today, the Kumeyaay people continue to maintain their political sovereignty and cultural traditions as vital members of the San Diego/Tijuana Community. We acknowledge their tremendous contributions to our region and thank them for their stewardship.

Chapter 1, in full, is a reprint of the material as it appears in Coastal Engineering 175 (2022). Cassandra S. Henderson, Julia W. Fiedler, Mark A. Merrifield, R.T. Guza and Adam P. Young, 2022. The dissertation author was the primary investigator and author of this paper.

# Chapter 2

# Bayesian Analysis of Infragravity Edge Waves

## Abstract

Infragravity edge waves on a moderately sloped ocean beach are characterized using 60 days of observations with low-to-moderate energy incident waves. Pressure (P) and colocated biaxial current meters (UV) were deployed from the shoreline to 30m depth, with an 8-element PUV array in 7 m depth spanning more than 1 km alongshore. Data were analyzed with a Bayesian Maximum a Posteriori method (MAP) that inverts (into linear shallow water modes) observed PUV cross-spectra including sensors separated in both alongshore and cross-shore directions. Estimates with MAP concur with previous studies using Maximum Likelihood Estimator and suggest edge waves often contain up to 50% of the along-shore velocity infragravity variance in 7m depth. When compared to non-hydrostatic numerical wave model SWASH (run on a 1D transect, initialized in 15 m depth, 1 km offshore), MAP estimates low mode edge waves are 10-25% of the runup variance. 5 days with LiDAR runup observations give similar results. Edge waves are more energetic at high tide (when the shoreline slope is largest), possibly due to a steep beach supporting multiple constructively interfering shoreline reflections, which are required to form edge waves with ray theory. SWASH in 1D generally overpredicts infragravity waves while by definition excluding edge waves, errors that partially cancel in predicted runup

frequency spectra.

## 2.1 Introduction

Infragravity (IG) waves are long period waves (25 to 250 second) generated by nonlinear, long period variations in the momentum flux of incident sea swell wave groups in shallow water. In this near-resonant triad, two incident sea swell (SS) waves with similar frequencies interact with a long third wave at the difference frequency. IG energy is ubiquitous on the shoreline, can dominate the runup during storms, and contributes to overtopping.

Model forecasts of runup of wave overtopping are often based on simplistic empirical models that consider only incident wave bulk properties (e.g. wave height and peak period) and neglect the effect of sandbars and offshore depth variations (e.g. Stockdon et al. (2006)) More sophisticated dynamics-based spectral models that include cross-shore depth variations and nonlinear IG wave generation and dissipation accurately predict infragravity wave runup and overtopping in laboratory flumes (Lashley et al., 2020). Waves incident on the domain are specified for both IG and SS waves. In these so-called 1D models, SS and IG waves propagate in the cross-shore direction only. However, natural SS waves are spread in direction with finite crest length. Existing observations show that infragravity waves are also directionally spread, with energy sometimes concentrated on the $k_y$-$f$ dispersion curves of topographically trapped edge waves.

First identified by Stokes (1846), edge waves are a normal mode of the surfzone. Infragravity edge waves were first connected to surf beat / nonlinear forcing by Gallagher (1971), and various linear array techniques (cross-shore: phase, node/antinode structure (Guza and Thornton, 1985) and alongshore: MLE and IMLE (Huntley et al., 1981; Oltman-Shay and Guza, 1987), and both (Sheremet et al., 2001)) were used to estimate that edge waves can occupy up to 50% of shoreline variance, though usually significantly less. Despite this, edge waves are systematically ignored by 1D methods, which perform well without them (e.g. Chapter 1). Our study builds on previous techniques for characterizing edge waves and compare results with a 1D method (SWASH) to ask: where is the contradiction?

Field observations and methods designed to determine the importance of edge waves to infragravity wave elevations and horizontal velocity are described. IG waves are briefly reviewed in the remainder of section 2.1. In section 2.2, the Runup Bathymetry 2D experiment (RUBY2D) is presented and observations are summarized. In section 2.3, Edge wave shapes are computed for Torrey Pines using observed bathymetry and a Bayesian cross-spectral inverse method for detecting and differentiating shallow water modes is presented. The forward (mode amplitudes to observed cross spectra) and inverse problems (observed cross spectra to mode amplitudes) are discussed. In section 2.4, edge waves are quantified and compared to SWASH and a technique adapted from Oltman-Shay and Guza (1987). Edge waves are estimated to be 10- 25% of runup and 25-35% of IG variance in 7m depth. In section 2.5, we relate edge wave excitation to tide level and incident wave size, and rationalize the relative accuracy of runup predicted by 1D phase-resolving models (SWASH 1D), despite neglecting edge waves. The appendices includes details of the instrumentation, processing, and SWASH 2D model test results.

### 2.1.1 IG Energy Balance

Generation by groups of sea and swell, dissipation, shoreline reflection, and refractive trapping have all been suggested to contribute significantly to the infragravity energy balance in shallow, nearshore waters (Munk, 1949; Longuet-Higgins and Stewart, 1964; Gallagher, 1971; Suhayda, 1974; Huntley et al., 1981; Herbers et al., 1994, 1995a; Ruessink et al., 1998; Henderson and Bowen, 2002; Janssen et al., 2003; Battjes et al., 2004). The nearshore dynamics of IG waves have been widely studied during the past decades through theoretical, laboratory, field and numerical efforts (see Bertin et al. (2018) for a recent review).

Various theories have been developed to explain the substantial growth of IG waves in the nearshore (Symonds et al., 1982; Schäffer, 1993; Janssen et al., 2003; Nielsen and Baldock, 2010; Contardo et al., 2021; Liao et al., 2021). Such theoretical background combined with numerical modeling (Reniers et al., 2002; Van Dongeren et al., 2003; Lara et al., 2011), laboratory experiments (Boers, 1997; Baldock et al., 2000; Baldock and Huntley, 2002) and field campaigns (Okihiro et al., 1992; Herbers et al., 1994, 1995b,a), has significantly advanced our understanding of the IG wave patterns, growth rates, dissipation and phase relationship with SS wave groups (Battjes et al., 2004; Van Dongeren et al., 2007; De Bakker et al., 2016).

A weakly nonlinear IG wave energy balance based on near-resonant triads explains much of the observed cross-shore variation of IG energy flux (Henderson and Bowen, 2002; Henderson et al., 2006; Ruju et al., 2012; Guedes et al., 2013; Rijnsdorp et al., 2015; Mendes et al., 2018). De Bakker et al. (2015, 2016) used a nonlinear Boussinesq energy balance to show that nonlinear interactions between two IG and one SS component can become significant and must be included to explain the loss of IG flux near the shoreline where the IG and SS wave heights are similar. Interactions between three IG components have also been detected on mild sloping beaches (Van Dongeren et al., 2003).

In deep and intermediate depths, the non-resonant triad results in a relatively small (formally 2nd order) bound IG wave in antiphase with groups of SS waves (Longuet-Higgins and Stewart, 1964). Observed bound wave crests coincide with a minimum in the sea-swell envelope (Okihiro et al., 1992; Herbers et al., 1994). Previous studies have shown the bound Infragravity energy in 10-15 m depth in Southern CA is typically only 10-30% of the energy. The remainder is free infragravity waves believed to be refractively trapped on the shelf, seaward of 10-15m depth (Okihiro et al., 1992; Herbers et al., 1995b; Lange et al., 2023b).

The bound wave is sometimes described as being "released" when the coupled SS wave group breaks or as "progressively released" in shallow water regardless of breaking

(Baldock, 2012). A spectral energy balance (Rijnsdorp et al., 2022) accounts for all mechanisms potentially transferring energy between SS and IG waves, including shoaling bound waves, excitation of free IG waves over a sloping bed and breakpoint generation. However, in the spectral approach these mechanisms are represented as either contributions to nonlinear flux gradients or nonlinear interactions, and the dominant mechanisms driving the interaction are not identified. Numerical simulations suggest inclusion of an offshore bound wave is often not necessary to reproduce observed energy balances in the inner surfzone (Fiedler et al., 2018).

### 2.1.2 Reflection, Tides, and Edge Waves

Infragravity waves can strongly reflect at the shoreline, but also can gain and lose energy through nonlinear transfers with sea swell waves and perhaps break in the inner surfzone (Sheremet et al., 2002). On beaches with a convex profile, the inner surfzone and shoreline slopes are low at low tide, and favor high dissipation and nonlinear transfers from IG to SS waves (Thomson et al., 2006). Tidal changes in depth profile, and IG energy and reflectance (often quantified as the reflection coefficient, the ratio of outgoing to incoming energy flux) are well documented (Okihiro and Guza, 1995; Thomson et al., 2006; Smit et al., 2018; Bertin et al., 2020; Matsuba and Shimozono, 2021)

This reflected energy propagates seaward and can either travel freely from the shoreline across the shelf to deep water (known as ‘leaky’ waves, Webb et al. (1991); Aagaard and Holm (1989); Ardhuin et al. (2014); Lange et al. (2023b)), or become ‘trapped’ along the shelf, due to back-refraction by the increasing water depth (Huntley et al., 1981; Guza and Thornton, 1985; Oltman-Shay and Guza, 1987; Oltman-Shay and Howd, 1993; Thomson et al., 2006). These trapped waves are sensitive to geography, with the amount of trapping depending on the continental shelf and beach topography (Herbers et al., 1995b; Smit et al., 2018).

Torrey Pines State Beach, CA has long been a study site for refractively trapped waves (Huntley et al., 1981; Guza and Thornton, 1985; Oltman-Shay and Guza, 1987; Okihiro et al., 1992; Thomson et al., 2006), with significant trapped IG energy detected shoreward of 15 m water depth. This refracted energy then propagates back onshore as free waves. These trapped waves are not phase-coupled to local (instantaneous) SS wave groups because they are not locally generated. Our inverse model estimates ambient IG edge wave energy, but the energy source is not identified.

A sloping beach is a wave guide for edge waves, with shoreline reflection and refractive trapping offshore creating cross-shore standing, alongshore propagating waves confined to shallow water (Eckart, 1951). Edge waves can be derived as sums of trapped (oblique from shore-normal), fully reflected free waves which constructively self- interfere. Edge waves, nearshore free waves, are quantized into modes, with mode 0 having the shortest alongshore wavelength $y$ (and largest alongshore wavenumber $k_y$). The mode number counts the number of zero crossings before the edge wave decays. At a single frequency, non-decayed edge waves have similar cross-shore structures, with nodes and antinodes at approximately the same locations, making them difficult to differentiate in the cross-shore.

Gallagher (1971) first noted that infragravity edge waves can be theoretically generated through nonlinear difference wavenumber/frequency interactions at the edge wave wavenumber and frequency. Infragravity edge waves may also be generated by breakpoint forcing (Lippmann et al., 1997), refraction and scattering on irregular bathymetry and by tsunamis and wind (effects not considered here).

Previous studies (Huntley et al. (1981); Oltman-Shay and Guza (1987), and many others) using alongshore linear arrays in shallow water to measure energy at edge wave $k_y$ were limited by array length and depth, but suggested edge waves can be up to 50% of the runup energy, though typically less Oltman-Shay and Guza (1987). Previous studies also used cross-shore arrays to examine the cross-structure of edge wave and leaky wave modes (Gallagher, 1971; Huntley, 1976; Guza and Thornton, 1985). Sheremet et al. (2001, 2002) estimated directional spectra, including edge waves, from a 2D (extending both along-shore and across-shore) array of PUV using a nonlinear least squares, using a relatively dense but short array, with a particular focus on fitting the unknown cross spectral structure of progressive waves. The few quantitative observations of infragravity edge waves are generally consistent with the present results. Edge waves have been shown to become more important for pocket beaches (Özkan Haller et al., 2001) and estuaries (Uncles et al., 2014) where they may be selected for by favorable bathymetry.

This study uses a least squares inversion of the second order statistics (the cross-spectra) observed by a 2D (cross-shore and along-shore) sensor array of pressure and current meters. Similar techniques have been used for coastally trapped waves (Haines et al., 1991; Middleton and Black, 1994), internal tides (Kachelein et al., 2022), and many more (Wunsch, 2006). Specifically, Bayesian Maximum a Posteriori method (MAP) (Van Trees, 2001) is used. Like Sheremet et al. (2001), this method estimates edge wave amplitudes with a least squares inversion, but rather than using nonlinear least squares, a conservative model prior is used, which allows the method to focus on the specific contribution of edge waves to the cross spectra.

Edge waves in field-like conditions have been modeled numerically with phase-averaged models (Van Dongeren et al., 2003; AJ et al., 2006), but phase-resolving models with along-shore variations are still challenged by computational and methodological limitations, including the wavemaker, offshore boundary condition, and large required domain size (Fiedler et al., 2018; Van Dongeren et al., 2003). Additionally, the importance of real (rather than model artifact) alongshore coherence of incident waves is unknown, but dynamically impactful on alongshore wave processes (Salatin et al., 2021). SWASH 2D (see Appendix B) was used to simulate lab type infragravity edge waves, but was troubled by wavemaker issues and higher order harmonic/subharmonic phase-coupled edge wave motions, which raise questions for future edge wave numerical modeling.

## 2.2 Observations

The Runup Bathymetry 2D experiment (RUBY2D) was conducted from October 2021 to February 2022 at Torrey Pines State Beach in Southern California (Figure 2.1a). The beach is a mixture of sand and cobbles and was relatively alongshore uniform (Figure 2.1b), with a concave cross-shore profile backed by riprap (Figure 2.1c). With 2.5 m spring tides (from -0.43 m to 2.19 m), shoreline slopes are significantly higher at high tide ($h'(0) \approx 0.08$) than low tide ($h'(0) \approx 0.025$) (Figure 2.1). Cobble coverage was intermittent and typically only seen above MSL (Matsumoto et al., 2020; Young et al., 2023).

Subaqueous bathymetry was measured approximately every other week on transects spaced 100m apart and extending to 15m depth, spanning 2.3 km alongshore (Figure 2.1b, MOPs 567-590). Subaerial sand levels were surveyed (usually with a scanning LiDAR) approximately every other day. The variation of water depth at each sensor with changing tide and bathymetry was accounted for in estimates of mode structure. Tidal effects are of interest, and the methods used later require a number of records to be statistically significant, tidal qunitiles will be used for analysis (1500 hours broken into 5 × 300 hour chunks, binned by average depth over 90 minute records).

RUBY2D included co-located pressure (P) and current (UV) meters in approximately 7, 10, 15, and 30m depth (denoted PUV7, PUV10, etc.) and pressure sensors (P0) at approximately 0m NAVD88 (approximately MLLW). The CDIP wave model output point (MOP 582, O'Reilly et al. (2016)) is used as the alongshore origin (Figure 2.1b). The Torrey Pines Outer CDIP buoy in 500m depth is used to characterize offshore sea swell waves.

PUV array derived bulk wave characteristics are typical of Southern California. Figure 2.2 shows a subset, and includes significant sea swell ($H_{SS}$) and infragravity wave heights ($H_{IG}$), directional spread, and infragravity reflection coefficient ($R_{IG}^2$, see Sheremet et al. (2002)). Infragravity energy and reflection coefficient are highest at high tide, typical

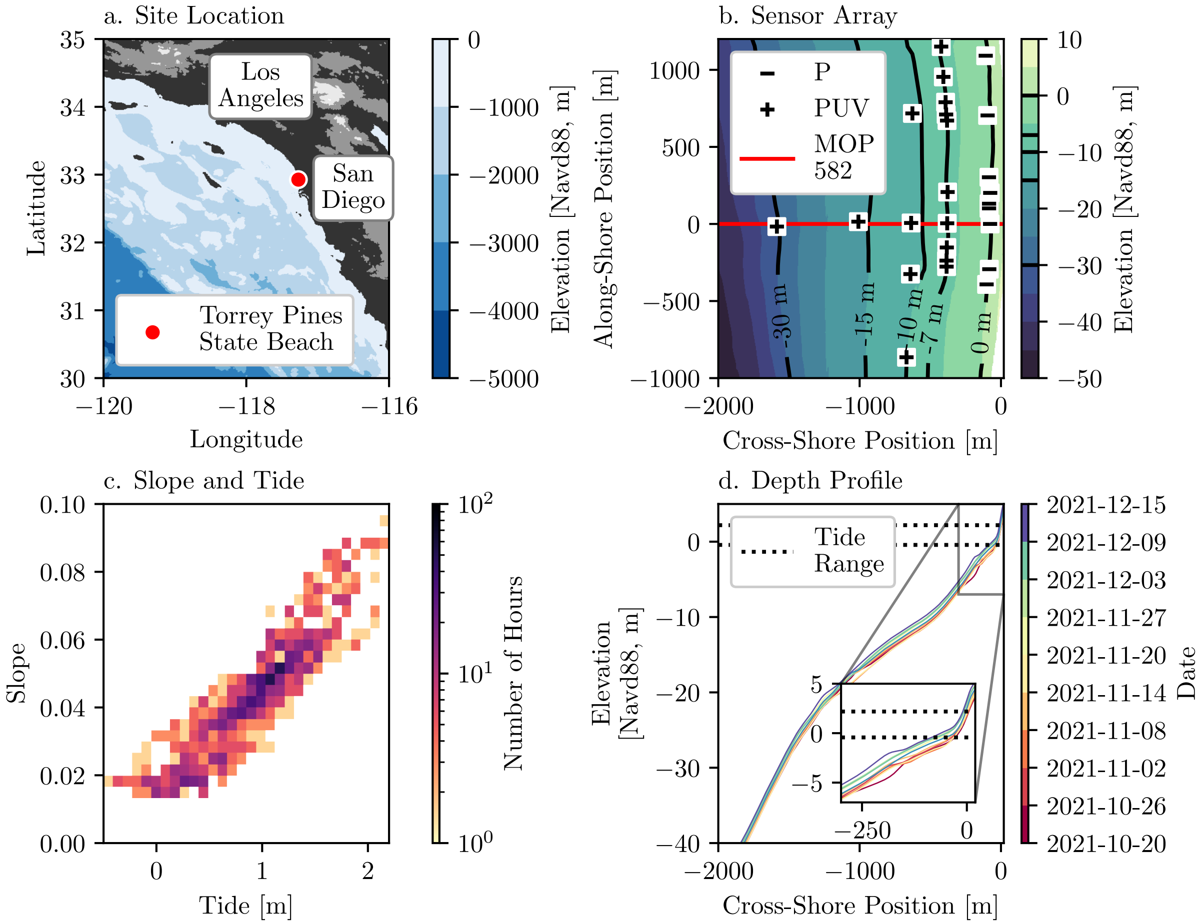

**Figure 2.1.** Layout of RUBY2D Experiment. (a): RUBY2D location at Torrey Pines beach in Southern California. (b): location of sensors; P (pressure) and PUV (colocated pressure and current). CDIP wave model output is 10m depth on MOP transect 582 (red line). (c): histogram (see color scale) of shoreline slope versus tide during RUBY2D. Shoreline slope varied between 0.02 (lowest tide) and 0.08 (highest tide). Shoreline slope is averaged over 20m cross-shore and 1000m along-shore.(d): bathymetric profiles on MOP 582, with inset near shoreline, show the characteristic Torrey Pines concave/convex high/low tide bathymetry.

of Southern California beaches with concave bathymetry and high slope at high tide (Okihiro and Guza, 1995; Lange et al., 2023b). Two relatively energetic wave events ($H_{SS} > 2.5$ m, 10/25 and 12/15) were observed. In the inner surfzone (low tide P0), sea swell waves are broken and $H_{SS}$ is accordingly small – therefore P0 observations of $H_{SS}$ are highly tidal. The presence of standing waves, possibly edge waves, were indicated by nodes and antinodes in the frequency spectra. The quantity $\sqrt{H_0 L_0}$ is used as an indicator of incident wave energy. This quantity is similar to the Iribarren number and often used to empirically estimate wave runup (Stockdon et al., 2006), and is used here because it is also independent of tide. Accordingly large wave observations are associated with higher $\sqrt{H_0 L_0}$. The directional spread narrows as waves propagate into shallow water, and as tide changes, owing to refraction.

A drone-mounted LiDAR measured wave runup along the MOP582 transect on 5 days, with 5 25-minute hovers daily spanning a range of conditions (Figure 2.3). Data were collected and processed following (Fiedler et al., 2021). The vertical position of the runup line is obtained using a running minimum to detect the sand bed, then computing the moving 10 cm depth line (similar to Henderson et al. (2022)).

Spectra are calculated with 90 minute records and 800 second segments (800 second segments are then linearly detrended to remove tide), for 6 non-overlapping segments with 12 degrees of freedom at each frequency, with frequency resolution of 0.00125 Hz, and 28 infragravity frequencies between 0.004-0.04 Hz. To preserve maximal phase information, which is necessary for our method, spectra are not tapered (see Guerci (1999); Dodson-Robinson et al. (2022)), and therefore not overlapping. Sensor locations and processing details are in the Appendix.

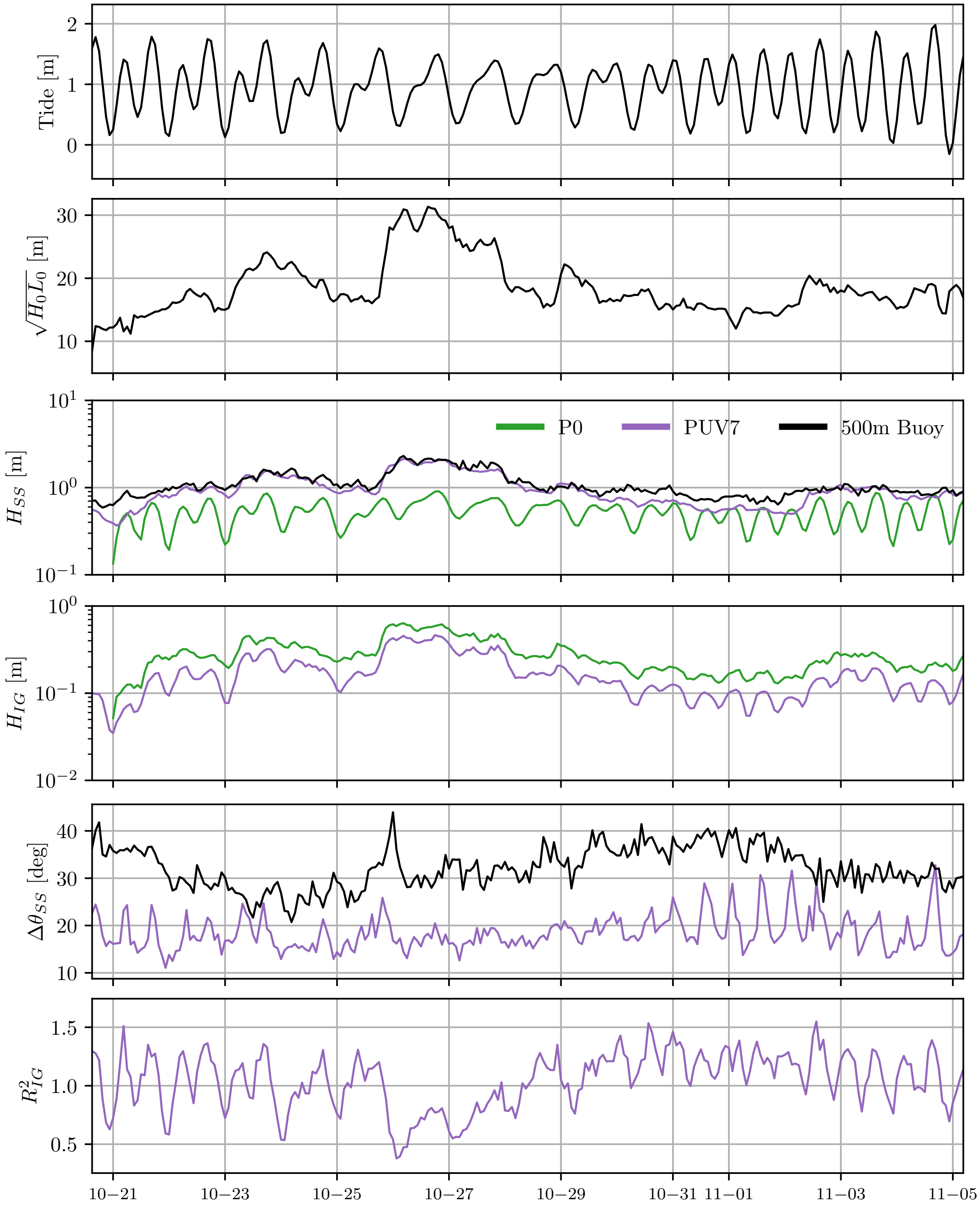

**Figure 2.2.** First 25% of Runup-Bathymetry 2D Experiment (RUBY2D) conditions, from October 21 to November 5, 2021. Time series (90 minute averages) of (a): Tide (Navd88). (b): offshore buoy $\sqrt{H_0 L_0}$. (c) $H_{SS}$ (P0 is in the swash/inner surf zone with depth-limited and strongly tidal $H_{SS}$. PUV7 is in 7m depth). (d): $H_{IG}$ (e) Sea swell directional spread derived from MEM (Lygre and Krogstad, 1986). Two depths are shown PUV7 and P0 (which does not measure spread and reflectance). (f) Infragravity reflection coefficient in 7m depth.

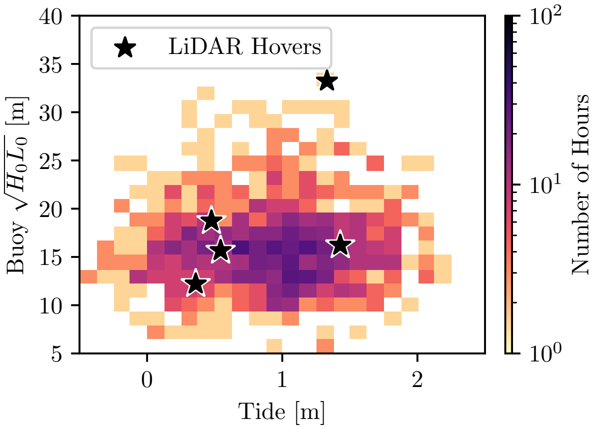

**Figure 2.3.** Number of hours (color bar) of wave $\sqrt{H_0 L_0}$ and tide level during the 2 months (1500 hours) of observations. Stars indicate LiDAR-observed runup . Data are divided into 997 (90 minute) records.

## 2.3 Methods

### 2.3.1 Edge Wave Shapes & Dispersion

For a fixed frequency, a linear shallow water wave on an alongshore uniform beach with complete shoreline reflection has velocity potential

$$\phi(x, y, t) = \left(-i\frac{g}{\omega}\right)\ a\Psi(x)\ e^{-i(\omega t\ +k_y y+\theta)} \tag{2.1}$$

where $a$ is shoreline amplitude, $\omega$ angular frequency, $k_y$ alongshore wavenumber, $\theta$ (random) phase, and $x, y$ are cross and along-shore positions ($x = 0$ is the shoreline). $\Psi(x)$, the cross-shore standing wave structure (at some frequency $\omega$) satisfies

$$\Psi''(x) + \frac{h'(x)}{h(x)}\Psi'(x) + \left[\frac{\omega^2}{gh(x)} - {k_y}^2\right]\Psi(x) = 0 \tag{2.2}$$

with cross-shore depth profile $h(x)$, shoreward boundary conditions $\Psi(0) = 1$ and $\Psi'(0) = -\frac{\omega^2}{gh'(0)}$ (no flow through the boundary), and seaward boundary condition $\lim_{x\to\infty}\Psi(x) \neq \infty$. Owing to the linear shallow water equations, particle velocities from $\nabla\phi = \overrightarrow{u} = (u, v)$ are depth-uniform, and surface elevation $\eta = -\phi_t/g$. Resulting surface elevation and horizontal currents are:

$$\eta(x,y,t) = \qquad a\Psi(x)\ e^{-i(\omega t\ +k_y y+\theta)} \tag{2.3}$$

$$u(x,y,t) = -\left(i\frac{g}{\omega}\right) \quad a\Psi'(x)\ e^{-i(\omega t\ +k_y y+\theta)} \tag{2.4}$$

$$v(x,y,t) = -\left(\frac{g}{\omega}\right)\ a\ k_y\Psi(x)\ e^{-i(\omega t\ +k_y y+\theta)} \tag{2.5}$$

The above waves are standing in the cross-shore and propagate alongshore. $\eta$ and $u$ are also out of phase, while $\eta$ and $v$ are in phase. Progressive shoreward or seaward IG waves associated with nonlinear generation, dissipation, and incomplete shoreline reflection are excluded.

This eigenvalue problem has a discrete set of solutions for $\Psi(x),\ k_y$ that depend on $h(x)$ and $\omega$, which we obtain using the shooting method. Solutions are either a shore-normal wave ($k_y = 0$), leaky oblique waves ($\frac{\omega^2}{g} > |k_y| > 0$), or edge waves ($|k_y| > \frac{\omega^2}{g}$), which are trapped in shallow water and decay in $x$. Edge wave modes are numbered by the number of zero crossings in edge wave $\Psi(x)$.

Mode 0,1 and 2 edge wave shapes for $\eta(x,y),\ u(x,y),\ v(x,y)$ (highest tide quintile averaged bathymetry) are plotted in Figure 2.4, showing how $\Psi(x)$ between modes are similar until decayed (Guza and Inman, 1975). A 3D depiction of the same is given in Figure 2.5.

Numerical solutions for $k_y$ and $\Psi(x)$ use along-shore averaged $h(x)$, with regularly updated bathymetric observations accounting for erosion/accretion and dynamic tide levels. Changing tide levels on the concave beach significantly affect mode shape near the shoreline. Changes in $\Psi(x)$, $k_y$ due to tide are demonstrated in Figure 2.6, and are significant, especially for low mode edge waves and high frequencies.

Another way to examine the impacts of tide is to compare numerically calculated $k_y$ to the analytical case. For a plane beach (slope angle $\beta$), the edge wave (mode $n$) dispersion relation is $k_y = \frac{\omega^2}{g\tan\beta(2n+1)}$, and the numerically computed $k_y$ are used to

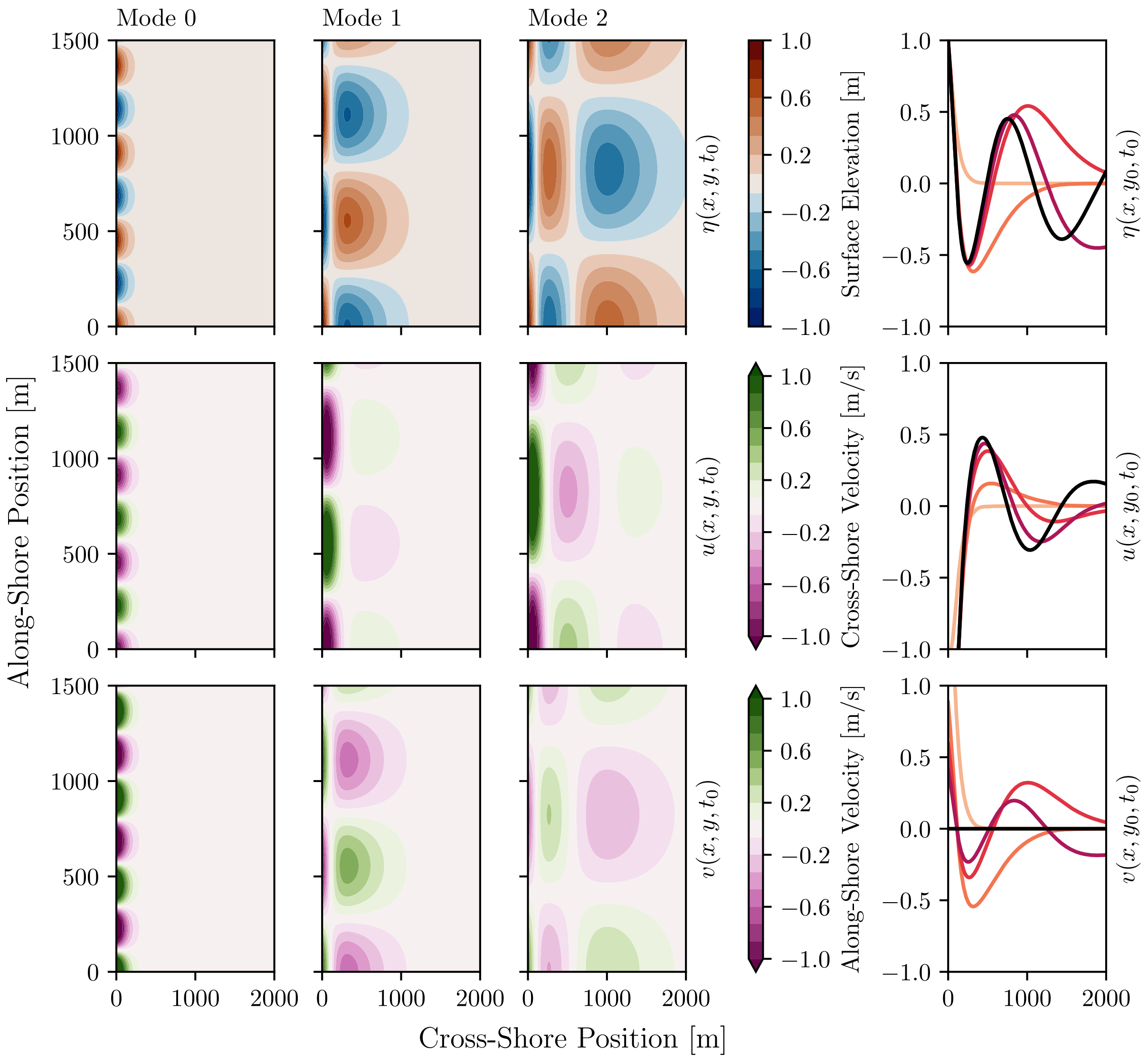

**Figure 2.4.** Example 0.01 Hz low mode edge waves for highest tide quintile, for surface elevation (p, top row), cross-shore velocity (u, middle row) and along-shore velocity (v, bottom row), with amplitude=1 m at the shoreline. 3 different modes are shown (0, 1, 2, corresponding to first, second, and third columns). Cross shore amplitude structures are shown in the rightmost column, for modes (0,1,2,3, lightest to darkest) and a shore-normal wave (black). p,u,v are all maximum at the shoreline but P-U are out-of-spatial-phase after the first 0-crossing. Note also a slight shoreward procession in zero crossings when mode number increases.

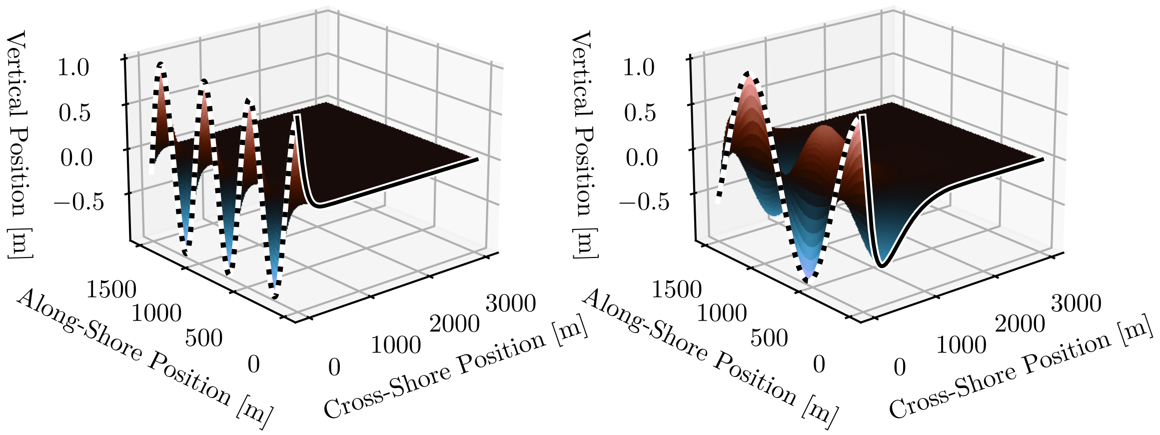

a. $\eta(x, y, t_0)$ 0.01 Hz, Mode 0

b. $\eta(x, y, t_0)$ 0.01 Hz, Mode 1

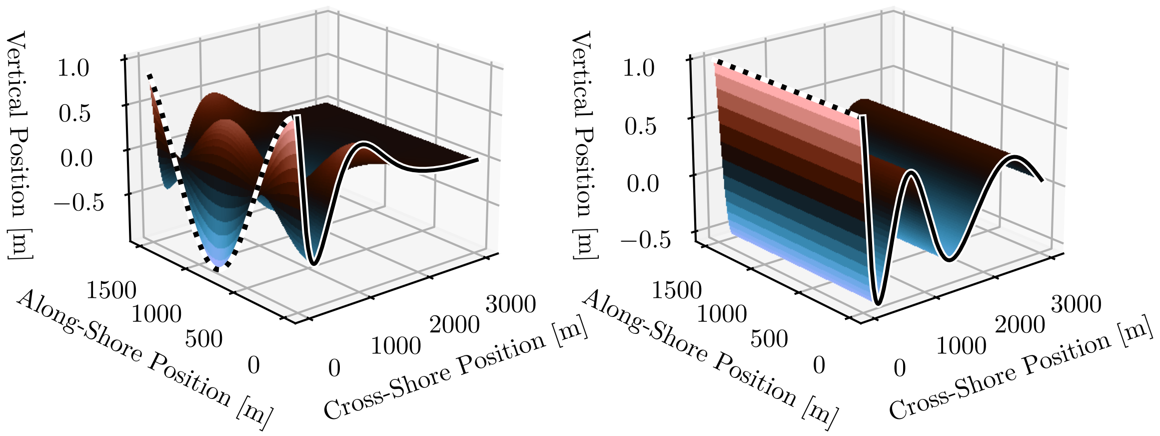

c. $\eta(x, y, t_0)$ 0.01 Hz, Mode 2

d. $\eta(x, y, t_0)$ 0.01 Hz, Shore-Normal

**Figure 2.5.** Example surface elevation of 0.01 Hz low mode edge waves (a,b,c) and shore-normal wave (d), with amplitude=1 m at the shoreline.

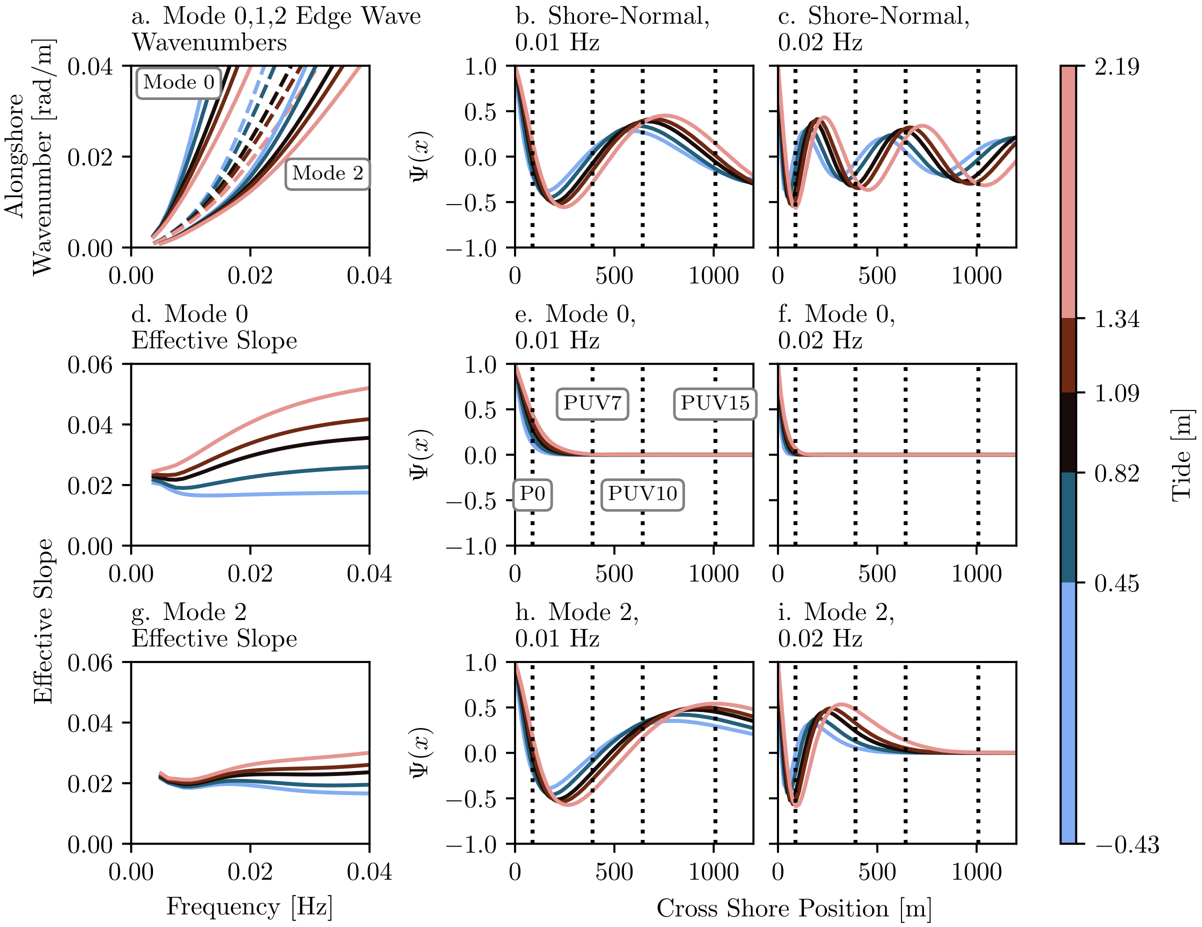

**Figure 2.6.** Linear shallow water modes, versus frequency and tide. (a): Alongshore wavenumbers $k_y$ versus frequency for modes 0 and 2 infragravity edge waves, in 5 tidal quintiles (see color bar). Mode 1 sits between, dashed (not labeled). (d,g): Effective slope of edge waves mode 0 (d) and 2 (g) as function of frequency, derived by assuming a plane beach and back-calculating slope from derived $k_y$, as described by Holman and Bowen (1979). (b,c,e,f,h,i): Cross shore structures of a shore-normal wave (b,c) and mode 0 (e,f) and 2 (h,i) edge waves, under changing tides for 0.01 and 0.02 Hz. Instrument positions are plotted as vertical lines. Note that for same shoreline amplitude ($\Psi(0) = 1$), lower tides (light blue) have smaller offshore amplitudes.

back-calculate the "effective slope" $\beta_{\text{effective}}$ (as done in Holman and Bowen (1979)) (Figure 2.6d,g), further demonstrating the tidal impacts on low modes and high frequencies.

### 2.3.2 Bayesian MAP for Shallow Water

Past methods for characterizing infragravity edge waves (MLE and IMLE, Huntley et al. (1981), Oltman-Shay and Guza (1987)), utilized 1 dimensional arrays with one data type (typically along-shore velocity). Sheremet et al. (2001) developed and tested an inverse method using cross spectra from 2 dimensional (cross-shore and along-shore) sensor array of pressure and currents simultaneously to estimate shallow water mode amplitudes, using nonlinear least squares. Here we build on previous results by utilizing modern Bayesian statistics and a large (1.5 by 1 km) array and record length (2 months), and focus specifically on edge waves.

Starting with a sum of $N$ arbitrary modes, the velocity potential (for a single frequency) is

$$\phi(x,y,t,\omega) = \sum_{n=1}^{N} \left(-i\frac{g}{\omega}\right)\ a_n(\omega)\Psi_n(x,\omega)\ e^{-i(\omega t\ +k_{y,n}(\omega)y+\theta_n(\omega))} \tag{2.6}$$

Note that all equations in this section are for a single frequency, and are frequency dependent (e.g., a Mode 0 edge wave changes $\Psi(x,\omega)$ and $k_y(\omega)$ according to frequency), but the $\omega$ will be dropped for brevity. We assume modes are uncorrelated ($< a_n a_m >= 0$, $< \theta_n\theta_m >= 0$).

We compute the tie Fourier transform of Equation 2.6, and take the expected value of the covariance of the Fourier coefficients between instruments to compute the expected cross spectrum ($G$) at frequency ($\omega$) between two sensors ($\alpha$ and $\beta$):

$$G_{\alpha\beta} = \sum_{n=1}^{N} a_n^2 C_{\alpha,n} C_{\beta,n}^* \tag{2.7}$$

Where $C_{\alpha,n}$ is replaced with $P_n(x,y)$, $U_n(x,y)$, or $V_n(x,y)$, ($\alpha$ or $\beta$ referring to both sensor type and location), defined as

$$\begin{aligned} P_n(x,y) &= \Psi_n(x)e^{ik_n y} && (2.8) \\ U_n(x,y) &= i\frac{\sqrt{gh(x)}}{\omega}\Psi'_n(x)e^{ik_n y} && (2.9) \\ V_n(x,y) &= k_n\frac{\sqrt{gh(x)}}{\omega}\Psi_n(x)e^{ik_n y} && (2.10) \end{aligned}$$

Note that in Equations 2.9 and 2.10, U and V assume surface elevation units using the shallow water dispersion relation, which is not valid at the shoreline and inner surfzone where beach slope is important, but valid for the present IG currents in 7-15m depth. Note also that the real part (co-spectrum) corresponds to the sum of up-coast and down-coast motions, and the imaginary part (quad-spectrum) corresponds to their difference.

Using the "forward problem" (have amplitudes, compute cross spectra) in reverse, the observed cross spectra can be inverted for amplitudes using matrix calculus. Equations for the cross spectrum in matrix form are

$$\mathbf{Hm} + \mathbf{r} = \mathbf{d} \tag{2.11}$$

where $\mathbf{m}$, the model parameter vector (size $N \times 1$ for $N$ modes), is

$$m_n = a_n^2 \tag{2.12}$$

The observation/data vector $\mathbf{d}$ is

$$d_m = \hat{G}_{\alpha\beta} \tag{2.13}$$

and is size $D \times 1$, where $D$ is the number of sensor-sensor cross spectral $\alpha\beta$ combinations, including self-self combinations. Real and imaginary parts of the cross-spectrum are used as independent data points in the inversion, so the matrices are all real. Each sensor pair is only counted once. Therefore, for $S$ sensors, there are $D = S^2$ members of the data vector. The forward problem matrix $\mathbf{H}$ (size $D \times N$) is defined as

$$H_{m,n} = C_{\alpha,n} C^*_{\beta,n} \tag{2.14}$$

and $\mathbf{r}$ (same size as $\mathbf{d}$) represents random uncertainty.

To invert for mode amplitudes, we use a Bayesian Maximum A Posteriori estimate (MAP) (Wunsch, 2006; Kachelein et al., 2022; Van Trees, 2001), adapted for shallow water modes as briefly described here. The goal is a least squares fit for shallow water mode amplitudes, which uses a prior constraint on mode amplitude to make a fit that is conservative and stable. Bayes' theorem states

$$P(\mathbf{m}|\mathbf{d}) = \frac{P(\mathbf{m})P(\mathbf{d}|\mathbf{m})}{P(\mathbf{d})} \tag{2.15}$$

where $P(\mathbf{m}|\mathbf{d})$ is the posterior probability distribution function to be maximized, $P(\mathbf{m})$ the prior on $\mathbf{m}$, and $P(\mathbf{d}|\mathbf{m})$ the likelihood function. $P(\mathbf{d})$ is a normalization constant and is ignored in the standard development. Maximum likelihood estimates (MLE, Davis and Regier (1977); Sheremet et al. (2001) and many others), maximize $P(\mathbf{d}|\mathbf{m})$ (equivalent to a least squares minimization) whereas Maximum A Posteriori (MAP) estimate maximizes $P(\mathbf{m}|\mathbf{d})$. Our likelihood function is a standard chi square:

$$P(\mathbf{d}|\mathbf{m}) \propto \exp\big( -(\mathbf{Hm} - \mathbf{d})\mathbf{R}^{-1}(\mathbf{Hm} - \mathbf{d})^T\big) \tag{2.16}$$

where the matrix $R$ is the covariance of the random uncertainty.

Assuming Gaussian probability distributions using the variance of the cross spectra

(Bendat and Piersol, 2011), the statistical uncertainty in a cross-spectral estimate is

$$R_{\alpha\beta} = G_{\alpha\alpha} G_{\beta\beta} \frac{1}{N_D} \tag{2.17}$$

where $G$ is defined in equation 15, and $N_D$ is the number of segments (typically 6, when using 90 minute records and 800 second non-overlapping segments). We assume zero cross-covariance between the uncertainty of observations of the cross spectra, making R diagonal. The model representational error, arising from expected motions not included in the model, is unknown and not included.

For the prior on $\mathbf{m}$, we assume a flat (in mode or wavenumber space) Gaussian (in amplitude space) prior, centered on 0, with variance $\sigma^2$ ($\sigma$ has units $m^2$), resulting in a model covariance matrix $\mathbf{P} = \mathbf{I}\sigma^2$ where I is the identity matrix and the prior probability distribution is

$$P(\mathbf{m}) \propto \exp\left(-\mathbf{m}^T \mathbf{P}^{-1} \mathbf{m}\right) \tag{2.18}$$

Without a prior, model energy is unconstrained and may try to fit noise.

The resulting posterior probability distribution function (in logarithm) is

$$\ln\left(P(\mathbf{m}|\mathbf{d})\right) = \; -\mathbf{m}^T \mathbf{P}^{-1} \mathbf{m} - (\mathbf{Hm} - \mathbf{d})\mathbf{R}^{-1}(\mathbf{Hm} - \mathbf{d})^T \; + \; \text{constant} \tag{2.19}$$

Minimizing equation 21 yields $\widehat{\mathbf{m}}$ , the best estimate of $\mathbf{m}$,

$$\widehat{\mathbf{m}} = \left(\mathbf{H}^T \mathbf{R}^{-1} \mathbf{H} + \mathbf{P}^{-1}\right)^{-1} \mathbf{H}^T \mathbf{R}^{-1} \mathbf{d} \tag{2.20}$$

The MAP inversion only increases model energy to decrease the misfit.

The model prior size $\sigma$ is a free parameter that must be chosen. The normalized misfit (equivalent to chi square of cross spectra)

$$J = \left(\mathbf{H}\widehat{\mathbf{m}} - \mathbf{d}\right) \mathbf{R}^{-1} \left(\mathbf{H}\widehat{\mathbf{m}} - \mathbf{d}\right)^T = \frac{\left(G_{\alpha\beta,\ modeled} - G_{\alpha\beta,\ observed}\right)^2}{G_{\alpha\alpha,\ observed} G_{\beta\beta,\ observed}} n_D \tag{2.21}$$

is used to evaluate fit from $\sigma$ values, and the elbow method (Satopaa et al., 2011) is used to select $\sigma$.

A least squares inversion can output negative variances in $\widehat{\mathbf{m}}$ (because this is not a non-negative least squares method), particularly when $\sigma$ is too large. Negative variances are unphysical and excluded before computing $J$, which cross-validates $\sigma$.

The resulting shallow water mode amplitudes are conservative, as small as possible while fitting as much of the data as possible. A typical example record and cross-spectra fit (Figure 2.7) illustrate the statistical chatter and significant misfit.

Model skill is estimated with the ratio of normalized misfit (Equation 2.21) to the case with no model estimate, i.e. $m_n = 0$:

$$s = 1 - J \ / \ J_0 \tag{2.22}$$

This is the fraction of the weighted cross spectral variance that the model explains. Average skill as a function of tide and frequency is plotted in Figure 2.8. Across all tides and frequencies, the average is 0.28. Owing to the unknown contribution of motions other than linear shallow water modes to the cross spectra, combined with biases from the spatial arrangement of the sensor array, the expected total skill or contribution of shallow water modes to the cross-spectra is not known.

The number and types of shallow water modes to include in $\mathbf{m}$ and $\mathbf{H}$ is an important method decision. Edge wave modes 0 through 9 are calculated. The shore-normal $\Psi(x)$ (alongshore wavenumber $k_y = 0$) is used to approximate leaky modes and higher mode edge waves (with small $k_y$). To account for small errors in wavenumber (arising from

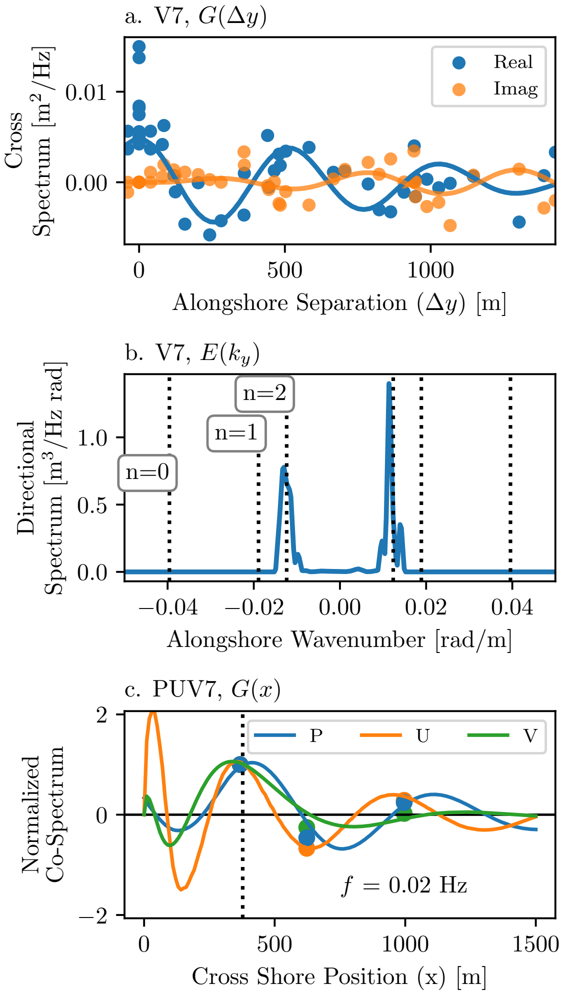

**Figure 2.7.** Typical MAP-modeled cross-spectrum for a 90 minute record (20 October 2021, 15:00 UTC) at frequency 0.02 Hz. MAP uses all cross-spectra, and results are shown here for (a) V7 array observed alongshore velocity cross spectra (data points) and MAP fit (solid line) versus sensor separation. Real (blue) and Imaginary (orange) parts of the cross-spectra are shown. (b) wavenumber spectrum of MAP fit at V7. Approximately equal amounts of up and downcoast propagating mode 2 edge waves yields relatively small imaginary cross-spectra. (c) Cross-spectrum along a transect (MOP582), with observed normalized co-spectrum (data points) between PUV7 and other PUV on MOP 582 ( P-P, U-U and V-V are shown), compared to MAP-fit normalized co-spectrum (solid lines). Normalization sets autospectra at PUV7 location (dotted line) to 1 (at that location, P, U, and V are overlapping).

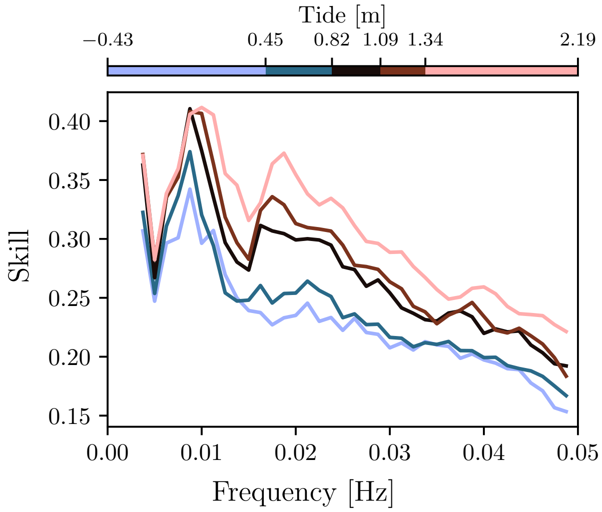

**Figure 2.8.** MAP skill (Equation 2.22) versus frequency and tide quintile (color bar). MAP skill is highest at high tide at IG frequencies between 0.01-0.02Hz.

random error, alongshore variations in bathymetry and other unaccounted factors such as setup, eddies, nonlinearity, etc), modes with “off resonant” $k_y$ are included in the mode fit, similar to Dushaw et al. (2011), with $k_y$ up to one array fundamental wavenumber from the numerically computed $k_y$. These off-resonant $k_y$ modes use the $\Psi(x)$ of the nearest standing mode in wavenumber space.

The 1.5 km PUV7 array has a fundamental wavenumber of $k_{y,f} = 2\pi/1500$ m $\approx 0.004$ rad/m. We use a spacing between modes of $0.2 \times k_{y,f}$ for a relatively fine resolution, enabled by the many cross-spectra available (>1000 for each frequency) to distinguish closely spaced modes (e.g. Figure 2.7b).

## 2.4 Results

### Edge Wave Amplitudes

After inverting observed cross spectra for mode amplitudes, it is straightforward to extrapolate edge wave sizes to the shoreline (and other locations). MAP estimates of low mode (0,1,2) infragravity edge wave significant wave height (from 7m depth to the shoreline) are computed as a time series in 3 depths (Figure 2.9), and as tidally averaged frequency spectra (Figure 2.10). Infragravity edge wave swash height for the duration of the experiment is between 5 and 50 cm, and is highly correlated with tide and $\sqrt{H_0 L_0}$ (as are other infragravity waves). Compared to all standing modes estimated by MAP, low mode edge waves are only a large fraction or majority at low frequencies. MAP qualitatively reproduces the observed node/antinode frequency spectrum structure of standing infragravity modes (Figure 2.10).

Maximum Likelihood Estimator (MLE) and MAP are compared to MAP in Figure 2.11 (see Section 2.4.2 for details). Associated runup frequency/wavenumber spectra from shallow water standing modes estimated by MAP are also plotted in Figure 2.11.

The estimated fraction of total infragravity variance in edge wave modes is considered in Figure 2.12. In 2 months of observations in 7m depth, edge waves are estimated to contain 25-35% of the surface elevation infragravity variance and 35-50% of the along-shore velocity variance. Though infragravity wave heights are larger at high tide, the variance fraction of edge waves at the runup line is higher at low tide, owing to a second order effect (see discussion section) where edge waves decay slightly less at low tide than SWASH 1D modeled infragravity runup.

Using SWASH 1D as a point of comparison (see section 2.4.3 for details), we attribute 10-25% of the runup variance to edge waves. As seen before, edge waves are most impactful on alongshore velocities. MAP is conservative, and only quantifies observable modes, excluding modes decayed shoreward of the sensor array or with nodes aligning with sensor positions. Therefore, MAP estimates of edge wave size may underpredict.

### 2.4.1 Reflectance

Reflection coefficient $R^2$, the ratio of seaward to shoreward wave energy in the infragravity band, is estimated assuming linear waves and cross-shore propagation (Sheremet et al., 2002). Observed (or modeled) timeseries of co-located sea surface elevation $\eta$ and cross-shore velocity $u$ yields the shoreward $\eta_+$ and seaward $\eta_-$ propagating sea surface

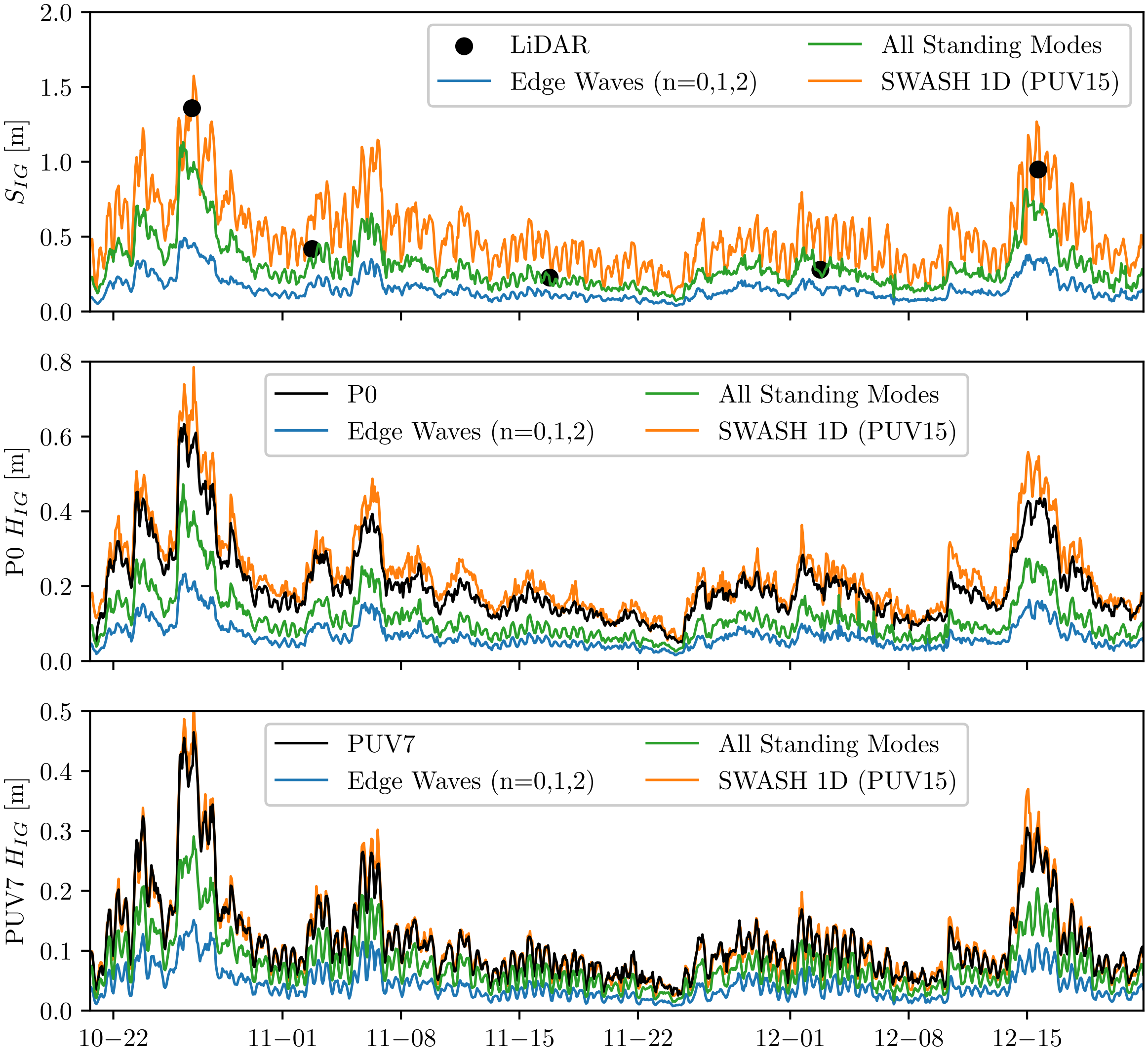

**Figure 2.9.** Timeseries of infragravity height observed (black, averaged between sensors), estimated with SWASH 1D (orange, initialized in 15m, 1 km offshore) and with the MAP inverse method (a) runup SIG, (b): P0 HIG and (c) PUV7 HIG. MAP estimates are of low-mode edge waves (blue) and all standing modes (green).

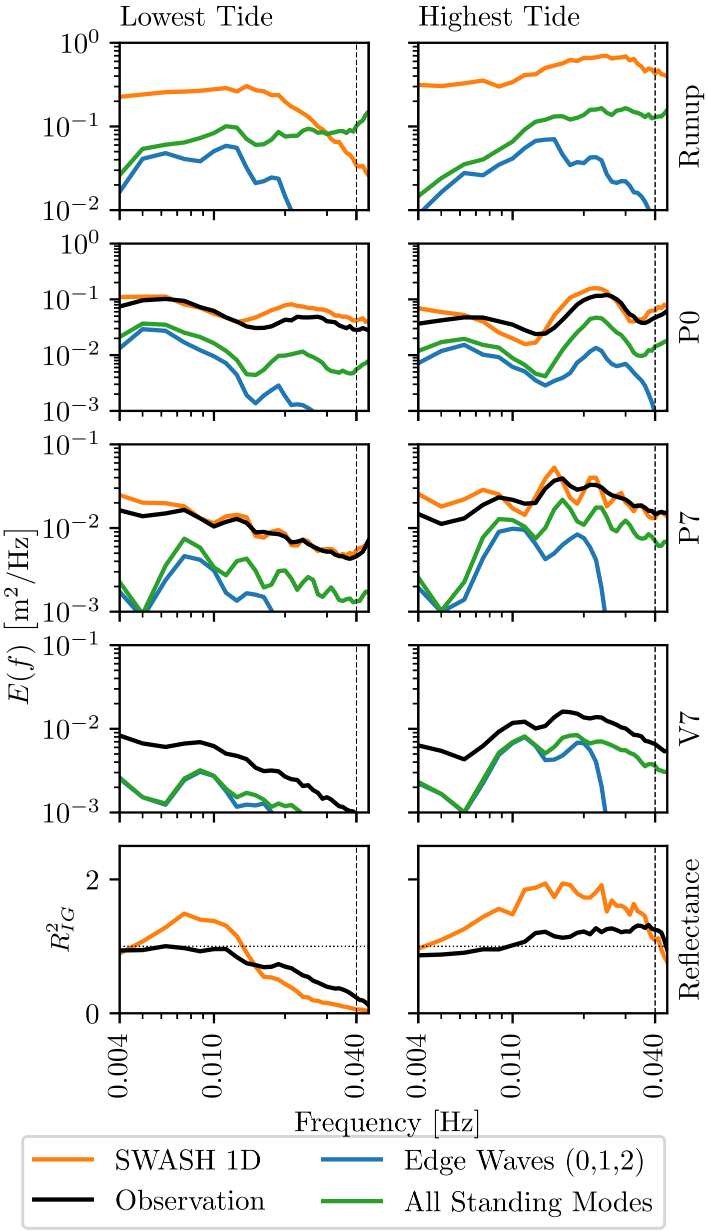

**Figure 2.10.** Low tide (left column) and high tide (right column) quintile (300 hour) average infragravity frequency spectra for (a,b) runup (1st row), (c,d) P0, (e,f) P7 and (g,h) V7 arrays and (i,j) infragravity reflection coefficient. Figure labels are on the right. Observations (black), SWASH (orange, initialized in 15m, 1 km offshore) and MAP estimates of low-mode edge waves (blue) and all standing modes (green). Lowest and highest tide depth quintiles ranges are [-0.43m, +0.45m] (7.2 m average ) and [+1.34m, +2.19m] (8.7 m average ) respectively. SWASH 1D compares well with observations at (c,d) P0 and (e,f) P(7).

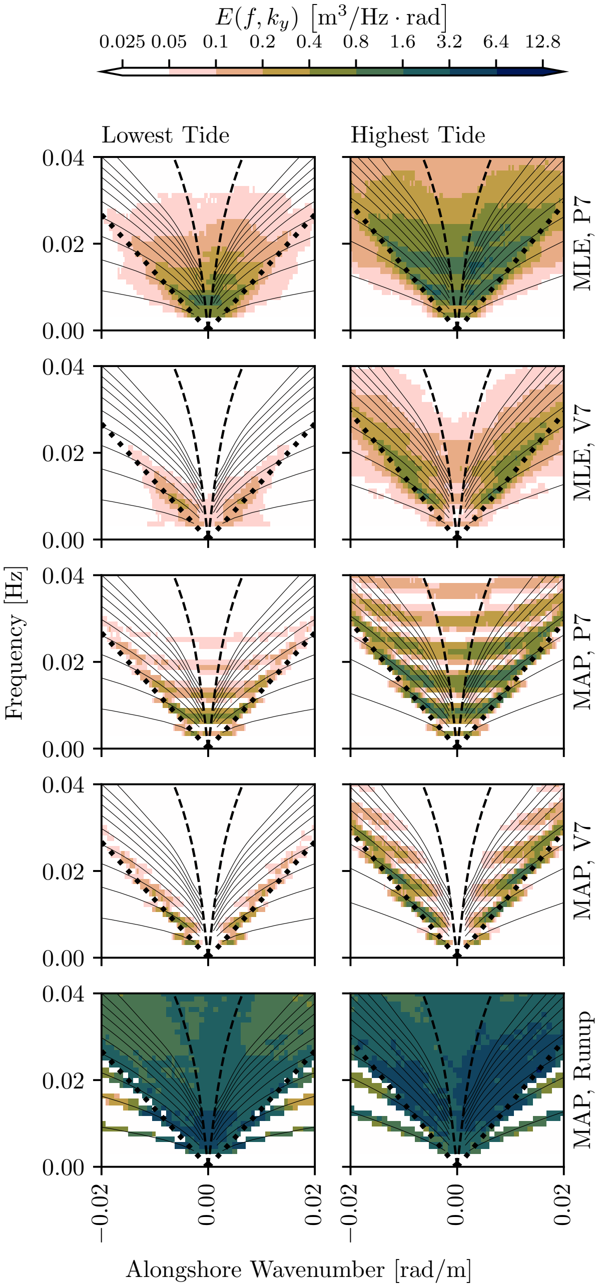

**Figure 2.11.** $E(f, k_y)$ from MLE (rows 1-2) or MAP (rows 3-5), for lowest/highest (left/right) tide quintiles (300 hour medians). MLE uses P7 and V7 arrays independently, with no prior information, and allows noise, whereas MAP fits one linear mode spectrum to all data, which is extrapolated to the runup line (row 5), and rejects noise. V is converted to equivalent surface elevation using linear WKB theory. Lowest/highest depth quintiles ranges are [-0.43m, +0.45m] (7.2 m avg) / [+1.34m, +2.19m] (8.7 m avg). Mode 0-9 edge wave dispersion curves are plotted (solid lines). Free wave dispersion ($\omega^2 = gk \tanh(kh)$) for the maximum alongshore wavenumber at that depth, are plotted for the PUV7 array (dotted line, demarcating waves free up to the PUV7 array depth) and for 500m depth (dashed line, roughly demarcating shelf-trapped waves).

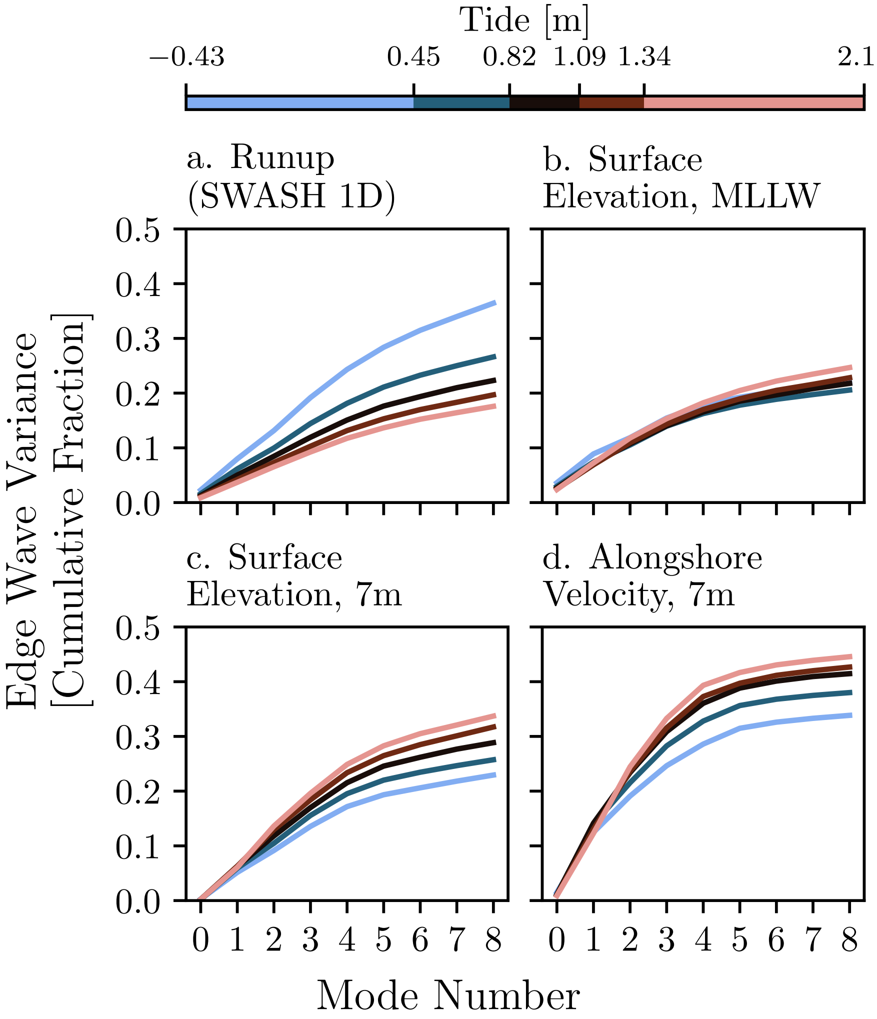

**Figure 2.12.** Cumulative fractional variance of infragravity edge waves versus mode number, colored by tide quintile (see legend). (a) runup, (b) P0 array near the mean lower low water line, (c) P from PUV7 array, and (d) V from PUV7 array. The MAP infragravity edge wave variance is normalized by the observed total IG, except runup where the total SWASH 1D estimated infragravity runup is used.

elevation.

$$\eta_{\pm} = \frac{1}{2}\left(\eta \pm u_{z=0}\frac{\tanh kh}{\omega}\right) \tag{2.23}$$

The bathymetric profile is concave, with high shoreline slope at high tide, and convex with low shoreline slope, at low tide (fig 1c,d). The resulting reflection coefficient averaged over infragravity frequencies is plotted in Figure 2.2 for PUV7, and tidally averaged in Figure 2.10. Reflection coefficient depends on sensor position relative to surfzone (as shown in Sheremet et al. (2002)), and is strongly affected by tides. As will be discussed later, reflectance may be dynamically important for edge waves.

### 2.4.2 MAP vs MLE

MAP and Maximum Likelihood Estimator (Davis and Regier, 1977) are conceptually similar. MLE inverts cross spectra (of a single type independently, i.e. PP, UU, VV) from a linear array into estimated power at any alongshore wavenumber, including noise, at some depth, without making any assumptions about wave physics. Our implementation of MAP, by comparison, inverts all cross spectra (from a 2D array) of all types into one set of self-consistent waves (at all depths), using shallow water modes with a conservatively set prior on mode size

The MLE frequency/wavenumber spectra for the P7 and V7 arrays are computed and plotted in Figure 2.11 and compared to MAP estimated frequency/wavenumber spectra for lowest and highest tidal quintile averages. In a frequency/wavenumber spectrum, edge waves are indicated by banding in frequency (due to standing modes) and energy centered around the edge wave dispersion curve, both of which are most visible in the high tide alongshore velocity signal for both estimators. The “U” shape visible in the high tide pressure signal (MAP or MLE) is caused by a slight procession of the node/antinode structure of shallow water mode $\Psi(x)$ under increasing mode number (visible in Figure 2.4, right column). At 7 m average depth, waves with larger alongshore wavenumbers than a cutoff wavenumber are trapped in shallower water. The cutoff alongshore wavenumber is that of a trapped (as in trapped in shallow water) free (as in freely propagating) wave traveling parallel to shore. MAP predicts no energy past the cutoff except the decayed (evanescent) tails of edge waves. Conversely, MLE predicts small but nonzero energy past the cutoff. Owing to its prior, MAP is also less energetic than MLE overall.

MLE and a related "high resolution" estimator IMLE (Pawka, 1983) were used by Huntley et al. (1981) and Oltman-Shay and Guza (1987) to estimate edge wave sizes. To evaluate the performance of our edge wave estimator, we will compare it to a version of the edge wave estimator implemented by Oltman-Shay and Guza (1987), who attributed energy from IMLE-estimated frequency/wavenumber spectra to edge waves if it was in a peak (defined by the half-power-width above a noise floor) which also contained an edge wave frequency/wavenumber dispersion curve. By instead attributing variance to edge waves if it is within one fundamental wavenumber of the dispersion curve, similar to our implementation of MAP, a similar estimate of edge wave variance, inspired by Oltman-Shay and Guza (1987), would be:

$$E_n(f) = \int_{k_{y,n}(f)-k_{y,f}}^{k_{y,n}(f)+k_{y,f}} E\left(f, k_y\right) dk_y \tag{2.24}$$

Where $n$ denotes edge wave mode, $k_{y,n}(f)$ the edge wave dispersion curve, and $k_{y,f}$ the fundamental wavenumber (in our case, $k_{y,f} = 2\pi/1500$ m $\approx 0.004$ rad/m). We follow the MLE method instead of IMLE because IMLE design goals ("high resolution" or narrow peaks) are not relevant to the study.

The first 3 infragravity edge wave total variances from MLE and our implementation of MAP are compared in Table 2.1, are linearly related, and have strong correlations (coefficient of determination close to 1). Considering all tide stages in 7m depth, the best agreement between MAP and MLE is when edge waves are not decayed (V7 Mode 1 and 2, coefficient of determination $R^2$=0.94, 0.97, regression slope $\approx 1$). The agreement is less

**Table 2.1.** Comparison of MLE (computed at PUV7 using Equation 2.24) and MAP estimated edge wave $H_{IG}$, in terms of linear regression slope and coefficient of determination ($R^2$) for edge wave modes 0,1 and 2, observed by the PUV7 array.

| | Mode 0 | | Mode 1 | | Mode 2 | |
|---|---|---|---|---|---|---|
| | Slope | $R^2$ | Slope | $R^2$ | Slope | $R^2$ |
| P7 | 0.33 | 0.85 | 0.73 | 0.97 | 0.73 | 0.94 |
| U7 | 0.43 | 0.86 | 0.59 | 0.94 | 0.64 | 0.93 |
| V7 | 0.55 | 0.88 | 0.98 | 0.98 | 0.94 | 0.97 |

for mode 0 ($R^2$=0.88) which is strongly decayed in 7m depth, where MAP estimates 1/3 the energy estimated by MLE. MAP amplitudes are lower than MLE (regression slope $\approx 1$, Table 2.1) because MAP rejects noise. This is a considerable constraint, relative to MLE, but means MAP esimates are all physically self-consistent waves.

### 2.4.3 SWASH 1D

Edge wave shoreline amplitude estimates need a point of comparison at the shoreline to understand their relative contribution to runup. The non-hydrostatic, phase-resolving numerical wave model SWASH (Zijlema et al., 2011) in 1D is known to be a high skill model for estimating infragravity wave runup (Fiedler et al., 2018; Henderson et al., 2022), and will be used for comparisons. Also, methods simulating waves across a 1D transect are common in nearshore physical oceanography, but by definition exclude edge waves, so 1D model performance is a quantity of interest for assessing the importance of edge waves.

SWASH is initialized with the ingoing wave timeseries observed at PUV15 (1 km offshore) on a 1D cross-shore transect (identified as MOP 582 in Figure 2.1). SWASH is equivalent to a layer-averaged RANS model, which resolves individual waves and nonlinear wave-wave interactions. Recommended physics and numerics for two layers are used, similar to Smit et al. (2013). Default friction is used (reasonable for a sandy beach), with a weakly reflective wave absorber. The 2D SWASH engine is used for variable grid size, but the domain is essentially a narrow wave flume, and is therefore referred to as "1D". For more details, see Chapter 1. SWASH modeled infragravity wave heights are then plotted in Figure 2.9 and tidally averaged spectra in Figure 2.10 for comparison with edge waves.

We validate SWASH against P0 and P7 observations of significant infragravity wave height, as well as infragravity reflection coefficient in 7m, in Figure 2.13. Overall SWASH 1D performance for predicting significant infragravity wave height is good, despite the expectation that a 1D model excludes edge waves. SWASH does overpredict infragravity variance by ≈5% at PUV7 and ≈30% at P0, on average, and overpredicts infragravity reflection coefficient by 50%. SWASH 1D overprediction of infragravity waves may be related to the 1D assumption discussed by Lange et al. (2023b). SWASH 1D, being run on a cross shore transect, cannot support trapped waves.

SWASH 1D is computed for the 1500 hours of the study and is used as a comparison point representing 1D dynamics (as in only cross-shore motions), including wave transformation and infragravity generation and dissipation. The cross-shore structure of standing (shore-normal) waves is reproduced (see SWASH-modeled nodes and antinodes in Figure 2.10). The cross-shore evolution of significant infragravity wave height is compared to that from edge waves estimated with MAP in Figure 2.14. In all cases, tidal variations are important, so tidal quintile averages are given.

In Figure 2.14, both SWASH 1D modeled infragravity wave height and edge wave height increase shoreward, indicating shoaling. Edge waves shoal linearly (following Green's law), whereas SWASH shoals nonlinearly, interacting with breaking sea swell waves. Both are significantly affected by tides. While edge waves are more relatively important offshore at high tide, the reverse is true for comparisons to SWASH 1D modeled runup (low tide edge wave runup is more relatively important than high tide edge wave runup). However, in all cases, edge wave height (runup or offshore) is maximized at high tide.

### 2.4.4 LiDAR Runup

LiDAR observations of runup are relatively sparse (less than 1% of coverage) and are not usable for overall runup validation, but are able to validate MAP and SWASH

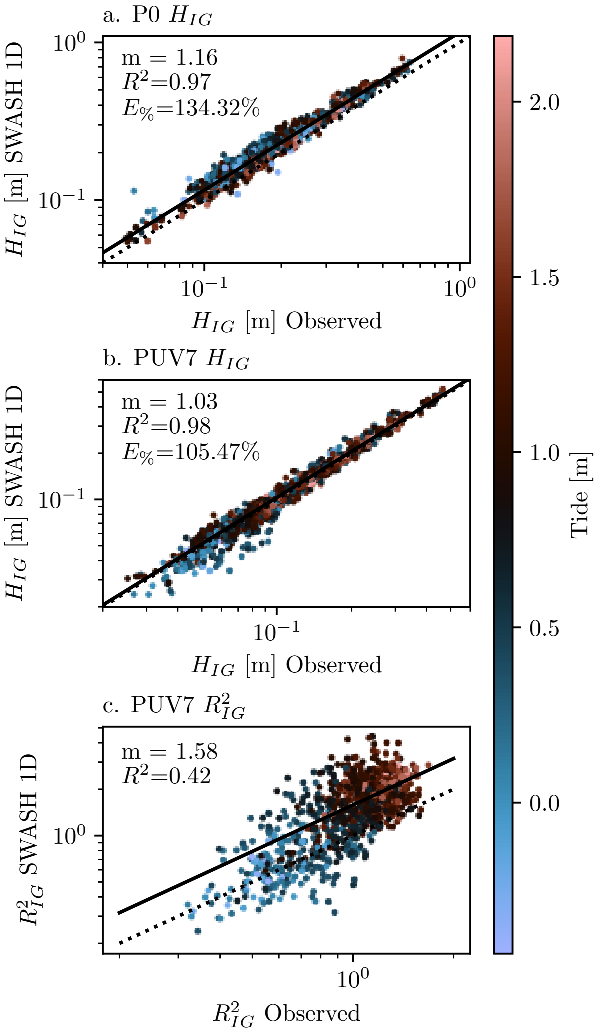

**Figure 2.13.** Performance of SWASH 1D for predicting infragravity wave height at P0 and PUV7, and infragravity reflection coefficient at PUV7. 2 months (1500 hours) of SWASH 1D (initialized at PUV15) HIG estimates versus observed $H_{IG}$ at (a) P0 and (b) PUV7, and (c) resulting infragravity reflection coefficient $R^2_{IG}$ at PUV7. Estimates above the 1:1 (dotted) line are SWASH 1D overestimates. Linear fit (zero intercept) (solid line), slope, and coefficient of determination ($R^2$) are included in each subplot. For wave height comparisons, the resulting variance ratio is given as a percentage, showing SWASH 1D overprediction of variance at P0 by ≈30% on average at P0, with ≈50% overprediction of reflection coefficient.

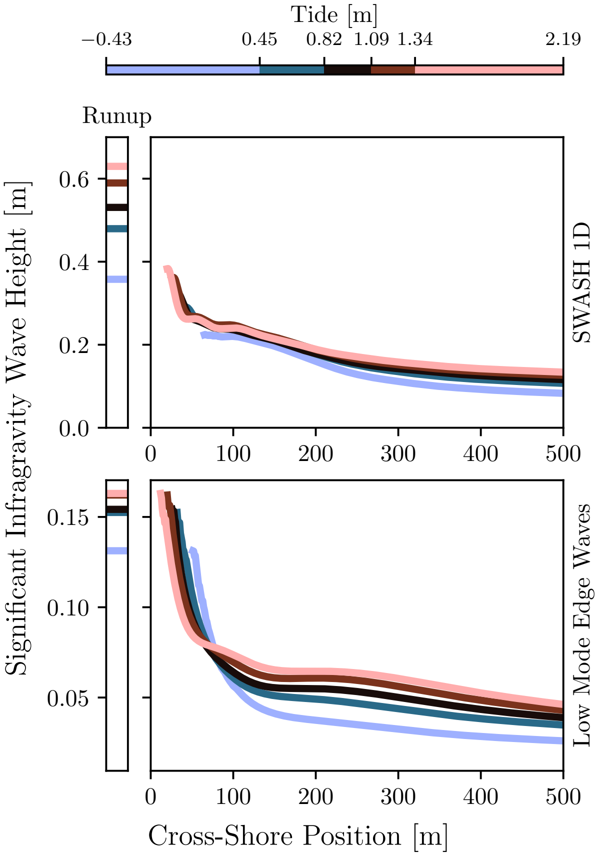

**Figure 2.14.** Tidally averaged significant infragravity wave height between SWASH 1D (top row) and MAP estimates of low mode (0,1,2) edge waves (bottom row). Runup is given in the left panels. Edge waves decay exponentially offshore, as expected. Edge wave runup assumes the shoreline (still water line) amplitude and runup are equal. When SWASH modeled $H_{IG}$ begins to decrease due to intermittent exposure of the sand bed in the swash zone, $H_{IG}$ values are cutoff.

performance for a few cases. Example LiDAR observations of runup time series and spectra, compared to MAP (low mode edge waves) and SWASH, are given in Figure 2.15. Unlike chapter 1, SWASH 1D does not attain phase agreement with LiDAR observations, possibly owing to the boundary being initialized 1 km away from shore, rather than 6m. LiDAR runup is instead used as a cross-validation for MAP, showing phase between offshore and runup, similar to Guza and Thornton (1985). Standing modes are either exactly in phase (phase is 0) or out of phase (phase is $\pm\pi$). Phase jumps are associated with nodes in the autospectrum. The overall agreement between SWASH and observations suggests SWASH 1D reproduces the observed standing wave structure, but only as a shore-normal fully reflected leaky wave, on top of a background of progressive waves.

## 2.5 Discussion & Conclusions

### Edge Waves

The amplitudes of infragravity waves (total wave size, standing waves, and low mode edge waves) depend on $\sqrt{H_0 L_0}$, infragravity frequency, and tide level (see Figure 2.16). Edge waves are largest with large incident wave energy, at low IG frequencies and high tide (associated with steeper slope on this concave bathymetry). Edge waves arise from multiple reflections off the shoreline and deep water (Schäffer and Jonsson, 1992). High reflectance (which also changes IG generation/dissipation) may indicate favorable conditions for multiple reflections, explaining the tidal dependence (Okihiro and Guza, 1995; Thomson et al., 2006).

Edge wave runup is less strongly decayed by low tide, compared to SWASH 1D modeled runup. A possible explanation is that shallow water mode $\Psi(x)$ change in tide (see Figure 2.6), which leads to smaller offshore antinodes. Given a fixed offshore wave height, therefore, a shallow water mode at low tide has a larger expected shoreline amplitude.

Dependence of edge wave fraction on other variables (e.g. directional spread) is

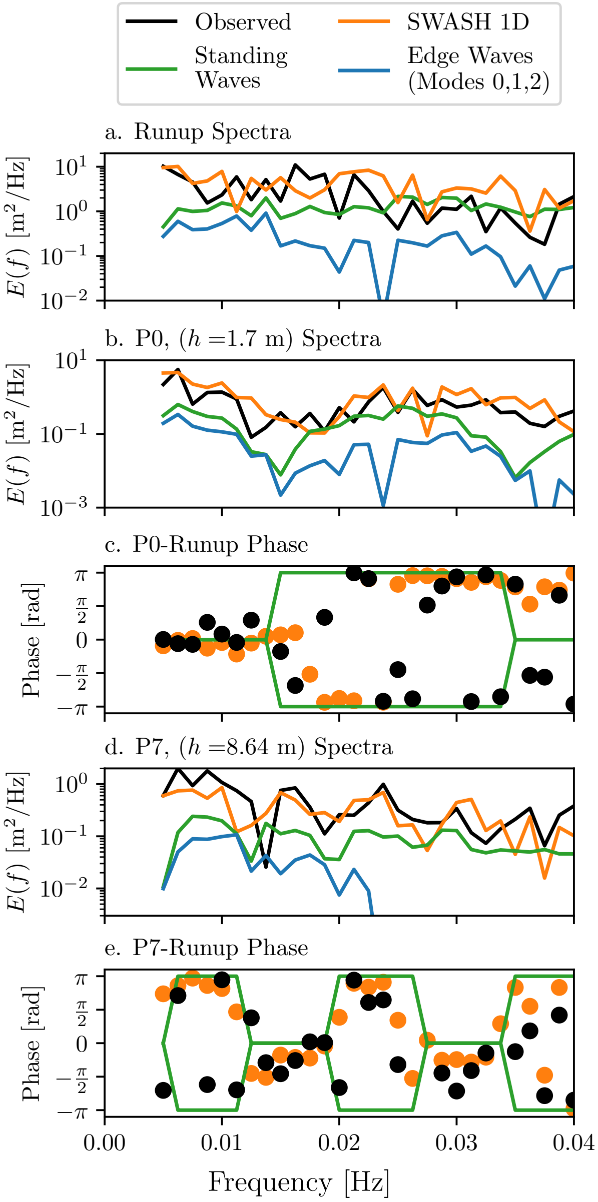

**Figure 2.15.** Example spectra compared between observations and MAP/SWASH along cross-shore transect MOP 582. Autospectra from observations (black), SWASH 1D (orange), and MAP-estimated edge waves (blue) and total standing waves (green, includes all leaky and trapped modes) are compared at the runup line at the shoreward end of MOP 582 (a), P0 sensor on MOP 582 (b) and P7 sensor on MOP 582 (d). Phase between P0/P7 and runup is given in subplots c,e. MAP-modeled phase is always either 0 or $\pm\pi$, for standing modes in or out of phase, while real observations and SWASH 1D have progressive modes (phase between 0 and $\pm\pi$). Phase flops between 0 and $\pm\pi$ after each spectral node node. Low mode edge waves are relatively decayed at higher frequencies. Spectra use only one array member (MOP 582 P0/P7) with 10 x 800 second segments (20 degrees of freedom).

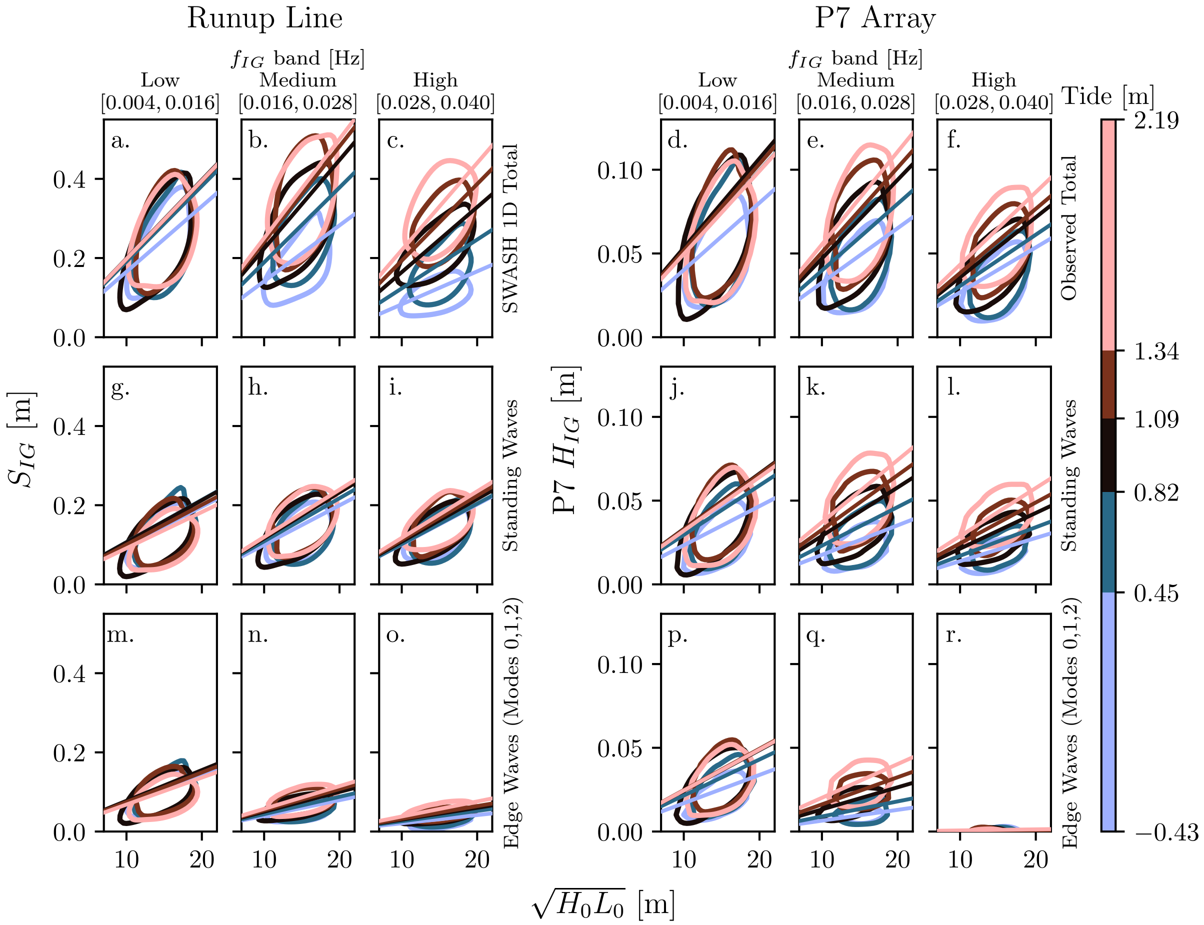

**Figure 2.16.** Infragravity wave heights compared between SWASH, edge waves, standing waves, and observations, at P7 array and runup, in tide and frequency bins. All observations are parsed by tide level (color bar) and incident wave conditions in 3 infragravity bands (low, medium, and high frequencies in the left, middle, and right columns). Shown are 50% population contours of significant wave heights in Runup (left) and P7 (right) are compared. SWASH 1D total runup (as proxy for an observation) and observed total compared to low mode edge waves (0,1,2) and all standing modes. A least squares linear slope is plotted, i.e. $H_{IG} = m\sqrt{H_0 L_0}$ in each tidal bin. Population contours are the highest probability region (estimated with Gaussian KDEs) that contain 50% of the observations in each tidal quintile. Note that low modes and high frequencies are most strongly decayed offshore, though all IG waves in Southern CA are smaller at low tide.

unclear in this data set, owing partially to the correlation of wave height and directional spread in Southern California. Further study is needed to test if directional spread enhances edge waves (through forcing a wider variety of resonant edge wavenumbers (Gallagher, 1971)).

The method presented here shows low mode linear edge waves (in the infragravity band) are 5-25% of the pressure infragravity variance (15% average), and 5-50% (average 30%) of the along-shore velocity variance at 7m depth. Average variance is somewhat less than the days studied in Oltman-Shay and Guza (1987), and the comparison is not direct, as their along-shore current meter array was in 1.5m depth. MAP is also expected to predict less, owing to its conservative prior. We estimate edge waves (all modes) are 10-25% of the runup depending on conditions. Locally generated infragravity waves dominate runup energy spectra.

### 2.5.1 SWASH

Edge waves are a significant dynamic in the surfzone, yet are excluded by 1D numerical models. Despite this, SWASH 1D performs well at predicting bulk parameters (Fiedler et al., 2018), and even tends to overpredict shallow water and runup infragravity wave height (Figure 2.13). SWASH 1D also accurately predicts the cross-shore standing structure of fully reflected shore-normal infragravity waves (Figure 2.10).

1D assumptions are known to cause overprediction of bound infragravity waves in intermediate water depths (Sand (1982); Lange et al. (2023b) and many others), and similar dynamics may lead to overall infragravity overprediction. SWASH is often run in 1D using the bottom (Manning) friction as a free parameter to fit observations (e.g. Conde-Frias et al. (2017); Melito et al. (2022)). This methodology may invoke reasonable variations in bottom friction to explain errors caused by excluding 2D IG motions. Here instead we use default parameters and draw attention to model-data differences SWASH should not explain.

The exclusion of edge waves may push SWASH 1D towards underprediction, which may cancel errors somewhat, and explain good 1D model performance despite factors leading to overprediction. SWASH 1D overpredicts infragravity reflection coefficient in this study (Figure 2.13), likely due to the exclusion of trapped waves (forcing all generated infragravity waves to be leaky). The SWASH 1D weakly reflective wavemaker may also imperfectly absorb outgoing waves, a known problem in physical and numerical models (Blayo and Debreu, 2005), especially when waves are standing in the cross-shore, which could complicate measures of reflection coefficient (see Appendix B).

We investigated IG edge wave generation with SWASH 2D using bichromatic incident SS waves in the Appendix, but transients and wavemaker issues (incomplete absorption of seaward propagating 2D IG waves) proved challenging and the large spatial domains and long time series were computationally expensive. Preliminary results show IG edge waves are indeed generated by two sea swell waves incident on a plane beach (slope 0.02) with frequencies 0.09 hz (shore-normal) and 0.07 Hz with oblique wave direction chosen such that the difference wavenumber $\Delta k_y$ satisfies the mode 1 edge wave dispersion relation at the difference frequency $\Delta f = 0.02$ Hz (Gallagher, 1971), see supplemental figures. Further model refinements are needed for quantitative study of IG edge waves.

### 2.5.2 MAP

MAP combines all sensors and variables (PUV) for one conservative, physics-based, self-consistent linear shallow water mode mix at each infragravity frequency. Node-antinode structure and the seaward decay of trapped modes are accounted for. However, only edge waves and a single shore-normal fully-reflected mode are modeled. A significant fraction of infragravity energy is expected to be progressive shoreward ($R^2 < 1$) or seaward ($R^2 > 1$). Depending on position in the surfzone, beach profile (and tide), and incident wave conditions, progressive IG energy varies cross-shore owing to nonlinear generation and dissipation. Progressive waves, setup, setdown, and along-shore variations in bathymetry are neglected. Small errors in cross-shore wave structure $\Psi(x)$ from unmodeled bathymetry detune the modeled and observed waves and introduce errors in node/antinode position (Figure 2.10). The many error sources and the conservative nature of the estimator suggest our method underestimates edge wave energy.

## Acknowledgements

This study was funded by the U.S. Army Corps of Engineers (W912HZ1920020) and the California Department of Parks and Recreation, Natural Resources Division Oceanography Program (C19E0026). Data was collected and processed by Center for Coastal Studies field team members Lucian Perry, Rob Grenzeback, Kent Smith, Shane Finnerty, Brian Woodward, Sierra Byrne, and Esther Nofodji, and academics Athina Lange, Hironori Matsumoto, Lauren Kim, Austin Barnes, Mika Siegelman, Mele Johnson, Zuzanna Swirad, Michele Okihiro, and Adam Young.

Scripps Institution of Oceanography sits on the unceded territory of the Kumeyaay Nation. Today, the Kumeyaay people continue to maintain their political sovereignty and cultural traditions as vital members of the San Diego/Tijuana Community. We acknowledge their tremendous contributions to our region and thank them for their stewardship.

Chapter 2, in full, is currently being prepared for submission for publication of the material. Cassandra S. Henderson and R.T. Guza, Bruce D. Cornuelle, Mark A. Merrifield and Julia W. Fiedler. The dissertation author was the primary investigator and author of this material.

# Conclusion

Chapter 1 demonstrates that 1D methods accurately predict phase-resolved runup and overtopping in field conditions, using a time series of incident waves in 7m depth as a boundary condition. Chapter 2 shows that infragravity edge waves, excluded from 1D methods, are typically 25% of the runup over 2 months at Torrey Pines State Beach. As 1D runup estimations become more sophisticated, the exclusion of edge waves and 2D bathymetry may become limiting factors.

On the open Torrey Pines coast edge waves are a significant fraction of the runup variance but do not form a linear core for nonlinear infragravity dynamics. Edge waves may be more important in pocket beaches (Özkan Haller et al., 2001) or with steep (strongly reflective) shorelines. The present work suggests interesting tidal effects on edge waves at the shoreline, but runup observations were limited by technical issues. Observations in a range of settings are needed but arrays of in-situ pressure and current meters are costly and labor intensive. Remote sensing (video and LiDAR) can provide long-term observations of runup over alongshore spans long enough to resolve IG edge waves but interpretation in terms of edge waves require companion observations of nearshore morphology.

Large scale phase-resolving 2D numerical wave models are becoming computationally feasible for infragravity edge waves but require extensive testing and validation. A simple model test (Appendix B) shows promising results from SWASH2D but also serious flaws.

# Appendix A

# Chapter 2 Array Details

## A.1 P0 Array

7 Paroscientific pressure sensors mounted on sand anchor pipes were deployed at approximately the MLLW tide line (-0.132 m NAVD88), called P0 sensors in this study. Locations were chosen based on past winter profiles. Paroscientific pressure sensors mounted on sand anchor pipes were used, however sand overburden was insufficient for the original planned array. The initial deployment was split into two dates (5 sensors on October 20-21 and 2 sensors on November 4). Sensors were deployed 40 cm under the sand.

Sand heights were monitored by hand (tape measure) daily. On November 15, the P0 sensor on MOP 585 was lowered by 60 cm on 11/15 after scouring exposed the sensor. On MOP 578, the sensor could not be lowered and was moved to 584 on December 3. A summary of positions and times is given in Table A.1. Array positions were chosen to attempt to use the P0 array as a lag array for MLE. However, the makeshift P0 positions were not ideal and were unable to resolve alongshore motions by themselves.

Tidal variations of 2.5 meters meant P0 sensors varied from 2+ meters depth to above the water line at the lowest tides. Spectra were computed over 90 minute records, and a P0 sensor is only used for that record if the sensor was fully submerged the whole time. Pressure, sampled at 2 Hz continuously, measured by buried sensors was converted to surface water levels using linear wave theory and dynamic sand burial depth, following Raubenheimer et al. (1998). Because shallow water pressure data is essential for the inverse method discussed later, we limit the data analysis to the deployment of the P0 array, i.e. from October 20 to December 21, 2021.

## A.2 PUV7 Array

During the RUBY2D experiment, 16 Nortek vectors ( co-located pressure (P) and current cross-shore U and along-shore V meters), called PUV, were deployed at 4 approximate depths (Table A.2), sampling continuously at 2 Hz. PUV data were processed by Athina Lange, see Lange et al. (2023a).

PUV10 at MOP 578 (on December 13) and PUV7 at MOP 579.2 (on October 26) were damaged and data collection ended. PUV were depth-corrected using linear theory. PUV used in MAP estimates of infragravity waves were required to pass the Z Test (1.2<Z<0.8 , Elgar et al. (2005)) , where $Z = \frac{S_{PP}}{(S_{UU}+S_{VV})}$, and S are observed spectra. Sensors failing the z- test for any 90 min-record are not used. PUV30 often had much larger IG (UV) velocities than consistent with linear theory and usually failed the Z test at IG frequencies. IG band motions other than gravity waves apparently dominate UV30.

**Table A.1.** P0 array locations, depths, and deployment durations.

| Sensor Type | MOP | Sensor NAVD88 [m] | UTM 11 Easting [m] | UTM 11 Northing [m] | Data Begin | Data End |
|---|---|---|---|---|---|---|
| P | 578 | -0.45 | 475681.9 | 3642843.3 | 10/21/2021 | 12/01/2021 |
| P | 579 | -0.31 | 475687.3 | 3642944.3 | 12/03/2021 | 12/21/2021 |
| P | 582 | -0.31 | 475652.9 | 3643235.5 | 10/20/2021 | 12/21/2021 |
| P | 583 | -0.70 | 475631.4 | 3643335.2 | 11/04/2021 | 12/21/2021 |
| P | 583.3 | -0.67 | 475628.0 | 3643364.4 | 11/04/2021 | 12/21/2021 |
| P | 584 | -0.40 | 475626.5 | 3643435.6 | 12/03/2021 | 12/21/2021 |
| P | 585 | -0.62 | 475604.4 | 3643534.5 | 10/20/2021 | 11/15/2021 |
| (lowered) |  | -1.22 | 475604.6 | 3643534.3 | 11/15/2021 | 12/21/2021 |
| P | 589 | -0.66 | 475540.4 | 3643930.2 | 10/20/2021 | 12/21/2021 |
| P | 593 | -1.19 | 475474.1 | 3644312.8 | 10/20/2021 | 12/21/2021 |

**Table A.2.** PUV locations, depths, and deployment durations. The relative lag is also given for PUV7.

| Sensor Type | MOP | Lag [m] | Depth [m] | UTM 11 Easting [m] | UTM 11 Northing | Data Begin | Data End |
|---|---|---|---|---|---|---|---|
| PUV | 582 | - | 30 | 474161.1 | 3643014.7 | 11/10/2021 | 03/02/2022 |
| PUV | 582 | - | 15 | 474728.0 | 3643123.9 | 10/19/2021 | 02/25/2022 |
| PUV | 573 | - | 10 | 475184.9 | 3642298.6 | 10/19/2021 | 03/02/2022 |
| PUV | 578 | - | 10 | 475139.0 | 3642837.1 | 10/19/2021 | 12/13/2021 |
| PUV | 582 | - | 10 | 475098.8 | 3643166.2 | 10/18/2021 | 02/25/2022 |
| PUV | 589 | - | 10 | 475011.0 | 3643871.7 | 10/18/2021 | 03/02/2022 |
| PUV | 579.2 | 0 | 7 | 475385.8 | 3642919.7 | 10/19/2021 | 10/26/2021 |
| PUV | 579.6 | 40 | 7 | 475380.1 | 3642958.4 | 10/19/2021 | 02/25/2022 |
| PUV | 580.4 | 80 | 7 | 475370.4 | 3643043.0 | 10/19/2021 | 02/25/2022 |
| PUV | 582 | 160 | 7 | 475351.8 | 3643198.9 | 10/19/2021 | 02/25/2022 |
| PUV | 584 | 200 | 7 | 475327.1 | 3643400.2 | 10/18/2021 | 02/25/2022 |
| PUV | 588.6 | 460 | 7 | 475260.2 | 3643859.0 | 10/18/2021 | 03/02/2022 |
| PUV | 589 | 40 | 7 | 475248.5 | 3643897.1 | 10/18/2021 | 03/02/2022 |
| PUV | 589.8 | 80 | 7 | 475233.8 | 3643975.6 | 10/18/2021 | 03/02/2022 |
| PUV | 591.4 | 160 | 7 | 475195.8 | 3644136.3 | 10/18/2021 | 02/25/2022 |
| PUV | 594 | 200 | 7 | 475154.0 | 3644328.9 | 10/18/2021 | 02/25/2022 |

# Appendix B

# SWASH Tests

## B.1 Standing Wave Amplification

The SWASH weakly reflective wave absorber in 1D (described in Zijlema et al. (2011); Vasarmidis et al. (2021)) can create a basin seiche from repeated constructive reflections between the beach and wavemaker. On a plane beach of slope $\beta$, a fully reflected shore-normal wave has surface elevation of

$$\eta(x,t) = aJ_0\left(2\omega\sqrt{\frac{x}{g\tan\beta}}\right)\cos(\omega t) \tag{B.1}$$

SWASH 1D is simulated with 5 cm incident waves (timeseries specified at the boundary) with varying domain lengths (from 50 to 60 m), sweeping the node-antinode cross-shore structure of Equation B.1. When the wavemaker was positioned at a node, the standing wave was amplified, and vice versa for antinodes (See Figure B.1).

For the same user-specified incident waves provided to the wavemaker, the resulting standing wave amplitude depends on basin width. This model artifact is associated with spurious, sometimes large standing wave motions excited by the imperfect numerical wave absorber and strong reflection at the beach. When incident wave amplitude is increased (Figure B.2), progressive waves begin to dominate over standing waves and the effect disappears. The max amplitude of the standing wave is roughly double in the case with

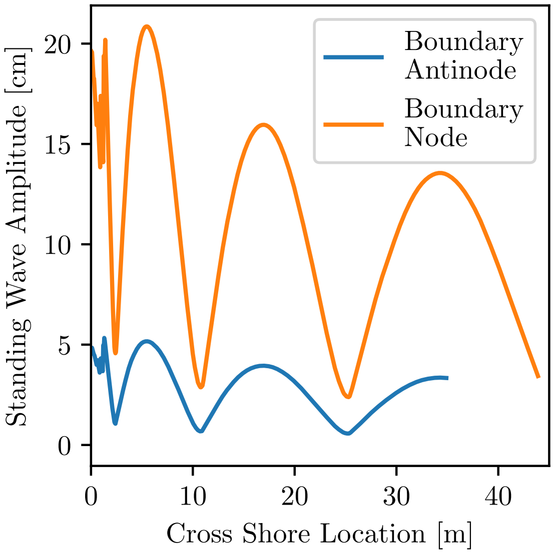

**Figure B.1.** SWASH 1D simulation of fully reflected waves with varied domain length, showing amplification when the wavemaker is positioned at a standing wave node. The amplitude of the standing wave (y axis) is compared to cross-shore position (x axis) for simulations where the boundary is at a node (orange) or antinode (blue) of the standing wave. Beach slope $\beta = 0.1$, $f_{inc} = 0.2$ Hz. A factor of 4 amplification is seen towards the shoreline.

the boundary condition being near a standing wave node.

Wavemaker amplification of fully reflected waves is potentially problematic for modeling studies of edge waves and other standing modes. An internal wavemaker may resolve this problem.

## B.2 Infragravity Edge Waves

SWASH 2D is initialized with a 3,000 m along-shore, 950 m across-shore domain, repeating in the alongshore. 2 computational layers are used. Along-shore resolution is 5 m, and cross-shore resolution is 2 m. Bathymetry is a plane beach of slope 0.06, therefore, the offshore boundary is at 57 meters depth. Waves are simulated for 30 minutes (1800 seconds). Boundary conditions are bichromatic, bi-directional sea swell waves ($f_1$=0.09 Hz, $f_2$=0.07 Hz, so that a 0.02 Hz wave is forced), each with a 30 cm amplitude. $f_1$ is always normally incident, $f_2$ is incident at some angle, see Figure B.3 for details. After 10 minutes, the wavemaker is shut off and the forced waves are allowed to propagate for 20 minutes. The cross-shore domain length was chosen to exclude higher mode edge waves at 0.02 Hz. Wave directions had to be manually chosen to fit in the alongshore domain.

Mode 1 edge waves are generated when the forced wavenumber is near a mode 1 edge wave wavenumber as predicted by linear theory for a plane beach. The resulting cross-shore structures are depicted in Figure B.4. Videos of simulated edge waves from the test are available as supplemental figures.

The runup variance of the forced wave 200 seconds after forcing was turned off, in each case, was used as a measure of the “response” of the mode 1 edge wave resonator. A Gaussian is fit to the response function to estimate the bandwidth (see Figure B.5), which is $k = 0.0022$ rad/m.

If Figure B.5 is taken to be representative of a test of wavenumber resonance, the quality factor $Q$ for the resonator can be computed ($Q = k_y/\Delta k_y$), resulting in $Q \approx 4$. The

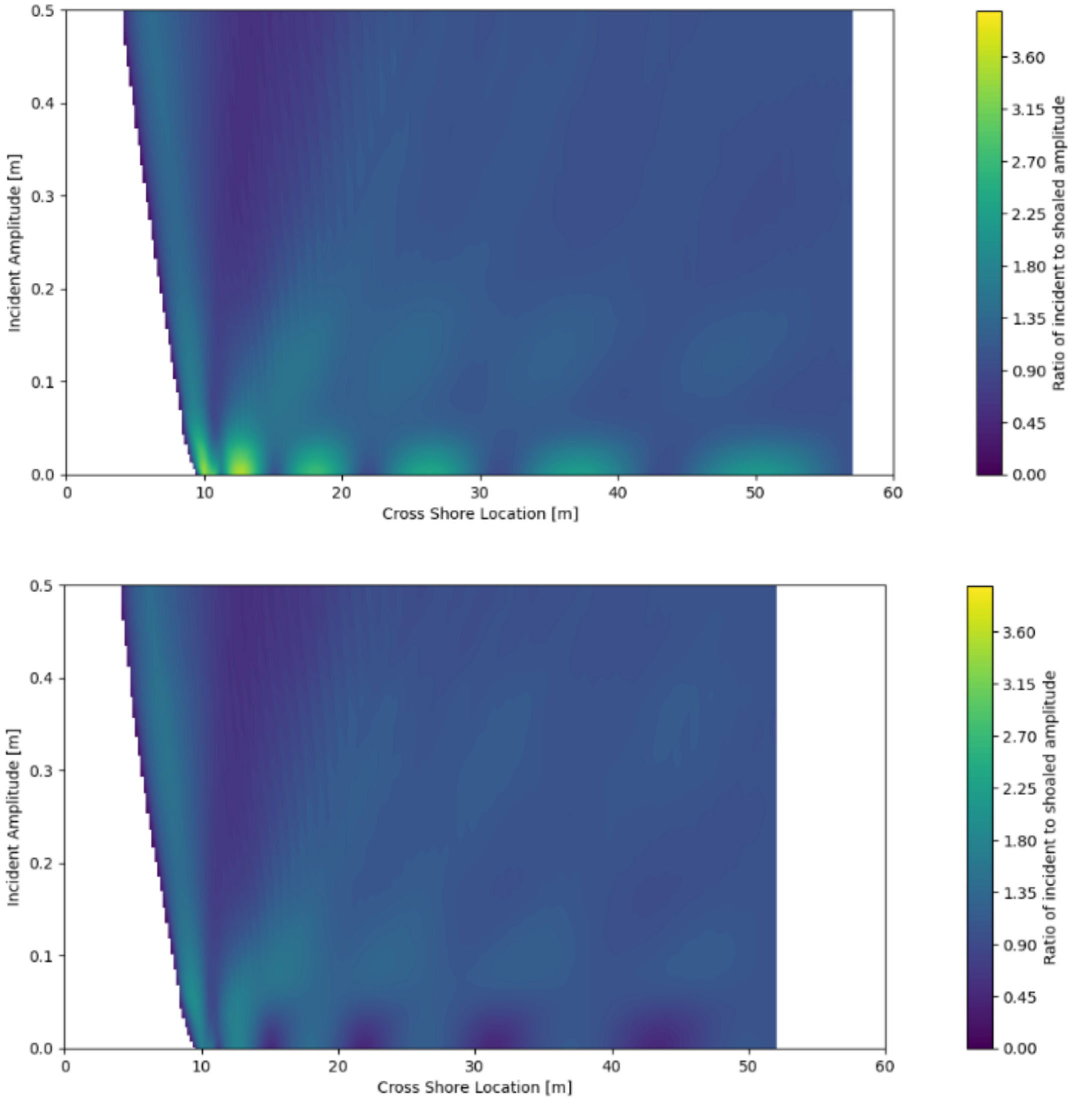

**Figure B.2.** SWASH 1D simulation of fully reflected waves with increasing amplitude, showing amplification when the wavemaker is positioned at a standing wave node. Cross shore structure (x axis) of reflected wave growth and decay (color intensity axis) for two different SWASH simulations are shown, one with the cross shore domain boundary near a standing wave node (top, $L_x = 57$ m) and antinode (bottom, $L_x = 52$ m). Requested incident wave amplitude is increased from 0 to 50 cm (y axis). Color intensity is the ratio of the amplitude at the wavemaker to the local amplitude in the domain, which combines both ingoing and outgoing waves. With large enough amplitude, the incident waves break instead of reflecting, and the amplification disappears, presumably because the phase-locked outgoing wave is no longer significant. Max amplification, a factor of 2, is achieved at the smallest amplitude.

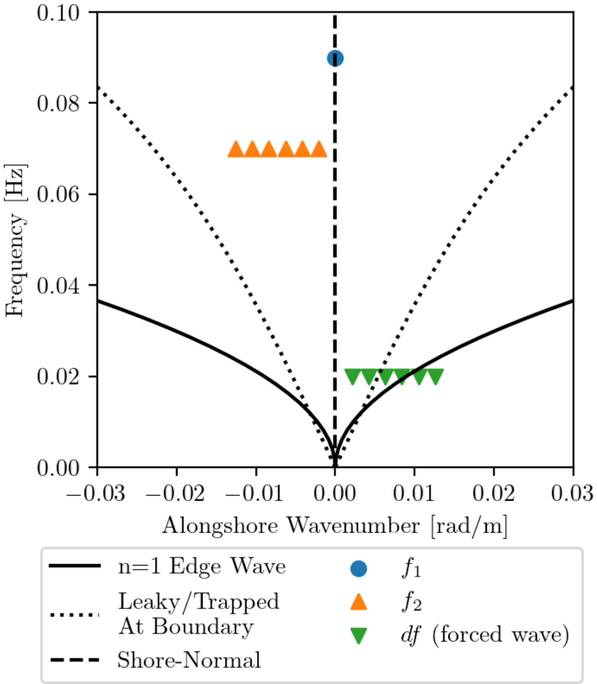

**Figure B.3.** Boundary condition for SWASH 2D simulation of trapped infragravity waves. In each case, two waves (0.09 Hz, blue and 0.07 Hz, orange) are incident on a plane beach (slope $\beta = 0.06$). Waves are generated in h=57 m depth and propagate 1 km to the shoreline. After 10 minutes, the wavemaker is turned off, and the forced infragravity wave (green) is considered. Incident wave angles are chosen to generate modes around a mode 1 edge wave at 0.02 Hz.

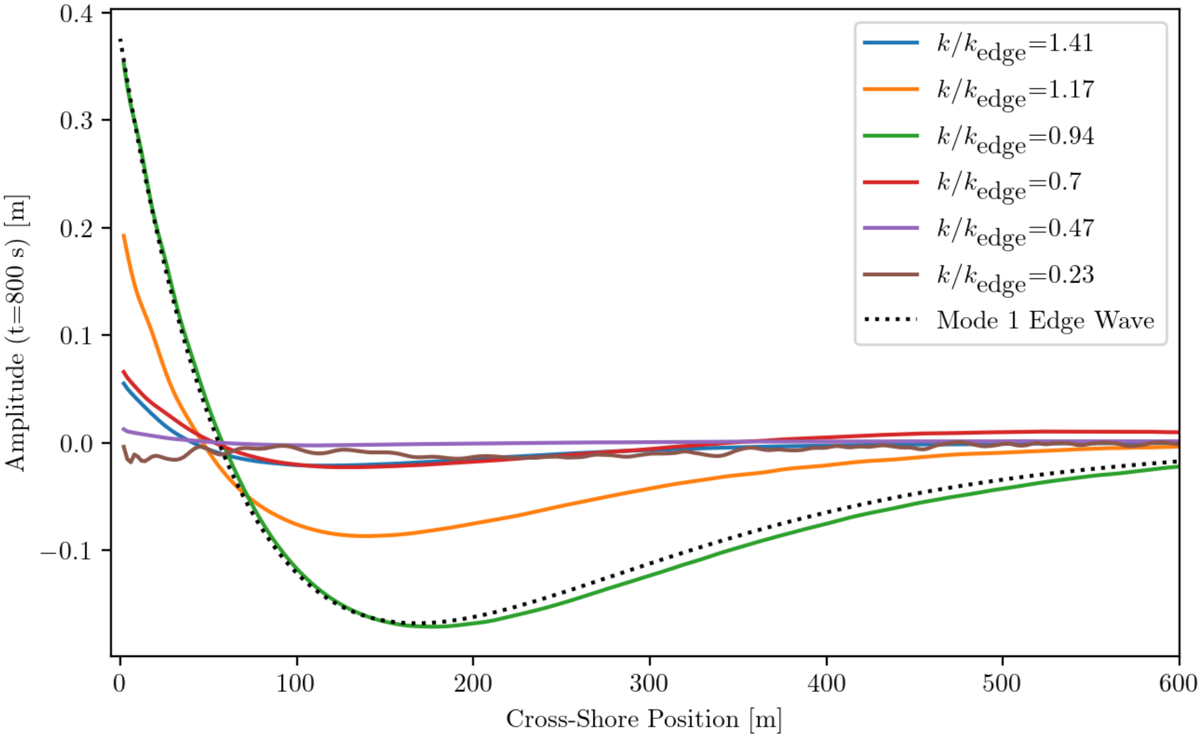

**Figure B.4.** Cross-shore structure of SWASH 2D modeled trapped infragravity waves. Profiles are computed by taking the average cross-shore profile seaward of runup maxima. Profiles are averaged from 800 to 1700 seconds (when the forcing is turned off and transients are mostly dissipated), and their amplitudes use the fit from above.

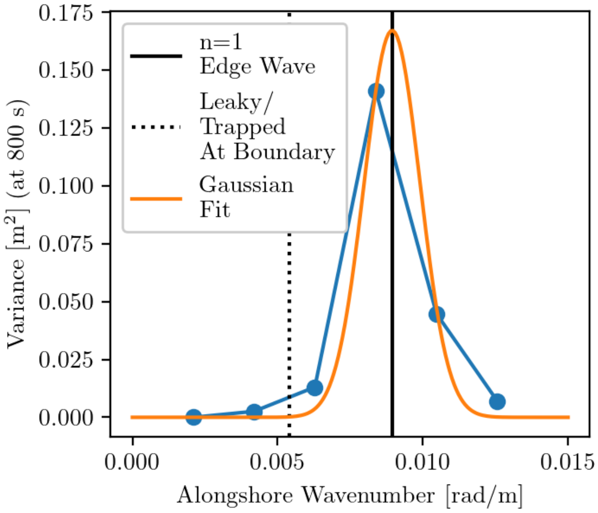

**Figure B.5.** Variance of SWASH 2D modeled trapped infragravity waves, with edge wave resonance. A Gaussian is fit to the 800 second variance of the forced wave, and the spread is used to compute resonance quality factor Q. The specific width of the peak (at half power) is $\Delta k = 0.0022$, and the central value is $k = 0.009$ rad/m. The Gaussian is assumed to center at the analytically computed wavenumber. For purposes of finding Q, only the width of the Gaussian matters.

response curve is rather wide compared to individual modes. This suggests that mode 2 and higher are likely to be close together relative to their resonant response curves, and are indistinguishable, if this test can be extrapolated to other frequencies/amplitudes/slopes.

Strong coupled harmonic and subharmonic edge waves and other higher-order triad interactions were observed within the domain, and an equilibrium state was generally not observed in the 10 minute spin-up, nor the 20 minute spin down. The average runup frequency wavenumber spectrum during model time with and without forcing is given in Figure B.6, demonstrating strong higher order interactions. The test resolution was also overly coarse, despite a wide (and computationally expensive) domain length. Wave simulations were also prone to instabilities leading to crashes, which could usually be fixed by decreasing time step and further increasing computational cost. Improvements on the modeling methodology addressing these problems are necessary for a future study.

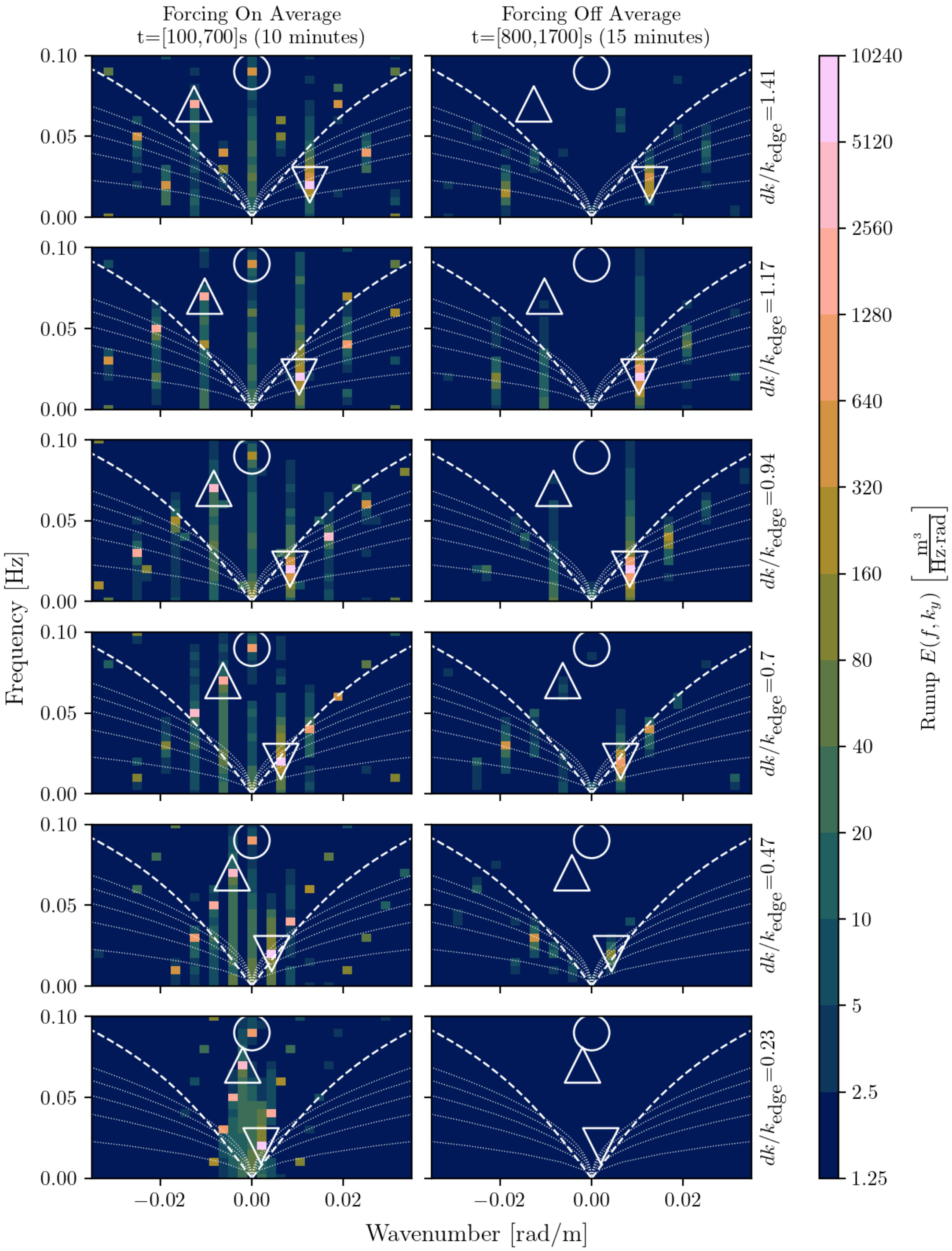

**Figure B.6.** Frequency/wavenumber spectra of SWASH 2D modeled trapped infragravity waves, including edge waves. Spectra are derived from 2D FFTs. 200 second segments with 50% overlap are used, for 6 segments in the first case and 10 segments in the second case. The spectra are averaged during forcing and after forcing. The triangular grid of variance demonstrates the importance of triad interactions. Strong nonlinear coupling leads to many high-order interactions which prevent the model from reaching equilibrium.

# Bibliography

Aagaard, T., Holm, J., 1989. Digitization of wave run-up using video records. Journal of Coastal Research , 547–551.

AJ, R., JH, M., EB, T., TP., S., 2006. Modelling infragravity motions on a rip-channel beach. Coastal Engineering 53, 209–222.

Almar, R., Blenkinsopp, C., Almeida, L.P., Cienfuegos, R., Catalán, P.A., 2017. Wave runup video motion detection using the radon transform. Coastal Engineering 130, 46–51.

Almeida, L., Masselink, G., Russell, P., Davidson, M., 2015. Observations of gravel beach dynamics during high energy wave conditions using a laser scanner. Geomorphology 228, 15–27.

Almeida, L.P., Masselink, G., Russell, P., Davidson, M., Poate, T., McCall, R., Blenkinsopp, C., Turner, I., 2013. Observations of the swash zone on a gravel beach during a storm using a laser-scanner (lidar). Journal of Coastal Research , 636–641.

Ardhuin, F., Rawat, A., Aucan, J., 2014. A numerical model for free infragravity waves: Definition and validation at regional and global scales. Ocean Modelling 77, 20–32.

Baldock, T., 2012. Dissipation of incident forced long waves in the surf zone—implications for the concept of "bound" wave release at short wave breaking. Coastal Engineering 60, 276–285.

Baldock, T., Huntley, D., 2002. Long–wave forcing by the breaking of random gravity waves on a beach. Proceedings of the Royal Society of London. Series A: Mathematical, Physical and Engineering Sciences 458, 2177–2201.

Baldock, T., Huntley, D., Bird, P., O'hare, T., Bullock, G., 2000. Breakpoint generated surf beat induced by bichromatic wave groups. Coastal Engineering 39, 213–242.

Barnard, P.L., Erikson, L.H., Foxgrover, A.C., Hart, J.A.F., Limber, P., O'Neill, A.C., van Ormondt, M., Vitousek, S., Wood, N., Hayden, M.K., Jones, J.M., 2019. Dynamic flood modeling essential to assess the coastal impacts of climate change. Scientific Reports 9.

Battjes, J., Bakkenes, H., Janssen, T., van Dongeren, A.R., 2004. Shoaling of subharmonic gravity waves. Journal of Geophysical Research: Oceans 109.

Battjes, J.A., Gerritsen, H., 2002. Coastal modelling for flood defence. Philosophical Transactions of the Royal Society of London. Series A: Mathematical, Physical and Engineering Sciences 360, 1461–1475.

Bendat, J.S., Piersol, A.G., 2011. Random data: analysis and measurement procedures. John Wiley & Sons.

Bertin, X., de Bakker, A., Van Dongeren, A., Coco, G., André, G., Ardhuin, F., Bonneton, P., Bouchette, F., Castelle, B., Crawford, W.C., et al., 2018. Infragravity waves: From driving mechanisms to impacts. Earth-Science Reviews 177, 774–799.

Bertin, X., Martins, K., de Bakker, A., Chataigner, T., Guérin, T., Coulombier, T., de Viron, O., 2020. Energy transfers and reflection of infragravity waves at a dissipative beach under storm waves. Journal of Geophysical Research: Oceans 125, e2019JC015714.

Biesel, F., 1952. Study of wave propagation in water of gradually varying depth. Gravity Waves , 243–253.

Blayo, E., Debreu, L., 2005. Revisiting open boundary conditions from the point of view of characteristic variables. Ocean Modelling 9, 231–252.

Blenkinsopp, C., Mole, M., Turner, I., Peirson, W., 2010. Measurements of the time-varying free-surface profile across the swash zone obtained using an industrial lidar. Coastal Engineering 57, 1059–1065.

Boers, M., 1997. Simulation of a surf zone with a barred beach; part 1: wave heights and wave breaking. Oceanographic Literature Review 4, 292.

Bowen, A.J., Guza, R.T., 1978. Edge waves and surf beat. Journal of Geophysical Research: Oceans 83, 1913–1920.

Briganti, R., Torres-Freyermuth, A., Baldock, T.E., Brocchini, M., Dodd, N., Hsu, T.J., Jiang, Z., Kim, Y., Pintado-Patiño, J.C., Postacchini, M., 2016. Advances in numerical modelling of swash zone dynamics. Coastal Engineering 115, 26–41. Swash-zone Processes.

Brodie, K.L., Slocum, R.K., McNinch, J.E., 2012. New insights into the physical drivers of wave runup from a continuously operating terrestrial laser scanner, in: 2012 Oceans, pp. 1–8.

Bromirski, P.D., Sergienko, O.V., MacAyeal, D.R., 2010. Transoceanic infragravity waves impacting antarctic ice shelves. Geophysical Research Letters 37.

Buckley, M., Lowe, R., Hansen, J., 2014. Evaluation of nearshore wave models in steep reef environments. Ocean Dynamics 64, 847–862.

Conde-Frias, M., Otero, L., Restrepo, J.C., Ortiz, J.C., Ruiz, J., Osorio, A.F., 2017. Swash Oscillations in a Microtidal Dissipative Beach. Journal of Coastal Research 33, 1408 – 1422.

Contardo, S., Lowe, R.J., Hansen, J.E., Rijnsdorp, D.P., Dufois, F., Symonds, G., 2021. Free and forced components of shoaling long waves in the absence of short-wave breaking. Journal of Physical Oceanography 51, 1465–1487.

Davis, R.E., Regier, L.A., 1977. Methods for estimating directional wave spectra from multi-element arrays .

De Bakker, A., Herbers, T., Smit, P., Tissier, M., Ruessink, B., 2015. Nonlinear infragravity–wave interactions on a gently sloping laboratory beach. Journal of Physical Oceanography 45, 589–605.

de Bakker, A., Tissier, M., Ruessink, B., 2014. Shoreline dissipation of infragravity waves. Continental Shelf Research 72, 73–82.

De Bakker, A., Tissier, M., Ruessink, B., 2016. Beach steepness effects on nonlinear infragravity-wave interactions: A numerical study. Journal of Geophysical Research: Oceans 121, 554–570.

de Beer, A., McCall, R., Long, J., Tissier, M., Reniers, A., 2021. Simulating wave runup on an intermediate–reflective beach using a wave-resolving and a wave-averaged version of xbeach. Coastal Engineering 163, 103788.

de Ridder, M.P., Smit, P.B., van Dongeren, A.R., McCall, R.T., Nederhoff, K., Reniers, A.J., 2021. Efficient two-layer non-hydrostatic wave model with accurate dispersive behaviour. Coastal Engineering 164, 103808.

Dodson-Robinson, S.E., Delgado, V.R., Harrell, J., Haley, C.L., 2022. Magnitude-squared coherence: a powerful tool for disentangling doppler planet discoveries from stellar activity. The Astronomical Journal 163, 169.

Dushaw, B.D., Worcester, P.F., Dzieciuch, M.A., 2011. On the predictability of mode-1 internal tides. Deep Sea Research Part I: Oceanographic Research Papers 58, 677–698.

Eckart, C., 1951. Surface waves on water of variable depth. Wave report nr. 100, SIO reference 51-12 .

Elgar, S., Raubenheimer, B., Guza, R.T., 2005. Quality control of acoustic doppler velocimeter data in the surfzone. Measurement Science and Technology 16, 1889.

Fiedler, J.W., Kim, L., Grenzeback, R.L., Young, A.P., Merrifield, M.A., 2021. Enhanced surf zone and wave runup observations with hovering drone-mounted lidar. Journal of Atmospheric and Oceanic Technology 38, 1967 – 1978.

Fiedler, J.W., Smit, P.B., Brodie, K.L., McNinch, J., Guza, R., 2018. Numerical modeling of wave runup on steep and mildly sloping natural beaches. Coastal Engineering 131, 106–113.

Fiedler, J.W., Smit, P.B., Brodie, K.L., McNinch, J., Guza, R., 2019. The offshore boundary condition in surf zone modeling. Coastal Engineering 143, 12–20.

Fiedler, J.W., Young, A.P., Ludka, B.C., O'Reilly, W.C., Henderson, C., Merrifield, M.A., Guza, R.T., 2020. Predicting site-specific storm wave run-up. Natural Hazards .

Foote, M., Horn, D., 1999. Video measurement of swash zone hydrodynamics. Geomorphology 29, 59–76.

Gallagher, B., 1971. Generation of surf beat by non-linear wave interactions. Journal of Fluid Mechanics 49, 1–20.

Gallien, T., 2016. Validated coastal flood modeling at imperial beach, california: Comparing total water level, empirical and numerical overtopping methodologies. Coastal Engineering 111, 95–104.

Gallien, T.W., Kalligeris, N., Delisle, M.P.C., Tang, B.X., Lucey, J.T.D., Winters, M.A., 2018. Coastal flood modeling challenges in defended urban backshores. Geosciences 8.

Gomes da Silva, P., Coco, G., Garnier, R., Klein, A.H., 2020. On the prediction of runup, setup and swash on beaches. Earth-Science Reviews 204, 103148.

Guedes, R.M., Bryan, K.R., Coco, G., 2013. Observations of wave energy fluxes and swash motions on a low-sloping, dissipative beach. Journal of geophysical research: Oceans 118, 3651–3669.

Guerci, J.R., 1999. Theory and application of covariance matrix tapers for robust adaptive beamforming. IEEE Transactions on Signal Processing 47, 977–985.

Guza, R., Thornton, E.B., 1985. Observations of surf beat. Journal of Geophysical Research: Oceans 90, 3161–3172.

Guza, R.T., Inman, D.L., 1975. Edge waves and beach cusps. Journal of Geophysical Research 80, 2997–3012.

Guza, R.T., Thornton, E.B., Holman, R.A., 1984. Swash on Steep and Shallow Beaches. pp. 708–723.

Haines, J.W., Thompson, K.R., Wiens, D.P., 1991. The detection of coastal-trapped waves. Journal of Geophysical Research: Oceans 96, 2593–2597.

Özkan Haller, H.T., Vidal, C., Losada, I.J., Medina, R., Losada, M.A., 2001. Standing edge waves on a pocket beach. Journal of Geophysical Research: Oceans 106, 16981–16996.

Hasselmann, K., 1967. Nonlinear interactions treated by the methods of theoretical physics (with application to the generation of waves by wind). Proceedings of the Royal Society of London. Series A. Mathematical and Physical Sciences 299, 77–103.

Henderson, C.S., Fiedler, J.W., Merrifield, M.A., Guza, R., Young, A.P., 2022. Phase resolving runup and overtopping field validation of swash. Coastal Engineering 175, 104128.

Henderson, S.M., Bowen, A., 2002. Observations of surf beat forcing and dissipation. Journal of Geophysical Research: Oceans 107, 14–1.

Henderson, S.M., Guza, R., Elgar, S., Herbers, T., Bowen, A., 2006. Nonlinear generation and loss of infragravity wave energy. Journal of Geophysical Research: Oceans 111.

Herbers, T., Elgar, S., Guza, R., 1994. Infragravity-frequency (0.005–0.05 hz) motions on the shelf. part i: Forced waves. Journal of Physical Oceanography 24, 917–927.

Herbers, T., Elgar, S., Guza, R., 1995a. Generation and propagation of infragravity waves. Journal of Geophysical Research: Oceans 100, 24863–24872.

Herbers, T., Elgar, S., Guza, R., 1999. Directional spreading of waves in the nearshore. Journal of Geophysical Research: Oceans 104, 7683–7693.

Herbers, T., Elgar, S., Guza, R., O'Reilly, W., 1995b. Infragravity-frequency (0.005–0.05 hz) motions on the shelf. part ii: Free waves. Journal of physical oceanography 25, 1063–1079.

Hinkel, J., Lincke, D., Vafeidis, A.T., Perrette, M., Nicholls, R.J., Tol, R.S.J., Marzeion, B., Fettweis, X., Ionescu, C., Levermann, A., 2014. Coastal flood damage and adaptation costs under 21st century sea-level rise. Proceedings of the National Academy of Sciences 111, 3292–3297.

Holman, R., 1986. Extreme value statistics for wave run-up on a natural beach. Coastal Engineering 9, 527–544.

Holman, R.A., Bowen, A.J., 1979. Edge waves on complex beach profiles. Journal of Geophysical Research: Oceans 84, 6339–6346.

Holthuijsen, L., Booij, N., Ris, R., 1993. A spectral wave model for the coastal zone, in: Ocean Wave Measurement and Analysis, ASCE. pp. 630–641.

Huntley, D., 1976. Long-period waves on a natural beach. Journal of Geophysical Research 81, 6441–6449.

Huntley, D., Guza, R., Thornton, E., 1981. Field observations of surf beat: 1. progressive edge waves. Journal of Geophysical Research: Oceans 86, 6451–6466.

Huntley, D.A., 1988. Evidence for phase coupling between edge wave modes. Journal of Geophysical Research: Oceans 93, 12393–12408.

Janssen, T., Battjes, J., Van Dongeren, A., 2003. Long waves induced by short-wave groups over a sloping bottom. Journal of Geophysical Research: Oceans 108.

Jasak, H., Jemcov, A., Tukovic, Z., et al., 2007. Openfoam: A c++ library for complex physics simulations, in: International workshop on coupled methods in numerical dynamics, IUC Dubrovnik Croatia. pp. 1–20.

Kachelein, L., Cornuelle, B.D., Gille, S.T., Mazloff, M.R., 2022. Harmonic analysis of non-phase-locked tides with red noise using the red_tide package. Journal of Atmospheric and Oceanic Technology 39, 1031–1051.

van Kuik, A.J., van Vledder, G.P., Holthuijsen, L.H., 1988. A method for the routine analysis of pitch-and-roll buoy wave data. Journal of Physical Oceanography 18, 1020–1034.

Lange, A.M., Fiedler, J.W., Merrifield, M.A., Guza, R., 2023a. Data related to "Free infragravity waves on the inner shelf: Observations and Parameterizations at two Southern California beaches".

Lange, A.M., Fiedler, J.W., Merrifield, M.A., Guza, R., 2023b. Free infragravity waves on the inner shelf: Observations and parameterizations at two southern california beaches. Authorea Preprints .

Lara, J.L., Ruju, A., Losada, I.J., 2011. Reynolds averaged navier–stokes modelling of long waves induced by a transient wave group on a beach. Proceedings of the Royal Society A: Mathematical, Physical and Engineering Sciences 467, 1215–1242.

Lashley, C.H., Roelvink, D., van Dongeren, A., Buckley, M.L., Lowe, R.J., 2018. Nonhydrostatic and surfbeat model predictions of extreme wave run-up in fringing reef environments. Coastal Engineering 137, 11–27.

Lashley, C.H., Zanuttigh, B., Bricker, J.D., van der Meer, J., Altomare, C., Suzuki, T., Roeber, V., Oosterlo, P., 2020. Benchmarking of numerical models for wave overtopping at dikes with shallow mildly sloping foreshores: Accuracy versus speed. Environmental Modelling  Software 130, 104740.

Liao, Z., Li, S., Liu, Y., Zou, Q., 2021. An analytical spectral model for infragravity waves over topography in intermediate and shallow water under nonbreaking conditions. Journal of Physical Oceanography 51, 2749–2765.

Lippmann, T., Holman, R.A., Bowen, A., 1997. Generation of edge waves in shallow water. Journal of Geophysical Research: Oceans 102, 8663–8679.

Longuet-Higgins, M.S., Stewart, R., 1964. Radiation stresses in water waves; a physical discussion, with applications, in: Deep sea research and oceanographic abstracts, Elsevier. pp. 529–562.

Ludka, B.C., Guza, R.T., O’Reilly, W.C., Merrifield, M.A., Flick, R.E., Bak, A.S., Hesser, T., Bucciarelli, R., Olfe, C., Woodward, B., Boyd, W., Smith, K., Okihiro, M., Grenzeback, R., Parry, L., Boyd, G., 2019. Sixteen years of bathymetry and waves at san diego beaches. Scientific Data 6.

Ludka, B.C., Guza, R.T., O'Reilly, W.C., Yates, M.L., 2015. Field evidence of beach profile evolution toward equilibrium. Journal of Geophysical Research: Oceans 120, 7574–7597.

Lygre, A., Krogstad, H.E., 1986. Maximum entropy estimation of the directional distribution in ocean wave spectra. Journal of Physical Oceanography 16, 2052–2060.

Martins, K., Blenkinsopp, C.E., Zang, J., 2015. Monitoring individual wave characteristics in the inner surf with a 2-dimensional laser scanner (lidar). Journal of Sensors 2016, 7965431.

Matias, A., Rita Carrasco, A., Loureiro, C., Masselink, G., Andriolo, U., McCall, R., Óscar Ferreira, Plomaritis, T.A., Pacheco, A., Guerreiro, M., 2019. Field measurements and hydrodynamic modelling to evaluate the importance of factors controlling overwash. Coastal Engineering 152, 103523.

Matsuba, Y., Shimozono, T., 2021. Analysis of the contributing factors to infragravity swash based on long-term observations. Coastal Engineering 169, 103957.

Matsumoto, H., Young, A.P., Guza, R.T., 2020. Observations of surface cobbles at two southern california beaches. Marine Geology 419, 106049.

McCall, R., Masselink, G., Poate, T., Roelvink, J., Almeida, L., Davidson, M., Russell, P., 2014. Modelling storm hydrodynamics on gravel beaches with xbeach-g. Coastal Engineering 91, 231–250.

Melito, L., Parlagreco, L., Devoti, S., Brocchini, M., 2022. Wave- and tide-induced infragravity dynamics at an intermediate-to-dissipative microtidal beach. Journal of Geophysical Research: Oceans 127, e2021JC017980. E2021JC017980 2021JC017980.

Mendes, D., Pinto, J.P., Pires-Silva, A.A., Fortunato, A.B., 2018. Infragravity wave energy changes on a dissipative barred beach: A numerical study. Coastal Engineering 140, 136–146.

Merrifield, M.A., Johnson, M., Guza, R., Fiedler, J.W., Young, A.P., Henderson, C.S., Lange, A.M., O'Reilly, W.C., Ludka, B.C., Okihiro, M., et al., 2021. An early warning system for wave-driven coastal flooding at imperial beach, ca. Natural Hazards , 1–22.

Middleton, J.F., Black, K.P., 1994. The low frequency circulation in and around bass strait: a numerical study. Continental Shelf Research 14, 1495–1521.

Munk, W., 2000. Achievements in physical oceanography. 50 Years of Ocean Discovery: National Science Foundation 1950-2000 , 44.

Munk, W., Snodgrass, F., Carrier, G., 1956. Edge waves on the continental shelf. Science 123, 127–132.

Munk, W., Snodgrass, F., Gilbert, F., 1964. Long waves on the continental shelf: an experiment to separate trapped and leaky modes. Journal of Fluid Mechanics 20, 529–554.

Munk, W.H., 1949. Surf beats. EOS, Transactions American Geophysical Union 30, 849–854.

Nicholls, R.J., Cazenave, A., 2010. Sea-level rise and its impact on coastal zones. Science 328, 1517–1520.

Nicolae Lerma, A., Pedreros, R., Robinet, A., Sénéchal, N., 2017. Simulating wave setup and runup during storm conditions on a complex barred beach. Coastal Engineering 123, 29–41.

Nielsen, P., Baldock, T.E., 2010. -shaped surf beat understood in terms of transient forced long waves. Coastal Engineering 57, 71–73.

Okihiro, M., Guza, R., 1995. Infragravity energy modulation by tides. Journal of Geophysical Research: Oceans 100, 16143–16148.

Okihiro, M., Guza, R., Seymour, R., 1992. Bound infragravity waves. Journal of Geophysical Research: Oceans 97, 11453–11469.

Oltman-Shay, J., Guza, R., 1987. Infragravity edge wave observations on two california beaches. Journal of Physical Oceanography 17, 644–663.

Oltman-Shay, J., Howd, P.A., 1993. Edge waves on nonplanar bathymetry and alongshore currents: a model and data comparison. Journal of Geophysical Research: Oceans 98, 2495–2507.

O'Reilly, W., Olfe, C.B., Thomas, J., Seymour, R., Guza, R., 2016. The california coastal wave monitoring and prediction system. Coastal Engineering 116, 118–132.

O'Neill, A.C., Erikson, L.H., Barnard, P.L., Limber, P.W., Vitousek, S., Warrick, J.A., Foxgrover, A.C., Lovering, J., 2018. Projected 21st century coastal flooding in the southern california bight. part 1: Development of the third generation cosmos model. Journal of Marine Science and Engineering 6.

Pawka, S.S., 1983. Island shadows in wave directional spectra. Journal of Geophysical Research: Oceans 88, 2579–2591.

Pullen, T., Allsop, N., Bruce, T., Kortenhaus, A., Schüttrumpf, H., Van der Meer, J., 2007. EurOtop wave overtopping of sea defences and related structures: assessment manual.

Raubenheimer, B., Elgar, S., Guza, R.T., 1998. Estimating wave heights from pressure measured in sand bed. Journal of Waterway, Port, Coastal, and Ocean Engineering 124, 151–154.

Raubenheimer, B., Guza, R., Elgar, S., 1996. Wave transformation across the inner surf zone. Journal of Geophysical Research: Oceans 101, 25589–25597.

Reniers, A., Van Dongeren, A., Battjes, J., Thornton, E., 2002. Linear modeling of infragravity waves during delilah. Journal of Geophysical Research: Oceans 107, 1–1.

Rijnsdorp, D.P., Ruessink, G., Zijlema, M., 2015. Infragravity-wave dynamics in a barred coastal region, a numerical study. Journal of Geophysical Research: Oceans 120, 4068–4089.

Rijnsdorp, D.P., Smit, P.B., Guza, R., 2022. A nonlinear, non-dispersive energy balance for surfzone waves: infragravity wave dynamics on a sloping beach. Journal of Fluid Mechanics 944, A45.

Rijnsdorp, D.P., Smit, P.B., Zijlema, M., 2014. Non-hydrostatic modelling of infragravity waves under laboratory conditions. Coastal Engineering 85, 30–42.

Roelvink, D., McCall, R., Mehvar, S., Nederhoff, K., Dastgheib, A., 2018. Improving predictions of swash dynamics in xbeach: The role of groupiness and incident-band runup. Coastal Engineering 134, 103–123. RISC-KIT: Resilience-increasing Strategies for Coasts – Toolkit.

Roelvink, D., Reniers, A., van Dongeren, A., van Thiel de Vries, J., McCall, R., Lescinski, J., 2009. Modelling storm impacts on beaches, dunes and barrier islands. Coastal Engineering 56, 1133–1152.

Ruessink, B., Kleinhans, M., Van den Beukel, P., 1998. Observations of swash under highly dissipative conditions. Journal of Geophysical Research: Oceans 103, 3111–3118.

Ruju, A., Lara, J.L., Losada, I.J., 2012. Radiation stress and low-frequency energy balance within the surf zone: A numerical approach. Coastal engineering 68, 44–55.

Ruju, A., Lara, J.L., Losada, I.J., 2014. Numerical analysis of run-up oscillations under dissipative conditions. Coastal Engineering 86, 45–56.

Salatin, R., Chen, Q., Bak, A.S., Shi, F., Brandt, S.R., 2021. Effects of wave coherence on longshore variability of nearshore wave processes. Journal of Geophysical Research: Oceans 126, e2021JC017641.

Salmon, S., Bryan, K., Coco, G., 2007. The use of video systems to measure run-up on beaches. Journal of Coastal Research , 211–215.

Sand, S.E., 1982. Long waves in directional seas. Coastal Engineering 6, 195–208.

Satopaa, V., Albrecht, J., Irwin, D., Raghavan, B., 2011. Finding a "kneedle" in a haystack: Detecting knee points in system behavior, in: 2011 31st International Conference on Distributed Computing Systems Workshops, pp. 166–171.

Schäffer, H.A., 1993. Infragravity waves induced by short-wave groups. Journal of Fluid Mechanics 247, 551–588.

Schäffer, H.A., Jonsson, I.G., 1992. Edge waves revisited. Coastal engineering 16, 349–368.

Shaeri, S., Etemad-Shahidi, A., 2021. Wave overtopping at vertical and battered smooth impermeable structures. Coastal Engineering 166, 103889.

Sheremet, A., Guza, R., Elgar, S., Herbers, T., 2001. Estimating infragravity wave properties from pressure-current meter array observations, in: Coastal Engineering 2000, pp. 1476–1489.

Sheremet, A., Guza, R., Elgar, S., Herbers, T., 2002. Observations of nearshore infragravity waves: Seaward and shoreward propagating components. Journal of Geophysical Research: Oceans 107, 10–1.

Smit, P., Janssen, T., Herbers, T., Taira, T., Romanowicz, B., 2018. Infragravity wave radiation across the shelf break. Journal of Geophysical Research: Oceans 123, 4483–4490.

Smit, P., Janssen, T., Holthuijsen, L., Smith, J., 2014. Non-hydrostatic modeling of surf zone wave dynamics. Coastal Engineering 83, 36–48.

Smit, P., Stelling, G., Roelvink, J., Van Thiel de Vries, J., McCall, R., Van Dongeren, A., Zwinkels, C., Jacobs, R., 2010. Xbeach: Non-hydrostatic model: Validation, verification and model description. Delft Univ. Technol .

Smit, P., Zijlema, M., Stelling, G., 2013. Depth-induced wave breaking in a non-hydrostatic, near-shore wave model. Coastal Engineering 76, 1–16.

Soldini, L., Antuono, M., Brocchini, M., 2013. Numerical modeling of the influence of the beach profile on wave run-up. Journal of Waterway, Port, Coastal, and Ocean Engineering 139, 61–71.

Stockdon, H.F., Holman, R.A., Howd, P.A., Sallenger Jr, A.H., 2006. Empirical parameterization of setup, swash, and runup. Coastal engineering 53, 573–588.

Stokes, G., 1846. Report on recent researches in hydrodynamics. British Association Report.

Stokes, K., Poate, T., Masselink, G., King, E., Saulter, A., Ely, N., 2021. Forecasting coastal overtopping at engineered and naturally defended coastlines. Coastal Engineering 164, 103827.

Stringari, C.E., Power, H.E., 2020. Quantifying bore-bore capture on natural beaches. Journal of Geophysical Research: Oceans 125, e2019JC015689.

Suhayda, J.N., 1974. Determining nearshore infragravity wave spectra. .

Suzuki, T., Altomare, C., Veale, W., Verwaest, T., Trouw, K., Troch, P., Zijlema, M., 2017. Efficient and robust wave overtopping estimation for impermeable coastal structures in shallow foreshores using swash. Coastal Engineering 122, 108–123.

Symonds, G., Huntley, D.A., Bowen, A.J., 1982. Two-dimensional surf beat: Long wave generation by a time-varying breakpoint. Journal of Geophysical Research: Oceans 87, 492–498.

Thomson, J., Elgar, S., Raubenheimer, B., Herbers, T., Guza, R., 2006. Tidal modulation of infragravity waves via nonlinear energy losses in the surfzone. Geophysical Research Letters 33.

Torres-Freyermuth, A., Pintado-Patiño, J.C., Pedrozo-Acuña, A., Puleo, J.A., Baldock, T.E., 2019. Runup uncertainty on planar beaches. Ocean Dynamics 69, 1359–1371.

Torres-Freyermuth, A., Mariño Tapia, I., Coronado, C., Salles, P., Medellín, G., Pedrozo-Acuña, A., Silva, R., Candela, J., Iglesias-Prieto, R., 2012. Wave-induced extreme water levels in the puerto morelos fringing reef lagoon. Natural Hazards and Earth System Sciences 12, 3765–3773.

Tucker, M.J., Deacon, G.E.R., 1950. Surf beats: sea waves of 1 to 5 min. period. Proceedings of the Royal Society of London. Series A. Mathematical and Physical Sciences 202, 565–573.

Uncles, R., Stephens, J., Harris, C., 2014. Infragravity currents in a small ría: Estuary-amplified coastal edge waves? Estuarine, Coastal and Shelf Science 150, 242–251. Special issue on Problems of Small Estuaries.

Ursell, F., 1952. Edge waves on a sloping beach. Proceedings of the royal society of London. Series A. Mathematical and Physical Sciences 214, 79–97.

Van Dongeren, A., Battjes, J., Janssen, T., Van Noorloos, J., Steenhauer, K., Steenbergen, G., Reniers, A., 2007. Shoaling and shoreline dissipation of low-frequency waves. Journal of Geophysical Research: Oceans 112.

Van Dongeren, A., Reniers, A., Battjes, J., Svendsen, I., 2003. Numerical modeling of infragravity wave response during delilah. Journal of Geophysical Research: Oceans 108.

Van Trees, L.H., 2001. Detection, estimation, and modulation theory-part l-detection, estimation, and linear modulation theory. John Wiley  Sons.

Vasarmidis, P., Stratigaki, V., Suzuki, T., Zijlema, M., Troch, P., 2021. On the accuracy of internal wave generation method in a non-hydrostatic wave model to generate and absorb dispersive and directional waves. Ocean Engineering 219, 108303.

Villarroel-Lamb, D., Hammeken, A.M., Simons, R., 2014. Quantifying the effect of bed permeability on maximum wave runup.

Vousdoukas, M.I., Voukouvalas, E., Mentaschi, L., Dottori, F., Giardino, A., Bouziotas, D., Bianchi, A., Salamon, P., Feyen, L., 2016. Developments in large-scale coastal flood hazard mapping. Natural Hazards and Earth System Sciences 16, 1841–1853.

Webb, S.C., Zhang, X., Crawford, W., 1991. Infragravity waves in the deep ocean. Journal of Geophysical Research: Oceans 96, 2723–2736.

Wunsch, C., 2006. Discrete inverse and state estimation problems: with geophysical fluid applications. Cambridge University Press.

Young, A.P., Matsumoto, H., Spydell, M.S., Dickson, M.E., 2023. Cobble tracking observations at torrey pines state beach, ca, usa. Journal of Geophysical Research: Earth Surface 128, e2023JF007199. E2023JF007199 2023JF007199.

Zijlema, M., Stelling, G., Smit, P., 2011. Swash: An operational public domain code for simulating wave fields and rapidly varied flows in coastal waters. Coastal Engineering 58, 992–1012.